Dissertation zur Erlangung des Doktorgrades der Fakultät Chemie und Pharmazie
der Ludwig-Maximilians-Universität München

Live-cell imaging of drug delivery by mesoporous silica nanoparticles

Drug loading, pore sealing, cellular uptake and controlled drug release

Anna Magdalena Sauer

aus

Assis, Brasilien

2011

Erklärung

Diese Dissertation wurde im Sinne von §13 Abs. 3 bzw. 4 der Promotionsordnung vom 29. Januar 1998 (in der Fassung der sechsten Änderungssatzung vom 16. August 2010) von Herrn Prof. Dr. Christoph Bräuchle betreut.

Ehrenwörtliche Versicherung

Diese Dissertation wurde selbständig, ohne unerlaubte Hilfe erarbeitet.

München, den 31. August 2011

Anna Magdalena Sauer

Dissertation eingereicht am	31.08.2011
1. Gutachter	Prof. Dr. Christoph Bräuchle
2. Gutachter	Prof. Dr. Thomas Bein
Mündliche Prüfung am	18.10.2011

Summary

In order to deliver drugs to diseased cells nanoparticles featuring controlled drug release are developed. Controlled release is of particular importance for the delivery of toxic anti-cancer drugs that should not get in contact with healthy tissue. To evaluate the effectivity and controlled drug-release ability of nanoparticles in the target cell, live-cell imaging by highly-sensitive fluorescence microscopy is a powerful method. It allows direct real-time observation of nanoparticle uptake into the target cell, intracellular trafficking and drug release. With this knowledge, existing nanoparticles can be evaluated, improved and more effective nanoparticles can be designed. The goal of this work was to study the internalization efficiency, successful drug loading, pore sealing and controlled drug release from colloidal mesoporous silica (CMS) nanoparticles. The entire work was performed in close collaboration with the group of Prof. Thomas Bein (LMU Munich), where the nanoparticles were synthesized.

To deliver drugs into a cell, the extracellular membrane has to be crossed. Therefore, in the first part of this work, the internalization efficiency of PEG-shielded CMS nanoparticles into living HeLa cells was examined by a quenching assay. The internalization time scales varied considerably from cell to cell. However, about 67% of PEG-shielded CMS nanoparticles were internalized by the cells within one hour. The time scale is found to be in the range of other nanoparticles (polyplexes, magnetic lipoplexes [1, 2]) that exhibit non-specific uptake.

Besides internalization efficiency, successful drug loading and pore sealing are important parameters for drug delivery. To study this, CMS nanoparticles were loaded with the anti-cancer drug colchicine and sealed by a supported lipid bilayer using a solvent exchange method (additional collaboration with the group of Prof. Joachim Rädler, LMU). Spinning disk confocal live-cell imaging revealed that the nanoparticles were taken up into HuH7 cells by endocytosis. As colchicine is known to exhibit toxicity towards microtubules, the microtubule network of the cells was destroyed within 2 h of incubation with the colchicine-loaded lipid bilayer-coated CMS nanoparticles. Although successful drug delivery was shown, it is necessary to develop controlled local release strategies.

To achieve controlled drug release, CMS nanoparticles for redox-driven disulfide cleavage were synthesized. The particles contain the ATTO633-labeled amino acid cysteine bound via a disulfide linker to the inner volume. For reduction of the disulfide bond and release of cysteine, the CMS nanoparticles need to get into contact with the cytoplasmic reducing milieu of the target cell. We showed that nanoparticles were taken up by HuH7 cells via endocytosis, but endosomal escape seems to be a bottleneck for this approach. Incubation of the cells with a photosensitizer ($TPPS_{2a}$) and photoactivation led to endosomal escape and successful release of the drug. In addition, we showed that linkage of ATTO633 at high concentration in the pores of silica nanoparticles results in quenching of the ATTO633 fluorescence. Release of dye from the pores promotes a strong dequenching effect providing an intense fluorescence signal with excellent signal-to-noise ratio for single-particle imaging. With this approach, we were able to control the time of photoactivation and thus the time of endosomal rupture. However, the photosensitizer showed a high toxicity to the cell, due to its

presence in the entire cellular membrane.

To reduce cell toxicity induced by the photosensitizer and to achieve spatial control on the endosomal escape, the photosensitizer protoporphyrin IX (PpIX) was covalently surface-linked to the CMS nanoparticles and used as an on-board photosensitizer (additional collaboration with the groups of Prof. Joachim Rädler and Prof. Heinrich Leonhardt, both LMU). The nanoparticles were loaded with model drugs and equipped with a supported lipid bilayer as a removable encapsulation. Upon photoactivation, successful drug delivery was observed. The mode of action is proposed as a two-step cascade, where the supported lipid bilayer is disintegrated by singlet oxygen in a first step and the endosomal membrane ruptures enabling drug release in a second step. With this system, stimuli-responsive and controlled, localized endosomal escape and drug release is achieved.

Taken together, the data presented in this thesis show that real-time fluorescence imaging of CMS nanoparticles on a single-cell level is a powerful method to investigate in great detail the processes associated with drug delivery. Barriers in the internalization and drug delivery are detected and can be bypassed via new nanoparticle designs. These insights are of great importance for improvements in the design of existing and the synthesis of new drug delivery systems.

Contents

Summary v

1 Introduction 1

2 Principles of nanomedical drug delivery 5
2.1 Uptake and trafficking of nanoparticles in cells . . . 5
2.1.1 Accumulation at the target tissue . . . 6
2.1.2 Cellular internalization . . . 7
2.1.3 Intracellular trafficking . . . 9
2.1.4 Endosomal release . . . 9
2.2 Nanoparticle designs for drug delivery . . . 10
2.2.1 Polymeric nanoparticles . . . 11
2.2.2 Lipid-based nanoparticles . . . 11
2.2.3 Viral nanoparticles . . . 11
2.2.4 Inorganic nanoparticles . . . 12

3 Colloidal mesoporous silica (CMS) nanoparticles 13
3.1 Mesoporous silica materials . . . 13
3.2 Synthesis of CMS nanoparticles . . . 13
3.2.1 Outer-shell functionalized CMS . . . 14
3.2.2 Core-shell functionalized CMS . . . 15
3.2.3 Template extraction . . . 15
3.3 CMS nanoparticles as drug delivery vehicles . . . 16
3.3.1 Drug loading . . . 16
3.3.2 Pore sealing . . . 16
3.3.3 Cancer cell targeting . . . 17
3.3.4 Stimuli-responsive release . . . 18
3.4 Biocompatibility of CMS nanoparticles . . . 22
3.4.1 Size, surface properties and concentration . . . 22
3.4.2 Degradation . . . 23

4 Fluorescence live-cell imaging 25
4.1 Principles of fluorescence . . . 25
4.2 Bleaching and quenching . . . 27

4.3 Wide-field and spinning disk confocal microscopy 27
4.4 Living cancer cells in fluorescence microscopy 29

5 Experimental methods and data analysis 31
5.1 Chemicals 31
5.2 Cell culture 31
5.3 Preparation of SLB@CMS 32
5.4 Fluorescence spectrometry 32
5.5 Microscopy *in vitro* and in live cells 33
5.6 Fluorescence intensity evaluation of the CMS-loaded drug and fluid phase marker. . 35

6 Internalization of CMS nanoparticles 37
6.1 Choice of a quenchable dye 37
6.2 Choice of quenchable CMS nanoparticles with PEG-shell 39
6.3 Uptake percentage of CMS-PEG550 into HeLa cells 40
6.4 Targeting of CMS nanoparticles with receptor-ligands 42
6.5 Summary 42

7 Lipid bilayer-coated CMS nanoparticles 43
7.1 Colchicine delivery by lipid bilayer-coated CMS 43
7.1.1 Synthesis and characterization of SLB@CMS 45
7.1.2 Mode of cellular uptake of POPC-SLB@CMS 46
7.1.3 Colchicine delivery from SLB@CMS nanoparticles 46
7.2 Variation in SLB composition and the influence on CMS uptake 51
7.2.1 Characterization of SLB@CMS nanoparticle integrity 51
7.2.2 Mode of uptake for various SLB@CMS nanoparticles into living cells 53
7.3 Summary 55

8 Disulfide-based drug delivery induced by photochemical internalization (PCI) 57
8.1 Synthesis of CMS for disulfide-based drug delivery 58
8.2 Single-particle characterization *in vitro* 59
8.3 Long-term live-cell imaging of HuH7 cells incubated with CMS nanoparticles 60
8.4 Photochemically-induced endosomal release 62
8.5 Summary 64

9 Cascaded photoinduced drug delivery from mutifunctional PpIX-mesoporous silica 67
9.1 Synthesis of CMS-NH_{2core}-$PpIX_{shell}$ 68
9.2 PpIX-induced disulfide-based drug delivery from CMS 69
9.3 PpIX-induced release mechanism of chromobodies from CMS 72
9.4 Cellular effects of PpIX-induced drug release 74
9.5 Summary 76

List of abbreviations **77**

Bibliography **81**

Acknowledgments **103**

List of publications **105**

Curriculum Vitae **107**

1 Introduction

66% of the German population estimate the risk of nanotechnology to be lower than its benefits. This statement is one conclusion of a study on public perceptions about nanotechnology, conducted by the German Federal Institute for Risk Assessment (BfR) in 2008. According to this study, 77% of the respondents state to have a good or very good feeling about this technology, but the acceptance is not equally distributed over all areas of nanotechnology [3]. For example, nanotechnology in the food sector is viewed critically, whereas nanotechnology in medicine is one of the areas connected with the highest expectations [3]. However, the shaping of the public opinion on the subject of nanotechnology is not at its end.

To help that public expectations remain realistic, it is important to maintain a dialog with the media and the public. One example for this was presented in the TV show "Faszination Wissen" in Bavarian Television (Bayrisches Fernsehen) broadcasted in March 2011, where scientists, among others Prof. Christoph Bräuchle from the LMU Munich and Prof. Christian Plank from the TU Munich, presented their research and opinions on nanomedicine. The key message of the show can be summarized as follows: nanotechnology is still struggling with reservations, but first success stories from the clinics, especially with novel drug delivery systems against cancer, are raising great hopes.

A drug delivery system is, on a symbolic level, a nanoscale "trojan horse". Its purpose is to transport drugs to target cells, while remaining unrecognized by the defense system of the body, and to release the drug at its destination. Thereby, side effects or damage on healthy cells shall be reduced and cellular treatment shall be limited to the target cells. However, in reality, the design of such a drug delivery device is non-trivial due to manifold requirements on the system. Amongst others, the nanoparticle as a carrier system should show low toxicity and be metabolized and eliminated quickly after cargo delivery.

Immense efforts are undertaken to develop drug delivery systems for the treatment of cancer [4]. This is of great importance as cancer is and will remain one of the most common causes of death. The WHO prognoses an increase in cancer-caused deaths of up to 9 millions in the year 2015 and 11.4 millions in the year 2030 [5]. In addition, cancer therapies are limited to a combination of surgery, radiation, and chemotherapy. For this reason, great hope is pinned on the development of new drug delivery devices which could especially help in chemotherapy.

For drug delivery, various nanoparticle designs have been established, mainly based on polymers and liposomes. In addition, inorganic nanoparticles, such as silica nanoparticles, have been developed. This study concentrates on colloidal mesoporous silica (CMS) nanoparticles. They are particularly interesting due their large surface area and pore volume leading to an efficient encapsulation of high amounts of guest molecules [6–8]. In addition, CMS nanoparticles can be functionalized at will [9]

and form stable colloidal suspensions [10].

Due to these advantages, CMS nanoparticles have been investigated intensively by various research groups. Although there are multiple synthesis and *in vitro*-functionality studies of CMS nanoparticles, detailed investigations on the mechanism of action in living cells, regarding cellular uptake, intracellular processing and function, are oftentimes missing. To fill this gap of knowledge, highly-sensitive fluorescence wide-field and spinning disk confocal microscopy on a single-cell level are powerful tools. Using these methods, we were able to observe the uptake, intracellular trafficking and drug delivery processes of single nanoparticles in real-time. These insights enable evaluation and continuous improvement of the CMS nanoparticles for drug delivery.

As drug delivery is a multi-step process, the nanoparticles have to fulfill certain demands on the target-cell level. One demand on the drug delivery vehicle is to attach to the target cell and to be internalized. In this work, we therefore studied the internalization time scale of CMS nanoparticles equipped with a polyethylene glycol (PEG)-shell into living cervix carcinoma cells (HeLa). The PEG coating shields the nanoparticle to avoid elimination of the nanoparticles from the body before reaching the target cell. This increases the nanoparticle's lifetime in the blood circulation [11].

Another demand of major importance is the high drug-loading into the CMS nanoparticles and pore sealing to protect the drug from the external milieu. For this reason, we loaded fluorescent dyes and (model-) drugs by incubation of the CMS in a drug-containing solution (drug adsorption). After adsorption of the drugs, the pores were sealed by a supported lipid bilayer. Drug delivery of the loaded substances to liver cancer cells (HuH7) has then been monitored by live-cell imaging.

A third demand involves controlled site-specific and stimuli-responsive release of the drug from the carrier. To achieve this, we exploited two external stimuli: changes in redox-potential and light irradiation. In the first study, the amino acid cystein was bound to the inner volume of the nanoparticle via a redox-cleavable disulfide linker. Upon internalization into the reducing milieu of the cytoplasm, this disulfide bridge was supposed to be cleaved setting free the cysteine. To support endosomal escape photochemical internalization (PCI) was used for delivery of cysteine into the cytoplasm. In a next step, to achieve a more precise, "surgical" function of photoinduced endosomal release and to minimize the toxicity of the nanoparticles on cells, we used a covalently surface-bound photosensitizer (PpIX) on CMS and coated the drug-loaded nanoparticles with a supported lipid bilayer. We studied the drug delivery processes after light irradiation in great detail by fluorescence live-cell imaging.

This thesis is structured as follows:

The introductory chapter (Chapter 1) is followed by three further chapters covering the theoretical background and status quo of the research fields that influenced this work.

Chapter 2 describes the principles of nanomedical drug delivery, with an introduction into uptake and trafficking of nanoparticles in cells and an overview about commonly used drug delivery systems. Chapter 3 focuses on the drug delivery system used in this work, which is colloidal mesoporous silica (CMS). The material class will be introduced along with the synthesis strategies developed by and used in the group of Prof. Thomas Bein. Subsequently, the demands on CMS nanoparticles

as drug delivery system will be explained along with considerations regarding the biocompatibility. Chapter 4 describes the principles of fluorescence and the phenomena of bleaching and quenching. The fluorescence microscopy set-ups are explained as well as the benefits of fluorescence microscopy in living cells.

Following the chapters on theory, the experimental methods are described in Chapter 5.

In Chapters 6 to 9, the results and discussions of our studies are presented in a partly cumulative manner. Chapter 6 describes the experiments concerning the internalization dynamics of CMS nanoparticles into living cells. Chapter 7 presents, in its first part, results on drug delivery by lipid bilayer-coated CMS nanoparticles loaded with colchicine, an anti-cancer drug. The results described in this chapter are published in Nano Letters [12]. In the second part of the chapter, additional experiments investigate the influence of the lipid bilayer composition on CMS nanoparticle uptake into cells. In Chapter 8 disulfide-based drug delivery and the role of photochemical internalization is presented. The study is published in Nano Letters [13]. To induce photochemical release in a more locally confined manner, we studied CMS nanoparticles with covalently surface-bound PpIX and its interaction with living cells. This study is presented in Chapter 9 and submitted for publication [14]. At the end of each chapter a summary of the main results is provided.

2 Principles of nanomedical drug delivery

Many diseases such as cancer are linked to changes in biological processes at the molecular level [15]. These changes can be caused by mutated genes, misfolded proteins and viral or bacterial infections. To specifically treat these diseases at the molecular level, nanotechnology with materials, especially particles in the 1-1000 nm range, has contributed significantly [16]. As an offshoot of nanotechnology, the discipline nanomedicine involves "highly specific medical interventions at the molecular scale for curing diseases or repairing damaged tissues" [17]. Nanomedicine as a discipline is subdivided into different fields, one of it being novel drug delivery systems [18, 19]. These systems are currently subject of immense research efforts, especially for the treatment of cancer.

Conventional cancer treatment involves the application of small molecule cytostatics for chemotherapy. However, these drugs lack selectivity for cancer tissue leading to considerable toxicity to healthy tissue and are prone to cause multidrug resistances in cancer cells [20]. To solve these and other issues, cancer drug delivery has been introduced. Drug delivery involves a pharmaceutical carrier, called nanoparticle, associated with a drug [21, 22]. Nanoparticles are useful, as they represent intracellular drug depots with sustained release profiles and protect the drug against degradation [23]. In addition, nanoparticles have the ability to be internalized into cells without being recognized by efflux transporters, main mediators of multidrug resistance such as multi-drug resistance proteins and P-glycoproteins [24].

Commonly used drugs range from nucleic acids (plasmid DNA, siRNA and antisense oligonucleotides) [25, 26]) to small molecule drugs, proteins or imaging agents [27]. Drug delivery can be achieved even with drugs showing poor water solubility [28]. Some of the novel drug delivery systems have already been approved by the Food and Drug Administration (FDA), such as Doxil, liposome-encapsulated doxorubicin with a polyethylene glycol (PEG) coat for treatment of ovarian cancer and multiple myeloma [20].

Our work focuses on nanometric drug delivery systems for cancer therapy. To evaluate the drug delivery mechanism on the level of individual cancer cells, the interaction of drug-loaded nanoparticles with cancer cells have to be studied [1, 2, 29, 30]. These processes include uptake of the nanoparticles into the cells, intracellular trafficking and controlled drug release into the cell.

In the following, the state of knowledge about nanoparticle uptake and intracellular trafficking will be described. Afterwards, an introduction into commonly used nanoparticle designs will be given.

2.1 Uptake and trafficking of nanoparticles in cells

To administer drug delivery systems into the human body, several modes including oral application, inhalation, intravenous and intraperitoneal injection are used [27]. Depending on the mode of

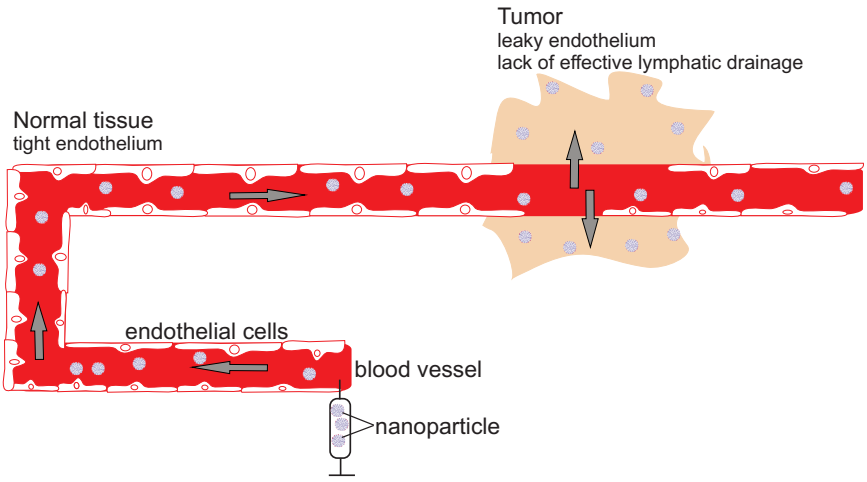

Figure 2.1: Passive tissue targeting by the enhanced permeability and retention (EPR) effect. Enhanced permeability of the tumor vasculature and ineffective lymphatic drainage leads to extravasation and accumulation of nanoparticles in tumor tissue. Figure adapted from [31].

administration, different types of barriers have to be crossed to reach the tumor tissue under minimum loss of quantity and activity **(accumulation at the target tissue)**. In subsequent steps, nanoparticles should selectively internalize into diseased cells without affecting healthy cells [24] **(cellular internalization)**, get transported to the site of action and release their cargo efficiently **(intracellular transport and endosomal release)**.

2.1.1 Accumulation at the target tissue

Nanoparticles can accumulate either passively in tumor tissue or by active tumor targeting [32]. This two accumulation modes will be discussed in the following.

Passive accumulation of nanoparticles in tumor tissue is mediated by the enhanced permeability and retention (EPR) effect [33]. This effect is a feature of many tumors and was first described by Matsumura *et al.* [34]. Nanoparticles, running with the blood flow, extravasate into the surrounding tumor tissue through the endothelial cell layer that exhibits holes. The holes enable macromolecules or nanoparticles smaller than 400-600 nm [35] to pass. The defective vascular architecture is a result of rapid tumor growth [31, 36] and consequential need for increased supply with nutrients via the blood flow. To supply the tumor with nutrients additional tumor vasculature is formed rapidly and with a lack of a tight endothelial cell layer. In addition, poor lymphatic drainage extends the residence time of extravasated substances in cancer tissue [37]. A schematic representation of the EPR effect can be found in Figure 2.1. Despite the positive effects of EPR on nanoparticle drug delivery, the EPR effect has its limitations. The permeability of vessels is not homogeneous throughout a tumor and certain tumors show no EPR effect [31]. Therefore, an alternative involves physical targeting of e.g. magnetic nanoparticles that are accumulated at the target site by magnets [38]. Once at the target site or tissue, active targeting strategies on a single cell level are beneficial

to accumulate drugs specifically in tumor cells.
Active targeting strategies for specific tumor-cell accumulation are based on the incorporation of targeting ligands into particles. The ligands bind to cell type specific receptors expressed on cell surfaces promoting active cellular uptake [39]. Active targeting has been investigated intensively. A list of applied ligand-receptor pairs can be found in Wagner *et al.* [40]. Taken together, a combination of passive and active targeting is useful for drug delivery to the cancer cell environment.

2.1.2 Cellular internalization

After reaching the cancer cell environment, the nanoparticle needs to be delivered to the specific sub-cellular region where its drug cargo is effective. Some drugs require intracellular delivery to tumor cells or to tumor initiating cells [20]. Therefore, it is of great importance to know about uptake, intracellular trafficking and fate of nanoparticles on a single-cell level. Depending on the internalization mode of nanoparticles into cells, their intracellular fate will differ considerably. The most common mode of uptake into mammalian cells is endocytosis. This process is characterized by the internalization of nanoparticles into membrane-bound vesicles (endosomes), formed by invagination and subsequent pinch-off [41]. Endosomes deliver cargo to specialized structures for sorting, where the cargo is directed towards intracellular compartments or recycled to the extracellular milieu [42]. In current nomenclature, two different classifications of uptake pathways have been proposed. One is based on the proteins involved in the endocytic pathway (e.g. clathrin-mediated endocytosis, caveolae-mediated endocytosis clathrin-and caveolae independent endocytosis and macropinocytosis). The size of the endosomes differs from 50 nm in caveolae-mediated endocytosis to as large as 5 µm in macropinocytosis [41, 43].
In this work, we will distinguish uptake modes according to the second classification. In this classification, different internalization stimuli on the cell membrane give rise to fluid-phase, adsorptive and receptor-mediated endocytosis [44].

Fluid phase endocytosis is, in contrast to adsorptive and receptor-mediated endocytosis, a low-efficiency and non-specific process. In this process solutes are taken up in their extracellular concentration [44]. Fluorescent dextrans are, for example, suitable markers of fluid phase pinocytosis [45]. However, in case of nanoparticle uptake, fluid phase endocytosis is not as relevant as receptor-mediated and adsorptive endocytosis.

Adsorptive endocytosis is initiated by unspecific interaction of, in our case, nanoparticles with binding sites on the cell membrane, such as lectin or heparan sulfate proteoglycanes. The latter are negatively charged and play an important role in electrostatic interactions [46]. Electrostatic interactions with the plasma membrane in general are mediated by the membrane potential of -30 to -60 mV [47, 48], leading to better association of positively charged nanoparticles with the plasma membrane [49]. The nanoparticles are concentrated on the cell surface and internalized together with the membrane region they are interacting with. For a schematic representation see Figure 2.2a.

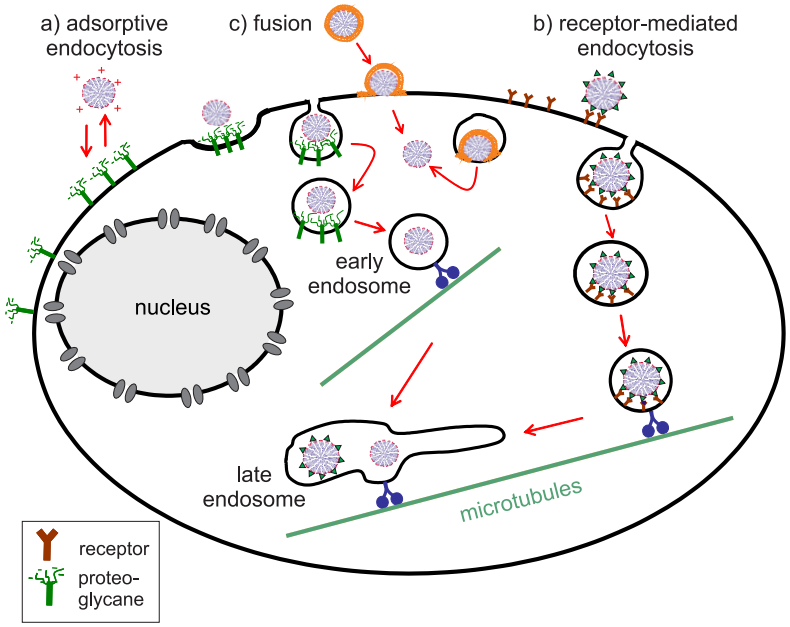

Figure 2.2: Uptake and intracellular trafficking of nanoparticles in cells. (a) Adsorptive endocytosis, (b) receptor-mediated endocytosis and (c) fusion with the plasma membrane are possible modes of internalization of nanoparticles into cells. In addition, nanoparticles can fuse with the endosomal membrane. Adapted from a figure provided by the courtesy of Dr. Nadia Ruthardt.

Receptor-mediated endocytosis occurs after binding of specific ligands on the particle surface to receptors on the cell membrane. Receptors overexpressed on cancer cells are, for example, the transferrin receptor (TFR) [50], the folate receptor [51] or the epidermal growth factor receptor (EGFR) [52]. Ligand binding to the receptor is followed by cell entry into endocytic vesicles [41, 53] (see Figure 2.2b). Upon extracellular receptor-binding of the epidermal growth factor (EGF), signal transduction to intracellular space is activated triggering a multitude of biochemical pathways including those leading to internalization [54]. To further increase efficiency and specificity, dual-receptor targeting has been exploited for the delivery of polyplexes (polycation complexed with anionic nucleic acid). Nie *et al.* equipped polyplexes with the transferrin receptor targeting peptide B6 and an arginine-glycine-aspartic acid (RGD)-containing peptide for integrin targeting [55].

Fusion of lipids or peptides with the plasma membrane is an internalization mode that bypasses endosomal uptake (see Figure 2.2c). Fusion of lipid bilayers is assumed to occur in a two-step process, where first the electrostatic repulsion of membranes in close proximity need to be overcome and then non-bilayer transition states are generated [56]. Studies by Felgner *et al.* suggested lipoplex (cationic lipid complexed with anionic nucleic acid) mediated gene delivery by fusion of the lipids with the cell membrane [57, 58]. However, later studies found a more pronounced effect of endocytosis on cellular uptake [59]. Verma *et al.* managed to achieve particle fusion on the plasma membrane by coating gold nanoparticles of 6 nm diameter with a shell of hydrophobic and anionic

ligands regularly arranged in ribbon-like domains of <6 Å width. These nanoparticles penetrate cell membranes without evidence of membrane disruption [60]. However, endocytosis is a more frequently used uptake mode for nanoparticles, whereas viruses seem to undergo fusion more often. Stimuli for enveloped virus-fusion on the plasma membrane can be low pH, processing of the fusogen precursor, binding to a receptor or a combination [61]. In addition to fusion on the plasma membrane, fusion with the endosomal membrane is possible as well [62]. It is important to note, however, that not all drugs would benefit from fusion-mediated cytosolic delivery as the cytosolic milieu is crowded and motility of substances delivered to the cytosol is strongly impaired depending on their size, structure and charge [63].
In case of endocytosed nanoparticles, it is important to understand the mechanisms of intracellular trafficking and endosomal release. These two topics will be discussed in the following.

2.1.3 Intracellular trafficking

Prior to internalization, nanoparticles attach to the cell membrane. The dynamics of the nanoparticles during membrane association can be characterized by slow, directed transport on the plasma membrane with velocities of 0.015 µm/s and diffusion coefficients of D = 2-4 $\times 10^{-4}$ µm^2/s, as assessed for magnetic lipoplexes of 390 nm diameter and epidermal growth factor (EGF)-equipped polyplexes of 270 nm diameter on living HuH7 cells [2, 30]. After attachment, the nanoparticles are internalized via endocytosis and confined in early endosomes. The milieu in the endosome in contact with the nanoparticles undergoes a drop in pH from extracellular tumor milieu of 6.6-7.0 (in healthy tissue pH 7.2-7.4) [64–66] to intracellular pH 5.9-6 [67]. In this phase, the dynamics of the nanoparticles trapped in endosomes is characterized by anomalous and confined diffusion in the crowded cellular interior with confinement diameters of 0.1-2 µm for both lipoplexes and polyplexes. Later on this phase is replaced by active transport of the nanoparticle-filled endosomes along microtubules with velocities of 0.5-0.7 µm/s [2, 30]. After maturation from early to late endosomes the pH changes to pH 5-6 [67]. Late endosomes were shown to fuse with lysosomes where cargo degradation takes place [41, 53]. This fusion was shown to take place preferably in the juxtanuclear region of the cell near the microtubule-organizing center [68]. The lumenal environment in lysosomes shows pH 5-5.5 [67] and contains acid hydrolases [68].
Although endocytosis is a rather efficient uptake route into cells, internalized molecules have a low availability at the side of action, for example the cytosol or nucleus, as they remain entrapped in endo/lysosomes. Therefore endosomal escape is one major prerequisite for successful drug delivery.

2.1.4 Endosomal release

To gain access to the cytosol or the nucleus and to prevent degradation, the internalized nanoparticles need to overcome endosomes or lysosomes. In the following section, mechanisms for endosomal escape are described. These mechanisms include pH buffering effects, fusion with the endosomal membrane and photochemical disruption of the endosomal membrane.
To take advantage of pH-buffering effects for endosomal escape, agents with high buffering capacity

combined with the flexibility to swell in protonated state are essential [69]. Polyamines with titratable secondary and tertiary amines in the physiological pH range, as found in polyethyleneimine (PEI), show high H^+ buffering capacity during acidification of the endosome. The buffering effect leads to increased H^+ pumping and concomitant Cl^- influx into the endosome to maintain charge neutrality. The increased ionic strength leads to water influx, osmotic swelling and endosomal rupture [70–73]. This model is described as "proton sponge effect" [74]. Recently, Yue *et al.* proposed that the "proton sponge effect" plays a role, however, not the dominant role for endosomal escape [75]. In their model, free cationic PEI chains, present after polyplex assembly, help to release polyplexes from endosomes. The free cationic PEI chains get embedded inside the anionic cell membrane via electrostatic interactions and lead to destabilization of the endosomal membrane. In addition, cationic PEI chains sticking-out from the loaded endosome prevent the formation of endo/lysosomes.
Another strategy for endosomal escape involves destabilization of the endosomal membrane by fusion that can be induced by the pH sensitive fusogenic lipid dioleoyl-phosphatidylethanolamine (DOPE). DOPE forms stable lipid bilayers at physiological pH, but changes to a hexagonal structure at pH 5-6. This inverted hexagonal structure can fuse with the endosomal membrane and destabilizes it [76, 77]. As another mediator of fusion, the pH sensitive hemagglutinin subunit HA-2 derived from influenza virus can be used. This peptide undergoes conformational changes at low pH and perturbs the endosomal membrane [78].
A further endosomal escape strategy is light-induced disruption of the endosomal membrane, a method called photochemical internalization (PCI) [69]. This method involves incubation of cells with a photosensitizer. The photosensitizer interacts with the cell membranes and is internalized. Intracellular localization of a photosensitizer is dependent upon its chemical properties (hydrophobicity, charge or amphiphilic character) and size [79]. A photosensitizer that localizes in the endosomal membrane is disulfonated *meso*-tetraphenylporphine ($TPPS_{2a}$). Upon exposure to light, $TPPS_{2a}$ induces photochemical reactions that lead to rupture of the vesicular membranes followed by release of the endosomal content into the cytosol [80]. PCI is a promising strategy for the application in site-specific drug delivery [81] and has been applied for the delivery of genes [30, 82] or other drugs [83]. However, the application of PCI is limited by the tissue's strong light absorption. Reduced tissue absorption is only observed in the range of 800 - 1200 nm light [84]
For the design of a nanoparticle for successful drug delivery, knowledge about uptake, intracellular trafficking and endosomal escape is essential. In the following, the most common nanoparticle types for drug delivery will be introduced briefly.

2.2 Nanoparticle designs for drug delivery

To design a successful nanoscale drug delivery system, sophisticated materials are available. These materials include polymers, dendrimers and lipids that can be assembled into nanocarriers to enhance the payload and solubility of drugs. In addition, inorganic materials such as ceramics or metals and metal oxides exhibiting unique optical and magnetic properties are promising materials for drug delivery. This section introduces different types of nanoparticulate delivery systems employed for

drugs in the field of nanomedicine with a short overview of their advantages and disadvantages.

2.2.1 Polymeric nanoparticles

Polymeric nanoparticles have been used for gene delivery [85, 86] and delivery of other drugs [16, 87]. They can be prepared from a wide range of materials such as PEI, chitosan, gelatin and FDA-approved polylactic acid (PLA) and poly(lactic-co-glycolic acid) (PLGA) in various designs. The cargo is electrostatically or physically entrapped in, or attached to the polymer matrix [88]. One example of a successfully used polymer in drug delivery is polyethylene glycol (PEG). PEG is used as a coating of nanoparticles and reduces plasma protein adsorption and phagocytosis of nanoparticles by cells of the reticulo endothelial system (RES) [23]. Most polymer materials show a good biodegradability and biocompatibility as well as good pharmacokinetic control [23]. Possible disadvantages of polymeric nanoparticles are that large-scale production and manufacturing remains an issue [23], that there are still cytotoxicity problems with some polymers [89], e.g. PEI, and that their drug carrying capacity is comparably low [87].

2.2.2 Lipid-based nanoparticles

Besides polymeric nanoparticles, lipid-based nanoparticles play an important role for drug delivery. This widely used system is able to load polar molecules to the lipid bilayer's aqueous core or absorb nonpolar drugs within the hydrophobic bilayer [90]. The term lipid-based nanoparticles comprises a variety of different designs including, among others lipoplexes (cationic lipid-nucleic acid complex) [77, 91, 92] and liposomes [90]. Liposomes are spherical bilayered vesicles with a phospholipid membrane surrounding a central aqueous space [24, 93]. Liposomes combine ease of surface functionalization with a good biocompatibility profile. They can be loaded with hydrophilic and hydrophobic pharmaceuticals, have a high drug carrying capacity [94] as well as adjustable size, charge and surface properties [23, 87, 93]. However, some drawbacks exist. Liposomes are eliminated from the blood rapidly and captured by cells of the RES [93]. In addition, they show low stability in biological media [23].

2.2.3 Viral nanoparticles

Viral nanoparticles are virus-based nanoparticle formulations that can be infectious or noninfectious [95]. Examples for viral nanoparticles include the cowpea mosaic virus, cowpea chlorotic mottle virus, bacteriophages [96] and recombinant adenovirus [97]. The capsid surface can be modified using chemical or genetic means to display targeting molecules and peptides in a biologically functional form [24, 98]. The high delivery efficiency, regular geometries, well-characterized surface properties, nanoscale dimensions and their structure known to near atomic resolution are advantageous. However, for a safe application of viral nanoparticles as nanocarriers *in vivo*, immunogenicity is an issue and it is essential to gain a better understanding of the fate and potential long-term side effects [95].

2.2.4 Inorganic nanoparticles

Inorganic nanomaterials as drug delivery systems consist of nanoparticles based on semiconductors, so-called quantum dots, metals (such as gold and silver), and metal oxides (such as iron oxide and silicon dioxide) [99]. These materials provide a robust framework for further modifications [7]. One promising example is gold nanostructures that are used to generate significant heat within tumors (hyperthermia) and therefore selectively increase the delivery of macromolecules with therapeutic anti-cancer drugs [100]. General advantage of inorganic nanoparticles is the stability over high temperature and pH range, but the lack of biodegradation and slow dissolution raises safety questions [23]. Silica nanoparticles also belong to the class of inorganic nanoparticles with extremely promising properties. As this material is of major importance for this work, the following chapter focuses on it.

3 Colloidal mesoporous silica (CMS) nanoparticles

Colloidal mesoporous silica (CMS) nanoparticles are highly promising candidates for the delivery of diagnostics or therapeutics to diseased cells and have been studied as drug delivery system throughout this work. Therefore, the following section will be focused on this material class. First, a general introduction into mesoporous silica materials is given, followed by an explanation of the CMS nanoparticle synthesis. As CMS nanoparticles are studied extensively in various research groups, an overview of the studies on CMS nanoparticles for drug delivery and on their biocompatibility is provided.

3.1 Mesoporous silica materials

Porous solids with ordered structure have been established from a variety of different materials, but silica is the most common. Microporous structures are defined to show pore diameters of <2 nm, whereas mesoporous materials contain pore diameters of 2-50 nm [101]. In 1992, the innovative synthesis method of Kresge *et al.* using aluminosilicates in the presence of a surfactant as a structure-directing agent, enabled to achieve porous material with uniform pore diameters in the mesoscale and narrow pore-size distributions [102]. This breakthrough revolutionized the field of mesoporous materials. The reason for mesoporous silica to be such an attractive material can be attributed to their uniform pore diameter, large surface area, high chemical and thermal stability, and to the ability to be functionalized at will [103, 104]. Their properties render mesoporous materials useful for a variety of applications, such as catalysis [105], chemical separations [106, 107] and biomedical applications such as implants for bone tissue engineering [108] or drug delivery [109, 110]. Mesoporous materials appear in multiple morphologies, for example thin films [111], powders [112] as well as micro- and nanoparticles in various shapes [113].
In this work, we focus on mesoporous silica nanoparticles for drug delivery. The nanoparticles were developed and synthesized by Dr. Valentina Cauda, Dr. Axel Schlossbauer, Christian Argyo and Alexandra Schmidt from the group of Prof. Thomas Bein (LMU Munich).

3.2 Synthesis of CMS nanoparticles

Colloidal mesoporous silica (CMS) nanoparticles can be described as solid, amorphous silica nanomaterials in suspension with hundreds of empty, mesoporous channels arranged in a porous structure

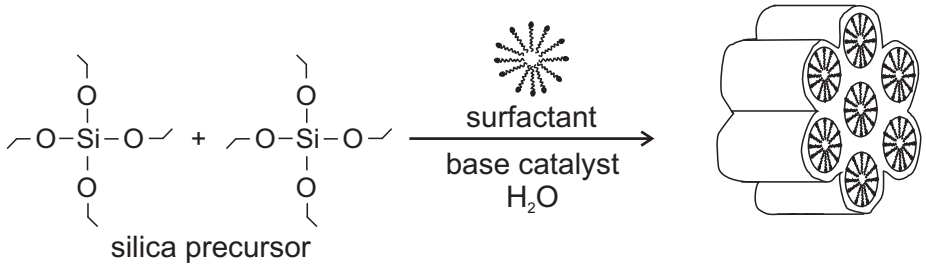

Figure 3.1: Cooperative self-assembly of silica precursors around surfactant micelles. Figure adapted from [106].

[114]. Due to their colloidal stability in certain media [115], biocompatibility [116, 117], degradability in living tissue [118], high loading capacity of guest molecules [12, 119, 120], improved pharmacokinetics and controlled release kinetics, CMS nanoparticles are of high interest for nanomedical applications.

In the following, the synthesis of CMS nanoparticles used throughout this study will be explained. The synthesis is based on cooperative self-assembly of silica precursors around a surfactant template under basic conditions (see Figure 3.1). The organic surfactant acts as a template and structure-directing agent introducing the well-defined and uniform mesopore morphology which is one of the major concerns in CMS synthesis. To limit the particle size the polyalcohol triethanolamine (TEA) was used as a complexing agent for silicate species and additionally as an encapsulator for mesoporous particles [10]. In addition, the use of organo-functionalized silane together with the silica source allows the introduction of chemical functional moieties throughout the porous silica surface. To achieve multiple functionalities within one particle, the group of Prof. Thomas Bein developed the delayed co-condensation approach [9]. In this work, two different particle-types, which were further modified, have been synthesized for this work: outer-shell functionalized CMS and core-shell functionalized CMS. Both synthesis strategies will be explained briefly in the following.

3.2.1 Outer-shell functionalized CMS

To synthesize outer-shell functionalized CMS [9], the silica source (e.g. tetraethyl orthosilicate, TEOS) is mixed with triethanolamine (TEA). The reaction mixture is heated for 30 min at 90°C without stirring. In parallel, the precursor cetyltrimethylammonium chloride (CTAC) solution in water is prepared and heated to 60°C. The CTAC solution is added to the TEOS/TEA mixture and stirred at 500 rpm for 20 min (see Figure 3.2a, first step). During this step silicate polyanions assemble at the positive charges of the cationic surfactant headgroups, which are forming micelles. The surfactant packing and therefore the pore topology is dependent on the volume of the surfactant, the headgroup area at the micelle surface and the length of the surfactant tail [121]. In case of the CMS nanoparticles, the resulting pores in the central areas of the particles are worm-like and radially diverging towards the boundary of the particles [10]. The mesostructure is formed by continuous crosslinking and polymerization of the silica species. If an amino-functionality at the CMS shell is

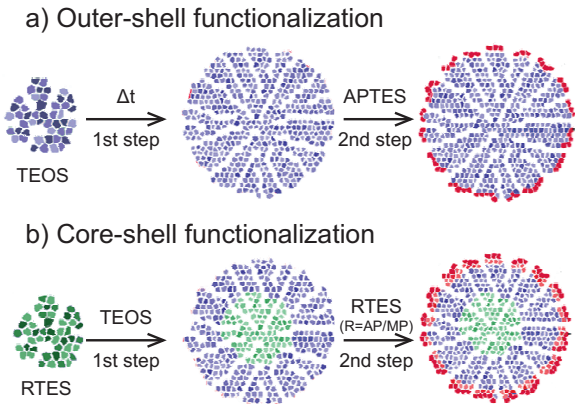

Figure 3.2: Synthesis of multiple core-shell functionalized CMS nanoparticles (a) CMS nanoparticles with amino-groups on the outer surface (red dots) achieved by a delayed co-condensation approach. (b) Multistep co-condensation reaction of CMS nanoparticles, where first the inner functionalization (green dots) was obtained, followed by a silica layer (blue dots) and the outer-shell functionalization by another trialkoxysilane (red dots). This procedure leads to functional groups within the particle volume depending on the addition time of the RTES. Figure adapted from [9].

desired, a functionalized trialkoxysilane, in our case (3-aminopropyl)-triethoxysilane (APTES), was added to the reaction mixture in combination with TEOS at a molar ratio of (1:1) 30 min after the beginning of the reaction. The resulting mixture was left to stir overnight at room temperature (see Figure 3.2a, second step). The sample was centrifuged, redispersed in ethanol, and extracted. For more details, please see Cauda *et al.* [9].

3.2.2 Core-shell functionalized CMS

As a second particle-type, used in this study, core-shell functionalized CMS were synthesized [9]. To obtain a functionalized core, TEOS was incubated together with TEA and the functionalized trialkoxysilane (RTES, in our case (3-aminopropyl)-triethoxysilane (APTES) or (3-mercaptopropyl)-triethoxysilane (MPTES)) at 90°C for 20 min. The 60°C -heated CTAC solution was added and the resulting mixture was stirred at 500 rpm for 20 min. After this synthesis step, an unfunctionalized silica layer was realized by multiple addition of small portions of TEOS to the reaction mixture and continued stirring for 40 min (see Figure 3.2b, first step). To functionalize the outer shell of the CMS a mixture of TEOS and another functionalized trialkoxysilane (1:1) was added and the reaction mixture was stirred at room temperature overnight (see Figure 3.2b, second step), centrifuged, redispersed in ethanol, and extracted. For more details, please see Cauda *et al.* [9].

3.2.3 Template extraction

To make the pores accessible after successful synthesis, it is necessary to remove the organic template. In our case, the template was extracted by heating the colloidal suspension in ethanolic ammonium nitrate solution to 90°C for 45 min under reflux [9]. Ammonium is a very efficient extraction reagent, as it has high similarity with the template headgroups [122]. Subsequently, a washing step in ethanol followed by centrifugation was performed. In a second step the suspension was kept in ethanol/hydrochloric acid solution for additional 45 min and was afterwards washed in ethanol.

3.3 CMS nanoparticles as drug delivery vehicles

The described synthesis leads to well-defined CMS nanoparticles of 50-80 nm with a wormlike mesoporous structure, pore diameters of about 3.7 nm and site-specific functionalities. These functionalities can be further modified to meet the requirements of drug delivery devices. The first requirement is that the nanoparticles should have high drug loading capacity and the loaded substances should be protected from external milieu to avoid cargo destruction (**drug loading**). Second, the loaded substances should show zero premature release and remain inside the drug carrier during transport to the target side (**pore sealing**). Third, the drug delivery vehicle should be taken up by the target cell efficiently (**cancer cell targeting**). Fourth, drug delivery should occur in a site-specific and stimuli-responsive manner (**stimuli-responsive release**). Fifth, the drug delivery vehicle has to be biodegradable and biocompatible and has to be excreted/degraded by the patient after it achieved successful drug delivery (**degradation and nanotoxicity considerations**). The aforementioned requirements will be further addressed in the following.

3.3.1 Drug loading

To load high quantities of drugs into CMS nanoparticles, two different strategies can be applied. On the one hand, the drug of interest can be covalently linked to the nanoparticle (e.g. by click chemistry [123] or disulfide linkage [13, 124]), on the other hand drugs can be simply loaded by incubation of CMS in a drug solution (adsorption) [125]. In the latter case, the amount of drug loaded in the porous matrix depends on multiple factors such as the solvent, the pH and the drug concentration used during CMS incubation with the drug, the pore size of CMS and functionalization of the pore walls [126]. For a controlled adsorption of the drug, the choice and modulation of adequate electrochemical surface properties is important [127].
Generally, both hydrophilic and hydrophobic drugs can be loaded into mesoporous silica nanoparticles (MSN). Various cargos have been loaded and published, including genetic information encoded in DNA and (si)RNA [128], quantum dots [128], toxins [128] and pharmaceuticals (vancomycin [129], ibuprofen [125], telmisartan [130]). For cancer treatment, cytostatics such as colchicine [12], camptothecin [131], doxorubicine [128, 132, 133], cisplatin [128] and 5-fluoruracil [128] are relevant drugs for CMS loading. In addition, neurotransmitters (adenosine triphosphate (ATP) [129]) or second messenger (cyclic adenosine monophosphate (cAMP) [134]) and model-drugs such as membrane-impermeable proteins (cytochrome c [119]), dyes (propidium iodide (PI) [131, 135], DiI/DiO [136], rhodamine B [137], safranine O [138], fluorescein [139–141]) as well as dye-labeled dextran e.g. 40 kDa FITC-dextran [142] have been tested as cargos and loaded into the pores.

3.3.2 Pore sealing

After drug loading, it is essential to avoid pre-mature drug leakage from the carrier, as this might induce systemic toxic effects. Therefore, a number of strategies for pore sealing have been developed. One important strategy is capping of the entire CMS nanoparticle by a supported lipid bilayer (SLB) as reported by Brinker *et al.* [128, 143, 144] and Bein *et al.* [12]. In the latter publication, the SLB

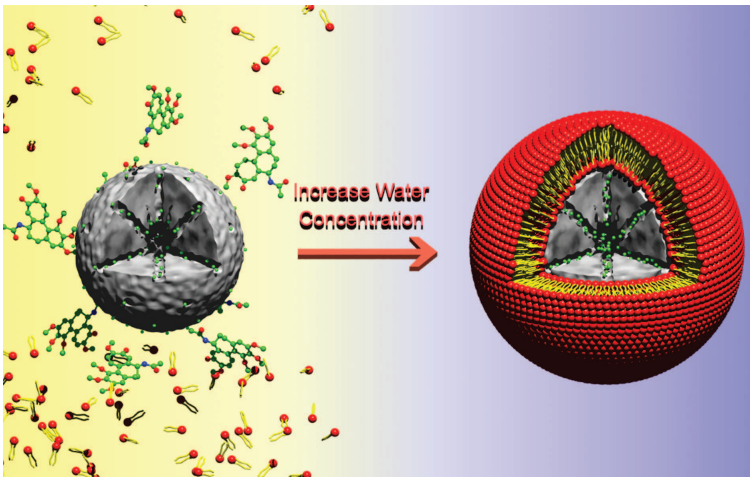

Figure 3.3: Pore sealing of CMS by a supported lipid bilayer (SLB). SLB are deposited on functionalized colloidal mesoporous silica (CMS) nanoparticles, resulting in a core-shell hybrid system (SLB@CMS). The supported membrane acts as an intact barrier against the escape of encapsulated substances. Figure taken from [9].

is built via solvent exchange by increasing the water content in the ethanolic suspension containing lipids and nanoparticles. The nanoparticles are enclosed and the membrane-impermeable cargo inside the pores is prevented from release (see Figure 3.3). This promising strategy has been applied in our own research and will be presented in Chaper 7 of this thesis.

Another strategy involves the use of peptides or proteins on the opening of the pores. Schlossbauer *et al.* reported on a biotin-avidin cap system [140]. Zhao *et al.* blocked the pore openings with insulin proteins [134]. Climent *et al.* used antibodies [145] and Luo *et al.* collagen [146] as a nanoscopic cap. Coll *et al.* took advantage of a peptide shell to reduce premature release [147]. Pore sealing was also achieved by inorganic nanoparticles as "gate-keepers", including CdS nanocrystals [129] or gold nanoparticles [138, 139, 141]. Also polymers [136, 148], dendrimers [132], sugar [149] and DNA double strands [150] have been used. A variety of strategies developed by Zink *et al.* include complex, supramolecular assemblies for pore sealing [131, 135, 137, 151–159].

3.3.3 Cancer cell targeting

Selective cancer-cell targeting is a important task, as anti-cancer drugs have severe side-effects caused by unspecific action on healthy cells. Therefore, receptors overexpressed on cancer cells can be targeted by nanoparticles, leading to efficient internalization of the drug carriers by receptor-mediated endocytosis (for details on the cellular uptake pathways, please see Chapter 2.1). Receptor-targeted MSN have been synthesized by many groups.

Most studies were performed using the specific interaction of folic acid with the α-folate receptor upregulated in various types of human cancers. Zink and coworkers showed the synthesis of MSN with an iron oxide core and surface grafted folate-silanes. They observed increased particle uptake into a pancreatic cancer cell line (PANC-1) compared to non-cancerous cells [7]. In another study, folic acid has been bound to a polyethyleneimine (PEI) shell. Cell culture studies show that the total number of particles internalized by folate-receptor overexpressing cells was about an order of magnitude higher compared to control cells with a low number of folate-receptors [160]. Similar studies on folic acid-functionalized MSN have been performed by other groups [161, 162].

Another receptor-ligand is lactobionic acid (LA) which binds specifically to the asialoglycoprotein receptor (ASGP-R) on the surfaces of hepatoma cells. Endocytosis efficiencies into HepaG2 (human liver hepatocellular carcinoma cell line) cells were shown to be three times higher for LA-MSN compared to untargeted MSN after 2 hours [146].
In a very recent study by Zink *et al.*, the cyclic RGD peptide and the protein transferrin have been covalently bonded to MSN and hydrophobic drug delivery of the anti-cancer drug camptothecin has been achieved [163]. Another recent study by Brinker *et al.* applied a SLB on CMS containing targeting peptides (SP94) and fusogenic peptides (H5WYG) and showed successful receptor targeting and cargo delivery [128]. Monoclonal antibody-functionalized (anti-HER2/neu mAb) MSN have successfully targeted breast cancer cells [164].
In addition, cancer cell-specific DNA aptamers, single strand nucleic acids that bind to their target molecules with high affinity and specificity, have been presented as targeting ligand on MSN. The aptamer binds to its target protein, the human protein tyrosine kinase-7, present on some tumor cells surfaces (e.g. on HeLa cells). Upon binding, aptamer-MSNs show highly efficient aptamer-mediated endocytosis [165].
Some studies show uptake of MSN upon binding to the mannose receptor. For example there is mannose on a photosensitizer (anionic porphyrin) that is covalently linked to MSN [166], mannosylated PEI-coupled MSN [167] and MSN methotrexate, which binds to the mannose receptor and is in addition a cytostatic [168].

3.3.4 Stimuli-responsive release

After CMS drug loading, pores are sealed and the nanoparticles internalize specifically to cancer cells. As a final step, release of the loaded drug is an important challenge. This is due to the toxicity and severe side-effects induced by these drugs on healthy tissue. Therefore, these drugs should be delivered with control over the space and time of the release process, preferably upon a defined stimulus. Several groups have reported upon stimuli for controlled release. The triggers of stimuli-responsive drug release include competitive displacement, magnetic field, enzymatic digestion, changes in temperature, pH, redox-potential and light irradiation. The triggers will be addressed in more detail in the following.

Competitive displacement

Competitive displacement is a trigger used in case of aptamer-modified gold nanoparticles that cap the pores of MSN by binding of aptamer to adenosine on the pore exterior of MSN. The addition of ATP leads to competitive displacement of adenosine and disrupts the adenosine-aptamer interaction [139] (see Figure 3.4a). In another approach, phenylboronic acid on the surface of MSN binds reversibly to gluconic acid-modified insulin serving as caps on the mesopores. The introduction of saccharides leads to uncapping of the system and release of the guest molecules [134]. In a third approach, antibodies against sulfathiazole bind to hapten on surface of mesoporous silica support.

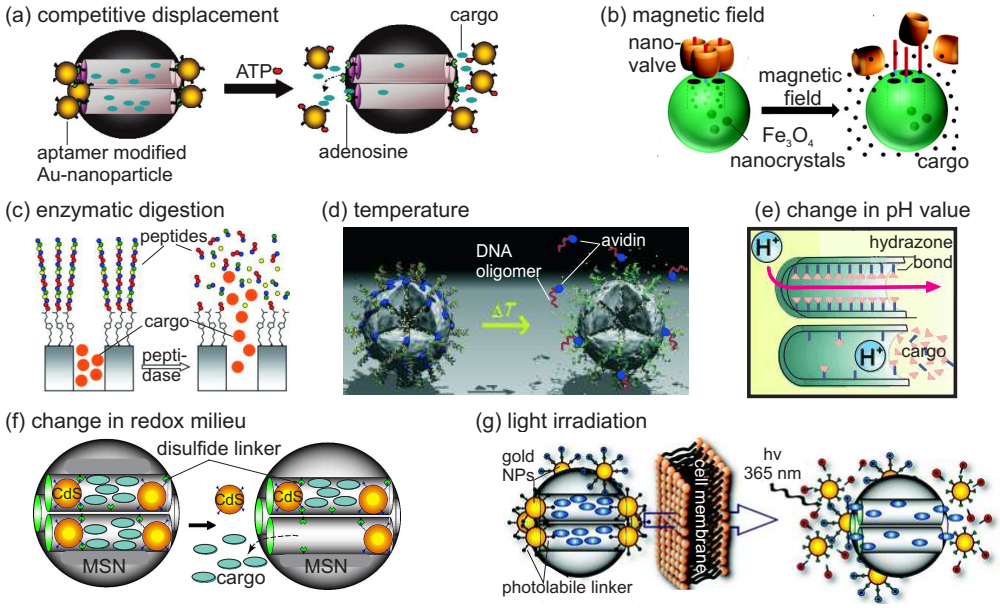

Figure 3.4: Stimuli for controlled drug release from MSN. (a) Competitive displacement (adapted from [139]).(b) Magnetic field (adapted from [169]). (c) enzymatic digestion (adapted from [147]). (d) temperature (adapted from [170]). (e) Change in pH value (adapted from [133]). (f) change in redox milieu (adapted from [129]). (g) light irradiation (adapted from [141]).

However, upon addition of sulfathiazole, the antibody is removed from its unspecific target [145].

Magnetic fields

Magnetic fields are used as release trigger as shown by Thomas *et al.* [169]. Zinc-doped iron oxide nanocrystals within a MSN were synthesized and the pores were sealed by a molecular machine consisting of cucurbit[6]uril, which electrostatically binds a molecular thread on the silica nanoparticle surface and prevents the cargo from leaching out of the MSN pores [135]. An alternating current magnetic field leads to the generation of local internal heat by the nanocrystals and causes the molecular machines to disassemble enabling drug release [169] (see Figure 3.4b).

Enzymatic digestion

Enzymatic digestion of the gatekeeping agent has been reported as another interesting approach for stimuli-responsive release. Stoddart *et al.* presented "snap-top" nanovalves on the surface of MSN, consisting of threads with α-cyclodextrin (α-CD) rings capped with ester-linked adamantyl stoppers. This construct is intact and prevents dyes from leaching out of the pores. Porcine liver esterase catalyses the hydrolysis of the adamantyl stoppers, leading to loss of the α-CD rings and

release of the cargo [156]. In another study a lactose derivative was used as a "gatekeeper" on the surface of mesoporous silica support. The enzyme β-D-galactosidase catalyzed the hydrolysis of the disaccharide lactose into the monosaccharides galactose and glucose followed by release of the loaded dye [149]. In a follow-up study, complex peptide sequences were anchored by click chemistry on the MSN. No release of the loaded dye was observed. Only after addition of proteolytic enzymes that cleaved the peptide sequences, dye release from MSN was observed [147] (see Figure 3.4c). Schlossbauer *et al.* presented an enzyme-responsive drug delivery system consisting of a biotinylated outer-particle surface. Upon addition of avidin, the well-studied biotin-avidin complex forms on the particle surface. As an enzymatic trigger trypsin enables the proteolytic digestion of avidin and re-opening of the pores. In addition, temperature can be used as a stimulus for denaturation of the avidin protein and pore opening [140]. One strategy with the ability to use both enzymes and temperature as external stimuli for pore opening has been adapted by Chen *et al.*. In their study, DNAse I is used to cleave DNA self-complementary double-strands clicked to pore openings on the surface of MSNs. In addition temperature induced denaturation of the DNA double strands can be applied [150].

Temperature

Temperature-induced DNA valve opening has been introduced before by Schlossbauer *et al.* [170]. For this, biotin-labeled DNA double strands were attached to the pore mouths of the core-shell CMS nanoparticles. The protein avidin closes the pores. The opening of the valve is achieved by temperature-induced separation of the DNA strands and removal of avidin from the pore openings (see Figure 3.4d).

pH

A change in pH is another option to induce controlled release from MSN. Porous silica particles with a naphtalene-containing dialkylammonium-tether are capped by noncovalent interactions with a crown-ether. Upon base addition, the crown-ether detaches from the tether and the cargo is released [152]. Another approach published by Zink *et al.* involves chemically fine-tuned trisammoniuim stalks tethered to the MSN orifices and encircled by cucurbit[6]uril (CB[6]) pseudorotaxanes. At neutral pH, the position of CB[6] on the stalk is such that the pores are sealed, however upon increase or decrease of the pH an opening of the pores is induced due to a change in position of CB[6] [135].
In a recent study, Muhammad *et al.* used ZnO quantum dot lids on MSNs which are efficiently dissolved in the acidic intracellular compartments of cancer cells. Using this system, the authors showed doxorubicine delivery to HeLa cells [171].
Another approach involves the use of a polymethacrylic acid-*co*-vinyl triethoxysilane (PMV) shell on mesoporous silica spheres that is in a loose and open state at pH 7.5 and in a compact and closed state at pH 4-5 [148]. Cauda *et al.* demonstrated, that selective functionalization of the pore

openings with both amino and sulfonate groups leads to ionic interactions of the two functional groups at acidic pH values and pore closure. It was shown that this gating system is applicable to base-induced release of the drug ibuprofen [125]. Apart from systems with a cap on the pore opening, pH-sensitive linkers, like hydrazone bonds were used to conjugate doxorubicin into the pores of MSN. The hydrazone bonds can be successfully cleaved at endosomal pH [133] (see Figure 3.4e).

Redox potential

Changes in the redox potential can also act as stimuli for controlled release. Most strategies utilize the reducing milieu of the cellular cytoplasm to cleave disulfide bridges. In one study, MSN end-capped with collagen was synthesized. Collagen is one component of the extracellular matrix of cells. The collagen immobilization on MSN was achieved by disulfide bonds which can be cleaved under reducing conditions [146]. Others used a disulfide-linked polymeric network as a "gatekeeper" on mesoporous silica particles. Poly(N-acryloxysuccinimide) was used for this purpose and the polymeric network was shown to be opened by reductive milieu [172]. Ambrogio *et al.* contributed to the field by introducing their redox-responsive "snap-top" nanovalves consisting -in this case- of threads with α-CD or CB[6] rings capped with disulfide-linked adamantyl stoppers. Upon addition of the strong reducing agent dithiothreitol (DTT) or 2-mercaptoethanol (ME), cargo release from the nanoparticles was observed [159]. Lin *et al.* succeeded to attach disulfide-bridged cadmium sulfide (CdS) nanoparticles to the voids of MSN to physically block premature cargo release, which was later induced by DTT [129] (see Figure 3.4f). Later an alternative strategy was proposed. For this, a membrane-impermeable cystein was linked into the pores of MSN by disulfide bridges. The study showed successful delivery of the cystein inside the cells. With this approach, the Lin group circumvented the problem of pore-capping [124]. A detailed study on disulfide-based drug delivery from CMS will be presented later in this thesis (see Chapter 8).

Light irradiation

Light irradiation can induce photochemically-controlled drug release. Various studies by the Zink group show that azobenzene derivatives can act as both gatekeepers and impellers in and on mesoporous silica nanoparticles. In detail, excitation with 457 nm light induces constant cis-trans isomerization reactions of N=N bonds in azobenzene and concomitant expulsion of the loaded cargo from MSN [131, 154]. In addition, the Zink group showed, that β-CD rings on azobenzene-containing stalks bind to trans-azobenzene units and seal the pores of MSN. After irradiation and isomerization from trans to cis- azobenzene the gates are opened and the cargo is released [157]. The establishment of a system applicable to living cells was the focus on the study by Vivero-Escoto *et al.* The authors capped MSN with gold nanoparticles via a photolabile linker which is positively charged in the MSN-bound state, but negatively charged in the MSN-unbound state. Light irradiation leads to a charge repulsion between the gold nanoparticles and MSN and uncapping of MSN [141] (see Figure

3.4g). In our research, we took advantage of photosensitizers used for photochemical internalization (PCI). These photosensitizers, once excited, can induce endosomal escape (presented in Chapter 8) and even rupture lipid bilayers surrounding CMS (see Chapter 9) inside living cells .
In summary, many strategies for controlled release have been presented. However, only some of the developed systems respond to physiologically relevant, easy-to-apply stimuli. Oftentimes the systems are not applicable in aqueous solutions, are not biocompatible or include toxic capping agents.

3.4 Biocompatibility of CMS nanoparticles

Not only the potential toxicity of capping agents are important to consider, the toxicity and biocompatibility of MSN material needs to be studied as well. Numerous groups published data on biocompatibility and MSN-induced cytotoxicity in cell culture [161, 173] and *in vivo* [174–176]. A long-term *in vivo* study of silica disk implants in living mice (1.5 g/kg body weight) showed no related changes in liver, kidney, uterus or lymph nodes. The implant was biocompatible with the surrounding tissue [116]. To study the toxicity of mesoporous silica nanoparticles and learn more about their biodistribution, it is, however, of great importance to consider the interplay of all key-parameters including size, surface properties and concentration, porosity of MSN as well as degradation byproducts and their effect on living organisms, tissues and cells.

3.4.1 Size, surface properties and concentration

The size of nanoparticles has an influence on biodistribution and might therefore also have an influence on toxicity. Generally, the size of nanoparticles for nanomedical applications should be designed to avoid immediate elimination by the immune system, which occurs more strongly in the larger size regime of 80-150 nm than at the lower size regime of 20-50 nm [177]. On the other hand, nanoparticles should be larger than 8 nm to avoid immediate renal clearance [178]. In the field of MSN, controversial findings have been reported about the effect of size on the cytotoxicity *in vitro*. Vallhov *et al.* reported, that -in case of MSN with diameters of 270 nm and 2.5 µm- the smaller particles showed lower activation of immune system and therefore lower cytotoxicity to human monocyte-derived dendritic cells (MDDCs) [179]. Another study by He *et al.*, however, showed the opposite effect. In case of the examined MSN with sizes of 190 nm, 420 nm and 1.22 µm, the authors found that the smaller particles show higher cytotoxicity on human breast cancer cells (MDA-MB-468) and African green monkey kidney cells (COS-7) [180]. Unfortunately none of the studies examined MSN in the range of 50-100 nm. However, it can be stated that MSNs in the size range of 100-170 nm show little cytotoxicity in various cell lines at concentrations lower than 100 µg/mL cell medium [181].
In addition to *in vitro* studies, *in vivo* studies have been performed. In an *in vivo* study, MSN with diameters of 80, 120, 200 and 360 nm have been injected into living mice at a dose of 20 mg/kg. The mice have been monitored for one month and survived well without pathological abnormalities [176]. In the same study, MSN were additionally shielded by a PEG coat. PEGylation increases

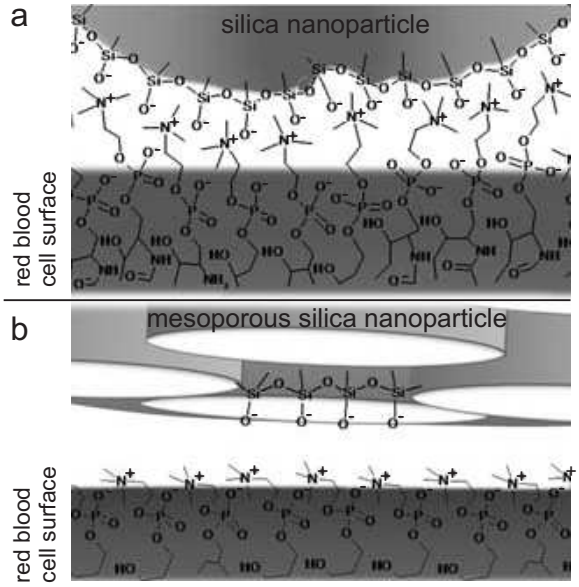

Figure 3.5: Hemolysis induced by non-porous and mesoporous silica nanoparticles. (a) Non-porous silica nanoparticles in contact with a red blood cell surface induces hemolysis. (b) Mesoporous silica nanoparticles induce hemolysis to lesser extent due to the reduced amount of silanol groups on the particle surface. Figure adapted from [186].

blood-circulation lifetime by avoiding phagocytosis. The PEG-shielded MSN showed the desired effects in the study be He *et al.* [176], but also in other studies [182, 183]. PEG linker with a molecular weight (MW) of 10 k showed the optimal chain density to reduce human serum protein (HSA) adsorbance and phagocytosis by human macrophages. In addition, PEGylation reduces hemolysis, the rupture of human red blood cells (HRBCs) and release of their contents into the surrounding fluid [182]. It was suggested, that hemolysis occurs due to the interaction of silanol groups of the nanoparticles with tetra-alkyl ammonium groups on the HRBC membrane. It is noteworthy that MSNs show a reduced hemolytic activity in comparison to silica nanoparticles without pores due to the voids on the surface of MSNs [184] (see Figure 3.5). Because of the hemolysis properties of surface silanol groups, it is advantageous to functionalize the silica surface for better biocompatibility. Positively charged quaternary ammonium groups, for example, were shown to be a quite biocompatible functionalization [185]. In addition, carboxy- and sulfonato-functionalized MSN were shown be less active in hemolysis than the unfunctionalized MSNs [186]. Along with particle size and surface properties, the applied nanoparticle concentration is a crucial parameter, when assessing toxicity. *In vitro* studies showed, that up to 100 µg/mL of MSN are well tolerated by cells as examined even after 7 cell cycles [161] or for up to 6 days [187]. *In vivo* studies showed no toxic effects on short-term for up to 200 mg/kg in mouse [175, 188], but administration of 1.2 g/kg MSNs is lethal to mice [189]. In the same study, different application routes were compared. Although subcutaneous administration was fairly well tolerated by rats (75 mg/kg), peritoneal and intravenous administration of 1.2 g/kg was lethal to mice within 24 hours [189].

3.4.2 Degradation

Biodegradability is a key issue regarding biocompatibility of MSN. An optimal nanoparticle drug carrier should be degraded and excreted by the body without accumulation. One study reported

on the structural stability and degradation behavior of mesoporous silica (MS) (particles in nano to micro range) in simulated body fluid (SBF). The authors describe a three-stage degradation behavior, including a very fast degradation step within 2 hours in which silica species are released from MS to a high degree. In the second step the amount of released silica species decreases due to the deposition of a calcium/magnesium silicate layer on the MS. The third stage shows very slow degradation heavily depressed by the calcium/magnesium silicate deposition layer with thorough degradation after 15-days [190]. A study on the degradation of unfunctionalized, phenyl-, chloropropyl- and aminopropyl-functionalized and poly(ethylene glycol)-coated CMS nanoparticles in SBF has been presented by Cauda *et al.* [191]. The authors show a fast degradation in all cases by broadening of pore-size distribution and loss of mesoporosity due to pore-size increase. CMS nanoparticles with a PEG-layer, however, showed a considerably decelerated degradation of the mesopore system in the particles and precipitation of inorganic compounds from SBF solution.
Although the degradation of silica has been studied and elucidated, it is important to learn about the influence of the degradation products on cells. In one study, it was shown that after 6 days of degradation an increase in hemolytic activity of MSN was detectable due to the altered surface structure in comparison to freshly synthesized MSN [184]. However, after 2 hours biodegradation in PBS, MSN side-products like silicic acids were exposed to human breast cancer cells (MDA-MB-468) and African green monkey kidney cells (COS-7). The outcome of the study was that no toxic effects have been detected on the cells [180]. Due to the amount of different parameters influencing toxicity of MSN on living matter, there has not yet been a study able to take all these parameters into consideration simultaneously. Therefore, more systematic research need to be performed *in vitro* and *in vivo* [99].
As shown in this chapter, an enormous amount of MSN designs and drug delivery strategies have been developed. It is important, however, to constantly evaluate the efficiency of the newly developed system on single cell level. To do so, fluorescence live-cell imaging is a powerful method as it allows detailed insights into the individual processes in living cells.

4 Fluorescence live-cell imaging

Fluorescence microscopy is based on recording of an emitted fluorescence signal in a microscope setup within nanoseconds after light absorption. It can be used to gain important insight into key questions in material science and biology, for example by exploring mesoporous silica structures [192–196] or by studying virus entry and egress [197–199]. To study virus infection, functions of biomolecules in cells, or general cell biological processes it is beneficial to perform fluorescence microscopy on a single-cell level, so called live-cell imaging [200].
In this thesis, highly-sensitive fluorescence live-cell imaging of the uptake and intracellular trafficking of CMS nanoparticles was performed. Our measurements enable direct observation of the dynamics of nanoparticles and the route which a nanoparticle takes into and inside a living cell. This leads to a detailed understanding of nanoparticle-cell interactions [201]. In addition, as we study CMS nanoparticles as drug carrier, the drug release mechanism in cells and the cellular fate after drug delivery can be studied in great detail. This knowledge can be a starting point for the development of new drug delivery systems or improvement of existing nanocarriers.
In this chapter, an introduction into the principles of fluorescence and fluorescent dyes will be given. Afterwards, loss of fluorescence by bleaching and quenching will be discussed theoretically. This is of interest, as in practice, we took advantage of quenching for studies on nanoparticle internalization kinetics and drug release. All our studies are made possible by high-end and custom-built fluorescence microscopes. Therefore, an introduction into our wide-field and spinning disk confocal microscope setups will be given. In a last part of this chapter, important developments increasing the meaning of live-cell imaging will be shown. The contributions of live-cell imaging adding information to standard ensemble measurements will be discussed.

4.1 Principles of fluorescence

Fluorescence is the emission of light by a molecule after absorption of a photon and energy transfer from the photon to the absorbing molecule. To gain an overview of the photophysical processes occurring in commonly used dyes, the Jablonski diagram conceived by Alexander Jablonski in the 1930s is adequate (see Figure 4.1).
When a fluorophore absorbs a photon, with sufficient energy generated by a laser or a lamp, it will be excited from the ground state S_0 to an electronic excited state S_n ($n \geq 1$). Oftentimes, the first electronic excited state S_1 is populated in some higher vibrational level [203]. From this state, the molecule can undergo vibrational relaxation to the lowest vibrational level of S_1. During vibrational relaxation the vibrational energy in the fluorophore is transferred to nearby molecules

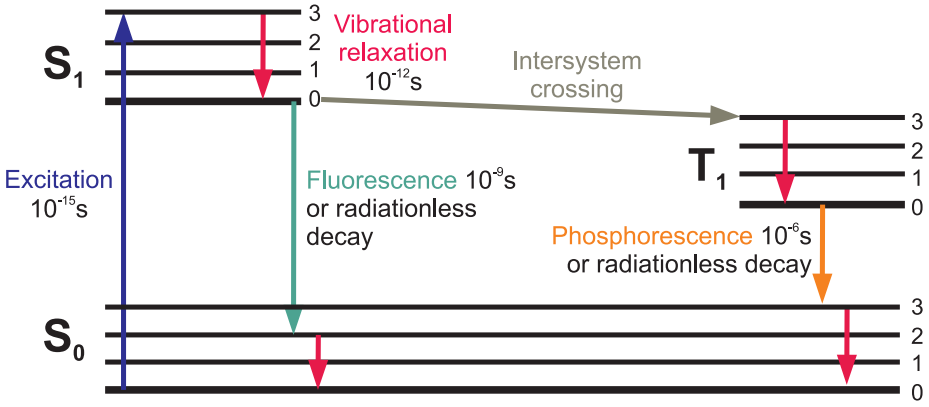

Figure 4.1: Jablonski diagram. Typical energy level scheme for fluorescence spectroscopy. Three electronic states are depicted: S_0: ground singlet state, S_1: first excited singlet state and T_1: lowest triplet state or other intermediate state. For each electronic states, vibrational energy levels (0, 1, 2, 3) are shown. Excitation, fluorescence, phosphorescence, radiationless decays and vibrational relaxation processes are indicated. Figure adapted from [202].

via direct interactions [202]. Vibrational relaxation occurs on a timescale of 10^{-12} s. From the lowest vibrational level of S_1, the electron is brought back to the ground state via fluorescence on a timescale of 10^{-9} s or radiationless decay. In addition, vibrational relaxation might take place to reach the lowest energy level of S_0. The loss of energy by radiationless processes both in the excited and in the ground state leads to an energy difference between excitation light and emitted light (Stokes shift). The subsequently emitted light is typically of higher wavelength than the absorbed light. This phenomenon renders fluorescence particularly powerful as the absorbed light can be separated from the emitted light with appropriate filters such that only fluorescent objects are detected [202]. As an alternative to fluorescence emission, there is a certain probability that molecules undergo spin conversion from the excited state to the first triplet state T_1. This process, called intersystem crossing, leads to electrons with parallel spins [202]. Some triplet-state molecules reach the ground state without light emission (radiationless decay), others emit light shifted to longer wavelengths relative to the fluorescence (phosphorescence). The latter process occurs on a timescale of 10^{-6} s or longer. As the electron needs to reverse its spin, the transition is unlikely and forbidden by quantum theory [202]. This leads to a slower decay than fluorescence.

To optimize the fluorescence signal, it is important to choose a fluorophore with suitable properties. A fluorophore contains an atom or group of atoms that behave as a unit in light absorption such as ketones, olefines, conjugated polyenes, conjugated enones and aromatic compounds [204]. Although many organic substances have intrinsic fluorescence, oftentimes samples are tagged with organic fluorescent dyes, nanocrystals ("quantum dots"), autofluorescent proteins, (fluorescently labeled) genetically encoded tags, and combinations of these probes [205].

When choosing an appropriate fluorophore its quantum yield and photostability play an important role. The fluorescence quantum yield (Q) is defined as the average ratio of emitted photons to the average number of photons absorbed. A high fluorescence quantum yield close to 100% is desirable

[206]. The quantum yield (Q) and fluorescence lifetime (τ_0) of a fluorophore are governed by the radiative decay rate (Γ) and the sum of the non-radiative decay rates (k_{nr}) connected to transitions from the excited state to the ground state [203].

$$Q = \Gamma \cdot \tau_0 = \frac{\Gamma}{\Gamma + k_{\mathrm{nr}}} \tag{4.1.1}$$

The fluorescence lifetime is defined as the average time the molecule stays in its excited state prior to returning to the ground state and is generally in the range of nanoseconds [203]. High quantum yields and short lifetimes are characteristic for fluorophores with high radiative rates [207]. Another important property of a fluorophore is its photostability. It should ideally be high, as almost all fluorophores are photobleached at some point upon continuous illumination [203].

4.2 Bleaching and quenching

The outcome of photobleaching is permanent fading of the fluorescent signal after a limited number of cycles between ground and excited states [202]. Photobleaching is dependent on the fluorophore structure and local chemical environment and is thought to be associated with photo-oxidation or other reactive degradation processes of the molecule.
Another effect that leads to a loss of fluorescence signal is called quenching. In contrast to photobleaching, this loss in fluorescence is reversible. Quenching is caused by noncovalent interactions between a fluorophore and its molecular milieu [202]. Two mechanisms are proposed: Collisional/dynamic quenching and static quenching. Collisional quenching occurs on the level of the excited fluorophore. Static quenching involves the ground-state fluorophore associating with another molecule. If the other fluorophore is identical, so-called self-quenching occurs [202]. However, although fluorescence quenching is a well-established technique, the mechanism of the quenching reaction is often not known with certainty [208].

4.3 Wide-field and spinning disk confocal microscopy

In this work, two microscopy techniques have been used: wide-field and spinning disk confocal microscopy. In wide-field microscopy a large area of interest is illuminated by a laser or an arc lamp and the fluorescence of this entire field of view is collected [209]. Laser illumination is beneficial as it provides high excitation intensities that are essential for strong photon emission by the fluorophores [201]. An epi-fluorescence microscope modified for wide-field laser illumination and equipped with two highly-sensitive EMCCD cameras was used. The wide-field setup is shown schematically in Figure 4.2a. For excitation of the sample, three lasers (405, 488 and 640 nm) are used. Their beams are aligned and guided into an acousto-optical tunable filter (AOTF) for adjusting the transmission intensities and combining the individual laser beams. Subsequently, the beam is coupled into an optical fiber, sent through a beam expander and focused on the back focal plane of the objective to achieve wide-field illumination. The laser beam exits the objective and excites the sample. Fluores-

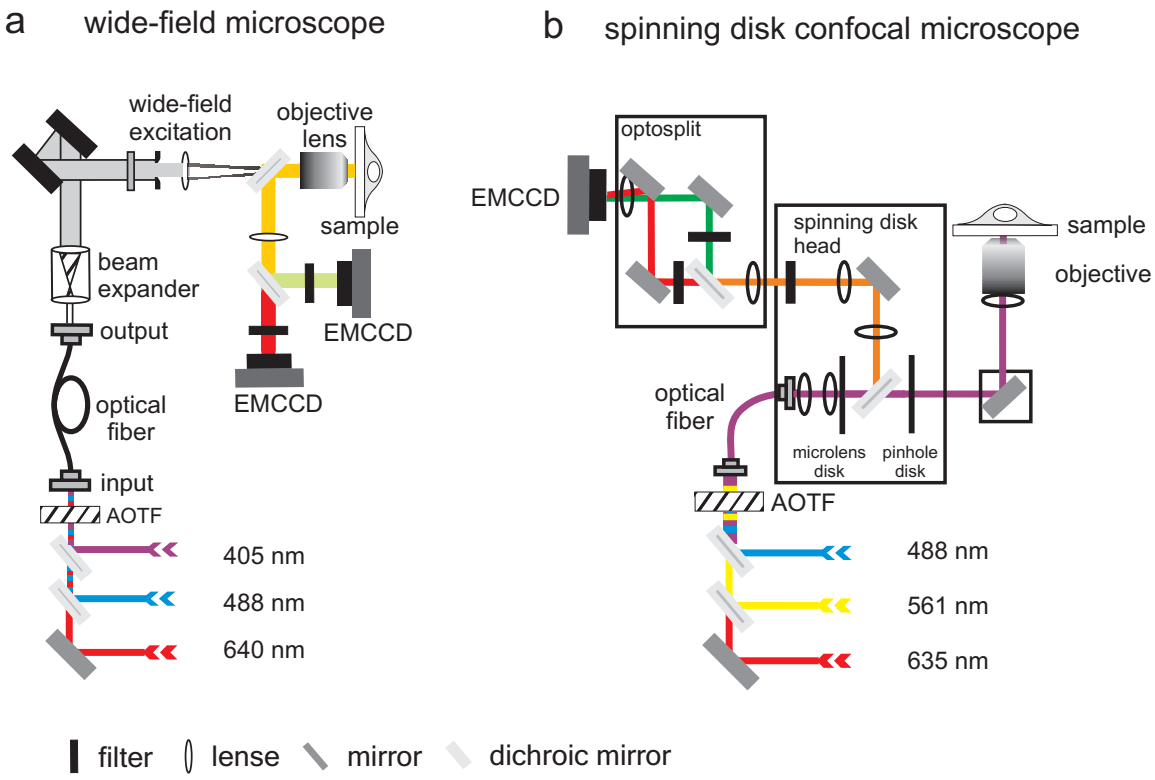

Figure 4.2: Wide-field and spinning disk confocal microscope setups. (a) In the wide-field setup, the lasers are focused onto the back focal plane of the objective for excitation of the sample. The fluorescence of the sample is collected by the objective and separated into two spectrally-separated channels. The fluorescence signal was projected onto two EMCCD cameras. The setup is based on the Nikon Eclipse Ti. (b) In the spinning disk setup, the laser light enters the spinning disc head and is further directed to the microscope to illuminate the sample. The emitted fluorescence passes the spinning disc head and is guided to the optosplit. The spectrally separated signal is imaged onto the two channels of the EMCCD camera. The setup is based on the Nikon 2000E. Adapted from figures provided by the courtesy of Dr. Sergey Ivanchenko and Dr. Yoshihiko Katayama.

cence light is collected from the sample by the objective in epifluorescence mode and separated from the excitation light by a dichroic mirror. The fluorescent light is further split by a dichroic mirror and two band-pass filters into two spectrally different channels that are imaged onto two separate EMCCD cameras.

The images or movies obtained with a wide-field system contain out-of-focus background signal and are two-dimensional. To extend the information from 2D (x- and y dimension) to 3D (z-dimension), the sample has to be scanned in the third dimension. This has been performed in this work by spinning disk confocal microscopy.

A spinning disk microscope is based on a so-called spinning disk unit where fast rotating discs contain concentrically arranged, multiple lenses and pinholes allowing for multiple scans simultaneously. By screening the many confocal spots over the sample an image is created. This allows to collect the image faster than scanning confocal microscopy and with multiple images per second. However, powerful lasers are required since the pinhole passes only a small amount of light [210]. The spinning disk microscope used for this work is commercially available from Andor technology and is depicted schematically in Figure 4.2b. The excitation path consists of three lasers (488, 561 and 635 nm with 50 mW) that can be selectively chosen in desired combinations by utilizing an AOTF. The lasers are coupled into a single-mode optical fiber and directed into the spinning disk unit. Afterwards, the beam passes the fast rotating microlense and pinhole disks, before entering the microscope and passing through the objective for illumination of the sample. The sample position is controlled in its x- and y-position by a motorized stage and in the z-position by a piezo-stage. In the fluorescence emission path, the fluorescence passes the pinhole disk for rejection of signal from outside the objective focal plane. Afterwards, emission light is spectrally separated from the excitation light by a quadruple dichroic mirror. A filter cube with an appropriate dichroic mirror and filters separates the emission light on two different parts onto the EMCCD camera.

Wide-field and spinning disk microscopy are highly sensitive fluorescence techniques and can be used for live-cell imaging to elucidate the details of nanoparticle–cell interactions on the single-cell level with high temporal and spatial resolution in real-time [201].

4.4 Living cancer cells in fluorescence microscopy

To non-invasively image a cell in all its dimensions, fluorescence microscopy is a powerful method [211]. For cell imaging, good excitation wavelengths are typically in the range of visible light. However, for *in vivo* imaging in an organism, the optimal excitation wavelength of a fluorophore is in the deep red or near-infrared range, because of the combined virtues of good tissue penetration due to a reduced tissue absorption in the range of 800 - 1200 nm [84], and low autofluorescence [212]. A breakthrough in the field of fluorescence live-cell imaging was the discovery and development of the green fluorescent protein (GFP and the related fluorescent proteins such as YFP and RFP) that led to the Nobel Prize in Chemistry for O. Shimomura, M. Chalfie and R.Y. Tsien in the year 2008. With fluorescent proteins, such as GFP, proteins of live cells can be permanently labeled with multiple colors. This is achieved by fusing the desired host cell gene to the genes of the

protein(s) of interest [213]. In a second step, the fusion construct is introduced into the cell, where the fusion protein is stably expressed. The ability to specifically and stably label desired cellular components enables dynamic insights into cellular processes that are not obtainable with fixed cells [214]. As one example, cancer research profited from tumor cells stably-expressing GFP and other fluorescent proteins *in vivo* by the possibility to examine tumor cell mobility, invasion, metastasis and angiogenesis [215]. In our work, we used HuH7 cells stably expressing GFP fluorescently-labeled cytoskeletal elements, such as actin and tubulin. The success of drug delivery was shown by incubation of cells containing GFP-labeled actin or tubulin with CMS loaded with drugs directed against actin or tubulin or their GFP-label. With this system, the outcome of drug delivery was assessed. Another set of experiments involved dynamics of fluorescently labeled nanoparticles with living cells. To examine the dynamics, we used single-particle measurements in living cells. Single-particle measurements can give insights into the position or movement of the fluorescent particles, the fluorescence intensity of the individual spots, as well as the color, the number, and distribution of the spots [216]. With all these information one can already draw conclusions on single-particle interactions with living cells. One advantage of single-particle imaging on the single-cell level is that distributions and fluctuations as well as "rare events" can be detected, which adds to the information available by ensemble measurements. Ensemble measurements (gene expression or flow cytometry) can investigate the final outcome, whereas high-resolution live-cell imaging provides detailed kinetic information on uptake and intracellular trafficking and spots bottlenecks in a chain of succeeding events [201].

5 Experimental methods and data analysis

5.1 Chemicals

The following chemical were used as received without further purification: 1,2-dioleoyl-sn-glycero-3-phosphocholine (DOPC), dioleoyl-phosphatidylethanolamine (DOPE), dioleoyl-sn-glycero-3-phosphocholine (DOPC), dioleoyl-trimethylammonium propane (DOTAP), didodecyldimethylammonium bromide (DDAB, all purchased from Avanti Polar Lipids), cetyltrimethylammonium bromide (CTAB, Fluka), Alexa Fluor 488 (AF488) and Alexa Fluor 488 Dextran (AFD, MW 10 kDa, both Invitrogen), cell culture media, fetal calf serum and B-27 serum-free supplement (Invitrogen), L-glutathione reduced (GSH, Sigma-Aldrich), meso-tetraphenylporphine ($TPPS_{2a}$, LumiTrans®, PCI Biotech), collagen A (Biochrom AG), 0.4% trypan blue solution and fluorescein sodium salt (Sigma). ATTO594 and Chromeo642-labeled chromobodies were provided by Dr. Ulrich Rothbauer (chromotek). Doubly distilled water from a Millipore system (Milli-Q Academic A10) was used.

5.2 Cell culture

HeLa cells were grown in Dulbecco's modified Eagle's medium (DMEM) with Glutamax I. Wild-type, actin-GFP and tubulin-GFP expressing HuH7 cells were grown in DMEM:F12 (1:1) at 37°C in 5% CO_2-humidified atmosphere. All media were supplemented with 10% fetal calf serum. To reduce autofluorescence in case of the HuH7 cells, the medium was changed to DMEM:F12 supplemented with 10% B-27 two days before seeding. The cells were plated on collagen A-coated LabTek-chambered cover glass (Nunc) 1-3 days before the measurement or incubation with the CMS nanoparticles in densities of 0.75×10^4 cells/cm^2 to 2×10^4 cells/cm^2. Prior to imaging, the medium was changed towards CO_2-independent medium (Invitrogen) and the cells were kept on a heated microscope stage at 37°C. There are two ways of nanoparticle incubation with cells. In case of short-term incubations ($t < 2$ h), the nanoparticles were pipetted into the CO_2-independent medium used for the measurements and the cells were incubated with the nanoparticles on the heated microscope stage. In case of long-term incubations ($t > 2$ h), the nanoparticles were added to the DMEM:F12 (1:1) medium (for HeLa cells) or DMEM:F12 supplemented with 10% B-27 (for HuH7 cells) and incubated at 37°C in 5% CO_2-humidified atmosphere prior to imaging.

5.3 Preparation of SLB@CMS

In a first step, the lipids have been prepared by Dr. Hanna Engelke from the group of Prof. Joachim Rädler. POPC, DOPC, DOPE, DOTAP and DDAB in various mixtures of given molar proportions were used. To obtain labeled SLBs, the amount of 2.5 mg of the lipids in chloroform was mixed with BODIPY-labeled HPC-lipids (0.5 µg), respectively. Chloroform was evaporated and the lipids were dried under vacuum overnight. Then the lipids were dissolved in a 1 mL mixture of 40%vol ethanol/60%vol water to yield a concentration of 2.5 mg/mL.
The lipids were then used for formation of the SLB. For this, the amount of 1 mg of CMS nanoparticles (25 mg/mL in EtOH) unlabeled or labeled with ATTO633 were centrifuged (19.000 rpm, 30 min) and 100 µL of unlabeled or labeled lipids (2.5 mg/mL in a mixture of 40%vol EtOH/60%vol water) were added. Upon addition of 700 µL of water, the formation of SLB on the external surface of CMS was induced. The SLB@CMS were then centrifuged again and redispersed in 800 µL of water, to eliminate unsupported lipids and the ethanol.

5.4 Fluorescence spectrometry

Spectrometry of trypan blue-based dye quenching

Emission spectra of the dyes AF488, ATTO488 and FITC were recorded in water with an excitation at 488 nm, emission spectra of Cy3 in water were recorded at 532 nm excitation on a FS900 fluorescence spectrometer (Edinburg Instruments). All spectra were recorded under exactly the same conditions with the same scan speed and step width (0.5 nm).

In-vitro release experiment from SLB@CMS.

The amount of 1 mg of unlabeled CMS nanoparticles (25 mg/mL in EtOH) was added to 10 mL of an aqueous solution of fluorescein sodium salt (1 µM, Sigma) and stirred (500 rpm) for 1 h at RT in the dark. In the case of colchicine, 1 mg of CMS nanoparticles labeled with ATTO633 was combined with 50 µL of an aqueous solution of colchicine (25 mM, Sigma) for 3 h under stirring at RT. After centrifugation, 100 µL of unlabeled lipids (2.5 mg/mL in a mixture of 40%vol EtOH/60%vol water) and 700 mL of water were added. The SLB@CMS were then centrifuged twice and redispersed in 800 µL of water, to eliminate the unsupported lipids and free dye molecules. Fluorescein-loaded CMS nanoparticles without lipids were prepared similarly as reference samples. An amount of 200 µL of the aqueous suspension containing SLB@CMS loaded with fluorescein or colchicine and loaded CMS nanoparticles without lipids, as reference samples, was transferred into a tube which could be closed by a holey cap lined with a dialysis membrane (with a molecular-weight cutoff of 16.000 g/mol). This custom-made system fits on the opening of a fluorescence cuvette, filled with 3 mL water. Whereas the SLB@CMS or CMS nanoparticles are too large to diffuse through the dialysis membrane, the dye molecules can enter the free cuvette volume and are detected by fluorescence spectroscopy. For the fluorescein delivery experiment, the excitation wavelength was

490 nm and the expected fluorescence emission maximum is 512 nm. Colchicine excited at 380 nm shows a maximum of emission at 437 nm. The dye-loaded SLB@CMS was monitored up to 60 min. After the addition of 20 µL of absolute EtOH or Triton X-100 (Sigma) into the tube containing the SLB@CMS sample, the lysis of the lipids from the CMS nanoparticles allows the diffusion of the dye molecules out of the mesopores and their detection in the cuvette.

5.5 Microscopy *in vitro* and in live cells

Trypan blue-based nanoparticle quenching

In case of the control measurements, Cy3-labeled CMS-PEG550 and 5000 MW nanoparticles were sedimented on LabTek-chambered cover glass (Nunc) and exposed to 0.04 g/L trypan blue (Sigma) in CO_2-independent cell culture medium (Invitrogen). For the quenching measurements in live cells, Cy3-labeled CMS-PEG550 nanoparticles were added to HeLa cells growing on collage A-coated LabTek-chambered cover glass (Nunc). After 10-80 min of nanoparticle incubation, the cells were exposed to 0.04 g/L trypan blue. In both cases, the fluorescence intensity was recorded before and after trypan blue addition on a fluorescence wide-field microscope. The amount of particles before and after quenching was determined by a Labview-based application "Count Co-localization" by Volodymyr Kudryavtsev (group of Prof. Christoph Bräuchle, Prof. Jens Michaelis and Prof. Don Lamb, all LMU). First, a threshold for the fluorescence intensity of a single particle was determined by multiple measurements of the particles on cover glass. Is the fluorescence of a particle above the threshold, it is counted by the program. The particles showing a fluorescence lower than the threshold are determined as quenched and not counted. Comparison of the amount of nanoparticles counted before and after quenching gives the percentage of internalization into the cells.

Dye release at single-particle level on glass.

Redox-cleavable CMS-CysATTO633$_{\text{core}}$ and the non-cleavable control CMS-ATTO633$_{\text{core}}$ were measured on glass on a wide-field fluorescence microscope first in water, then in 10 mM GSH solution. Movies of the ATTO633 and background fluorescence were recorded before ($t < 0$ min) and after ($t > 0$ min) addition of the GSH solution. As a control measurement, redox-cleavable CMS-CysATTO633$_{\text{core}}$ nanoparticles were measured on glass in 0.025 µg/mL $TPPS_{2a}$ solution. The fluorescence intensity of the particles was measured before and after activation with laser light of 405 nm.

Photochemical endosomal release of CMS nanoparticles by $TPPS_{2a}$.

The photochemical release experiments were performed on the basis of the experiments by de Bruin *et al.* [30]. In brief, the cells were seeded at a density of 0.75×10^4 cells/cm^2, 3-4 days before imaging. 12-24 hours before imaging, the medium was replaced by a medium containing 0.025 µg/mL $TPPS_{2a}$. AFD in a concentration of 0.24 mg/ml and the nanoparticles were added to the cells. Cells were incubated overnight, washed three times with CO_2-independent medium and subsequently

transferred to a 37°C heated microscope stage. The photosensitizer was activated by illumination with 405 nm laser light for 1 min. After the activation of the photosensitizer, the measurement was performed with alternating excitation by 488 and 642 nm laser light.

Photochemical drug delivery from CMS nanoparticles by covalently surface-bound PpIX.

The cells were seeded at a density of 0.75×10^4 cells/cm^2, 3-4 days before imaging. 12-24 hours before imaging, PpIX-CMS nanoparticles were added to the cells in culture together with AFD in a concentration of 0.24 mg/ml. Cells were incubated overnight, washed three times with CO_2-independent medium (Invitrogen) and subsequently transferred to a 37°C heated microscope stage. The photosensitizer was activated by illumination with 405 nm laser light for 1 min. After the activation of the photosensitizer, the measurement was performed with alternating excitation by 488 and 642 nm laser light.

Wide-field fluorescence microscopy for live-cell imaging.

Wide-field fluorescence microscopy was performed on a custom-built setup based on the Nikon Ti microscope equipped with a 1.45 N.A. 60x Apo TIRF oil immersion objective (Nikon). The photosensitizer was excited by 405 nm laser light (~0.15 W/cm^2) 15 s-1 min prior to imaging. AFD and ATTO594/ATTO633 were excited by 488 and 561 or 642 nm laser light in alternating fashion. Fluorescence was collected in epifluorescence mode, split into two emission channels by a dichroic mirror (565 DCXR, Chroma) and passed through adequate filter sets (525/50, 617/73 or 725/150, Semrock). The green and red emission channels were projected onto two EMCCD cameras (iXon+, Andor Technology) with a pixel format of 512x512. The presented overlays of the the two camera channels were made afterwards.

Spinning disk confocal microscopy for live-cell imaging

Confocal microscopy for live-cell imaging was performed on a spinning disk confocal microscope purchased from Andor (Revolution System). The setup is based on the Nikon TE2000E and utilizes a Yokogawa spinning disk unit (CSU10). The system was equipped with a 1.49 NA 100x Plan Apo oil immersion or a 1.3 NA 40x Plan Fluor oil immersion objective from Nikon. Samples were illuminated with 488 nm, 561 nm and 640 nm lasers exciting GFP, BODIPY, ATTO488, PI and Alexa Fluor 647 or Chromeo642 and ATTO633 respectively. For two-color detection of ATTO488 and ATTO633, dichroic mirrors and band-pass filters HQ 525/50 and 730/140 were used (AHF analysentechnik AG). The same settings were used for two-color detection of GFP and Alexa Fluor 647 or Chromeo642, as well as for two-color detection of GFP or BODIPY and ATTO633. For the detection of PI a 585 nm dichroic mirror and 630 /69 nm filter was employed. Image sequences were captured on two different sections of an electron multiplying charge coupled device camera (iXon+, Andor Technology) with a pixel format of 512x512. The presented overlays of the different sections

and z-planes were made afterwards.

5.6 Fluorescence intensity evaluation of the CMS-loaded drug and fluid phase marker.

The fluorescence intensity of nanoparticles was obtained by calculating the mean fluorescence intensity of regions of interest (ROI) containing a single endosome or nanoparticle for all frames of a movie. To account for different laser excitation intensities and differing fluorescence intensities of individual movies, the mean fluorescence intensity was normalized to the initial background intensity defined by a ROI in a region without particles and plotted over time.
In some cases, as stated in the text, a rolling ball background filter of 5 pix was used to remove inhomogeneous background fluorescence due to released AFD and loaded drugs in both channels [217]. Afterwards, the mean fluorescence intensity was normalized to the highest intensity value and plotted versus time.

6 Internalization of CMS nanoparticles

Nanoparticles for intracellular drug delivery have to cross several barriers in a human body before they deliver their drug cargo to the site of action. One important site of action for drug delivery is the cellular cytoplasm. In cytoplasmic drug delivery, the first major barrier for the nanoparticle on the cellular level is the plasma membrane of the target cell. Therefore, processes occurring during the initial contact of the nanoparticle with the plasma membrane that result in the intracellular presence of the nanoparticle are of great importance. One way to study the cellular entry is to explore the internalization time scale of nanoparticles. The nanoparticles used for this study are CMS nanoparticles with a polyethylene glycol (PEG)-shell. PEG coatings are particularly important for intravenously administered drug carriers due to their shielding capability, leading to reduced plasma protein adsorption and reduced phagocytosis by cells of the reticulo endothelial system (RES) [23, 218]. Thus, the PEG shell increases the nanoparticle's lifetime in blood circulation and avoids capturing of the nanoparticles before reaching the target cell [11]. However, despite the advantages, PEGylation reduces cellular uptake and slows down the internalization dynamics [1, 218]. To increase the specificity of cellular binding and to speed up internalization, targeting moieties can be attached to the surface of the nanoparticles. The so-called "targeting" leads to specific receptor-ligand interactions of nanoparticles with the cell and overcomes the problem of low and unspecific interactions of PEG-shielded nanoparticles [218].
In this chapter, we examine the internalization time scale of PEG-shielded CMS nanoparticles into living HeLa cells by a quenching assay. The assay exploits the fact that a cell membrane-impermeable quencher dye only quenches extracellular particle fluorescence, whereas the intracellular particles remain visible. Comparing the amount of fluorescent spots visible before and after quencher addition, the percentage of internalized nanoparticles can be evaluated. However, before the quenching assay could be performed, the experimental conditions had to be optimized. In a first step, we tested different dyes for their ability to be quenched by trypan blue, a well-known membrane-impermeable quencher dye. In a second step, PEGylated CMS nanoparticles containing PEG chains of different molecular weights have been evaluated as quenchable nanoparticles. Finally, after the measurement conditions were set, the quenching assay was performed on a single-cell level. In the last part of this chapter, first attempts for CMS targeting to cancer cells will be presented as an outlook to future work.

6.1 Choice of a quenchable dye

For the quenching assay on living cells, a dye is needed that is quenched well by the cell membrane-impermeable quencher dye trypan blue. To find a dye suitable for this experiment, we recorded

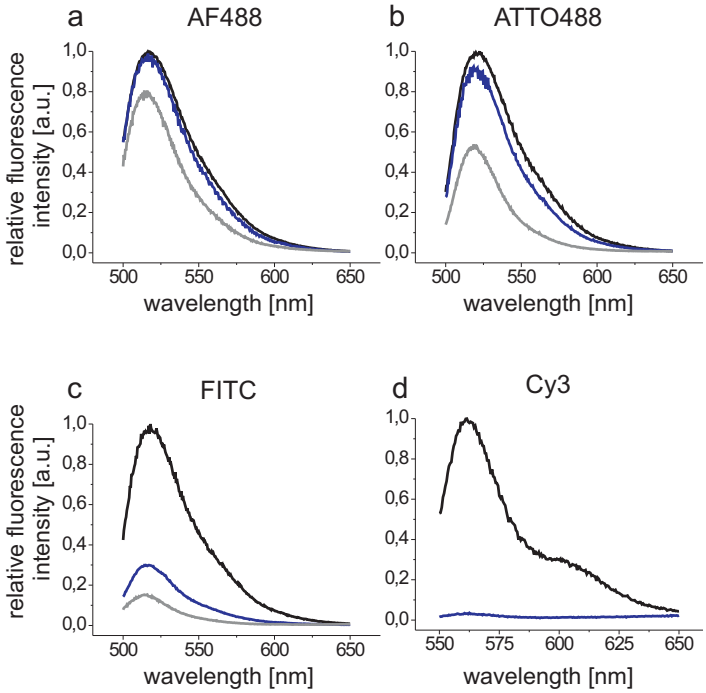

Figure 6.1: Fluorescence spectra of fluorophores quenched by trypan blue. Fluorescence spectra of four dyes in aqueous solution were taken upon addition of trypan blue in different concentrations (black curves: spectra without trypan blue, blue curves: 0.01 g/L trypan blue and gray curves: 0.06 g/L trypan blue.) (a) AF488 is not well quenched by trypan blue in the applied concentration range. (b) ATTO488 is slightly quenched by trypan blue. (c) FITC shows a more pronounced ability to be quenched by trypan blue. (d) Cy3 is quenched well already at a trypan blue concentration of 0.01 g/L.

emission spectra of Alexa Fluor 488 (AF488), ATTO488, fluorescein isothiocyanate (FITC) and Cy3 in the absence and presence of trypan blue by fluorescence spectrometry. All dyes, except for ATTO488, have been reported to be quenched by trypan blue in cellular uptake studies [1, 219, 220]. However, the concentration of trypan blue varied considerably between the different studies. From previous studies in our lab, we know that the trypan blue concentration should be around 0.04 g/L [1, 2]. Higher concentrations result in a high fluorescence background signal due to the fluorescence of trypan blue itself. Therefore, we wanted to investigate the ability of the aforementioned dyes to be quenched by trypan blue in concentrations of 0.01 g/L and 0.06 g/L. For the measurement, the dyes were diluted in water and added to a 200 µL cuvette. Emission spectra of AF488, ATTO488 and FITC were recorded at an excitation of 488 nm on a fluorescence spectrometer. In case of Cy3 an excitation wavelength of 532 nm was used. The emission intensities were normalized and are presented in Figure 6.1.

Depending on the dye, the quenching effect is found more or less pronounced. Starting from their initial fluorescence intensity curves without trypan blue (depicted in black in Figure 6.1a and b), AF488 and ATTO488 show almost no reduction in their fluorescence intensity upon addition of 0.01 g/L trypan blue (blue curves in Figure 6.1a and b). Further addition of trypan blue up to a

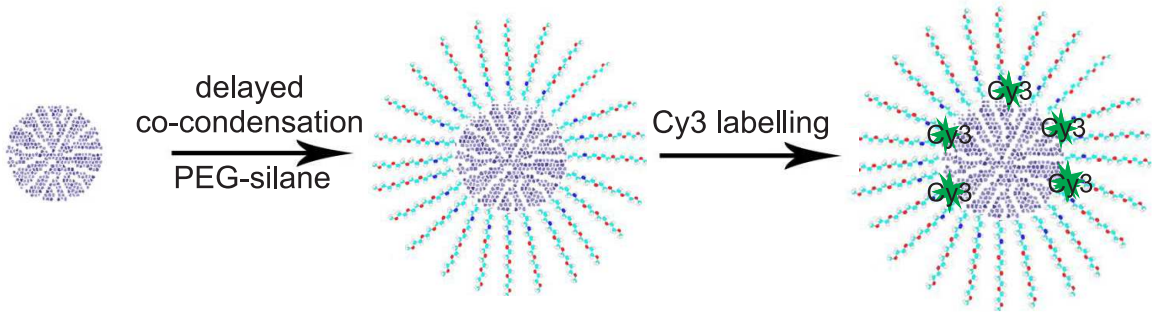

Figure 6.2: Synthesis scheme of CMS-PEG nanoparticles. A triethoxy-silane terminated PEG-precursor is used for co-condensation with the silica precursor. This approach is used to bind the PEG precursor covalently to the outer surface of the growing CMS nanoparticles. In a last step, the CMS surface is labeled with the fluorescent dye Cy3. Adapted from a figure provided by the courtesy of Christian Argyo.

concentration of 0.06 g/L decreased the fluorescence intensity slightly in case of AF488 (gray curve in Figure 6.1a) or more pronounced in case of ATTO488 (gray curve in Figure 6.1b). However, a significant reduction can be observed in case of FITC (Figure 6.1c) and Cy5 (Figure 6.1d), with complete quenching at a trypan blue concentration of 0.01 g/L. For this reason, Cy5 was selected to be bound to the nanoparticle surface and is used for the following studies.

6.2 Choice of quenchable CMS nanoparticles with PEG-shell

To design nanoparticles for quenching experiments, CMS with surface-bound Cy3 and PEG shells have been synthesized by Christian Argyo from the group of Prof. Thomas Bein. PEGylation is beneficial as the nanoparticles show enhanced colloidal stability in aqueous suspensions when PEG polymer is grafted on the nanoparticle's surface [221]. Well-dispersed, unaggregated nanoparticles are in turn a prerequisite for a successful evaluation of the quenching assay.

A schematic representation of the synthesis is depicted in Figure 6.2. As a first step, a linear PEG-silane precursor is synthesized and added to the CMS synthesis mixture for outer shell functionalization with linear PEG-silanes using a delayed co-condensation approach [9]. Finally, the silica surface is labeled with Cy3 by reacting the dye's NHS ester group with the residual aminopropyl functionality derived from the co-condensation approach with unpurified PEG-aminopropyl silane precursor (see Figure 6.2). Unreacted dye is washed away with ethanol and the nanoparticles are dispersed in water (for details see [222]). Two particle types were synthesized: CMS with PEG550 and 5000 MW. The particle types have been tested for their ability to be quenched by trypan blue.

To test the ability of the Cy3-labeled CMS nanoparticles with PEG550 and 5000 MW shells to be quenched by trypan blue, the nanoparticles in aqueous suspension have been sedimented on glass coverslips. The fluorescence of the Cy3-labeled nanoparticles was recorded in a movie sequence before and after addition of 0.04 g/L trypan blue. The fluorescence intensities of four representative

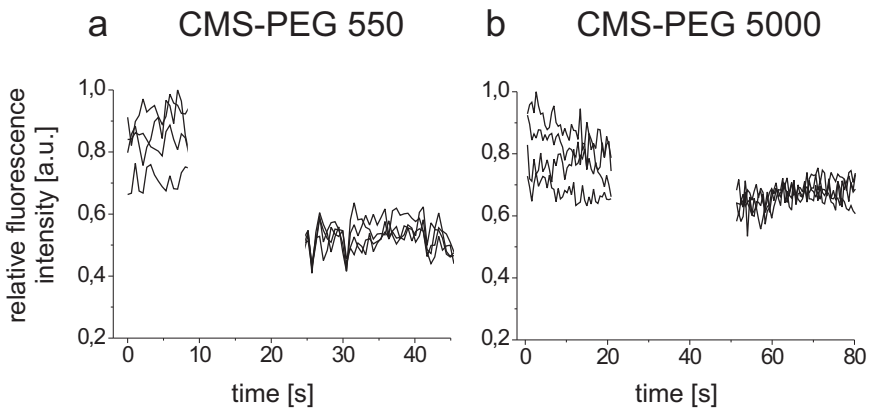

Figure 6.3: Quenching of CMS-PEG nanoparticles. Fluorescence intensity plots of four representative nanoparticles on cover glass. (a) Cy3-labeled CMS with PEG 550 MW before ($t = 0 - 10$ s) and after trypan blue addition ($t = 25 - 45$ s). (b) Cy3-labeled CMS with PEG 5000 MW before ($t = 0 - 20$ s) and after trypan blue addition ($t = 45 - 80$ s). A PEG layer composed of 550 MW PEG was found to be more permeable for trypan blue than one composed of 5000 MW PEG.

nanoparticles were extracted, normalized and plotted versus time (see Figure 6.3). In the evaluation, nanoparticles are counted as successfully quenched if two prerequisites apply. First, all nanoparticles on cover glass have to decrease in their fluorescence intensity. Second, it is possible to set a clear threshold between the fluorescence intensity of unquenched and quenched nanoparticles. CMS-PEG550 nanoparticles show a decrease of their fluorescence intensity after trypan blue addition (see Figure 6.3a). A clear threshold can be set between the fluorescence intensity of the nanoparticles before and after quenching. This result indicates that the PEG550 shell enables trypan blue to reach the Cy3 dyes on the CMS nanoparticle surface. CMS-PEG5000 nanoparticles, however, show a slight reduction in fluorescence intensity that is not sufficiently high to set a threshold between the fluorescence intensity before and after trypan blue addition (see Figure 6.3b). Therefore, CMS-PEG550 nanoparticles were chosen for subsequent uptake studies on HeLa cells.

6.3 Uptake percentage of CMS-PEG550 into HeLa cells

To determine the timescale of internalization of Cy3-labeled CMS-PEG550 nanoparticles into HeLa cells, quenching experiments were performed with trypan blue. Addition of trypan blue to the cells leads to quenching and disappearance of the Cy3-fluorescence of extracellular nanoparticles, the fluorescence of intracellular particles remains intact. Before and after application of trypan blue, the Cy3-CMS-PEG550 fluorescence was recorded in an image sequence on a wide-field microscope. From the movie, the amount of fluorescent spots before and after trypan blue addition is compared and the percentage of internalized nanoparticles can be determined (for a detailed description, see [30]). For the experiment, the nanoparticles have been incubated with HeLa cells for 10-80 min. Quencher dye addition occurred at different time points within this time range.

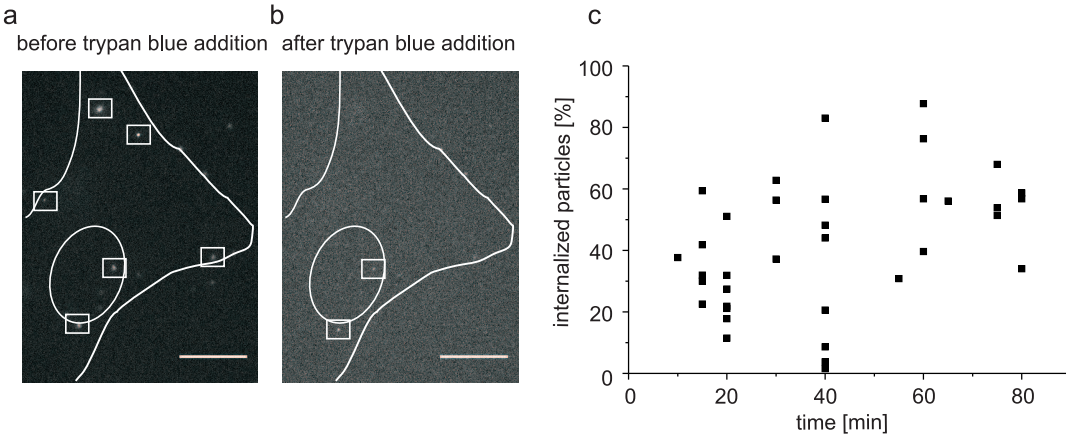

Figure 6.4: Quenching experiments on HeLa cells to determine the percentage of internalized CMS-PEG550 nanoparticles at different timepoints. (a) Fluorescence wide-field image of CMS-PEG550 nanoparticles (highlighted by white boxes) incubated for 55 min with a HeLa cell before addition of trypan blue. (b) Fluorescence image of the cell after addition of trypan blue. Two particles are still visible after trypan blue addition. The nucleus and the cell boundaries are outlined in white. Scale bar: 5 µm. (c) Internalization kinetics of CMS nanoparticles into cells measured by particle quenching. The plot displays the percentage of internalized nanoparticles determined at different time points after addition of the nanoparticles to the cells. Each data point in the graph represents one single-cell measurement.

Figure 6.4a and b show the fluorescence images of Cy3-labeled CMS-PEG550 nanoparticles incubated with a HeLa cell for 55 min. Before trypan blue addition, six nanoparticles are counted in the cellular region (white boxes), as determined by transmitted light image and indicated by white lines (see Figure 6.4a). After trypan blue addition two nanoparticles were counted (see Figure 6.4b). As a result, 33% of the nanoparticles have been internalized into the cell after 55 min. 77% were still quenchable and therefore present in the cell exterior. The data obtained by quenching of 38 different HeLa cells is plotted in Figure 6.4c. The percentages of internalized CMS-PEG550 nanoparticles after different incubation time intervals are shown. Since quenching was irreversible, each data point in the graph represents one single-cell measurement. The nanoparticles exhibit a large spread in the internalization time. After 20 min 22% (median value) of the particles were internalized by HeLa cells. This percentage increases with time to 67% after 60 min. The internalization percentages are in the same range as obtained for PEI polyplexes and magnetic lipoplexes in HuH7 liver cancer cells [1, 2]. This is not surprising, as all three particle types lack a receptor ligand as targeting moiety. Therefore, non-specific uptake and thus a similar internalization time scale may be expected. Particles with specific receptor targeting unit, such as EGF-targeted polyplexes, show a much faster internalization behavior with 50% (median) internalization after 5 min and 91% (median) internalization after 10 min [1]. It can be noted that epidermal growth factor receptor (EGFR) targeting leads to fast and efficient internalization.

6.4 Targeting of CMS nanoparticles with receptor-ligands

Current efforts to improve the internalization of CMS nanoparticles focus on ligands for cancer cell targeting. In first preliminary studies, Dr. Axel Schlossbauer, Dr. Valentina Cauda and Christian Argyo, from the group of Prof. Thomas Bein, equipped CMS nanoparticles with receptor ligands for fast intracellular uptake and, above all, for cancer specific targeting. One targeting ligand is the epidermal growth factor (EGF), a globular protein of 6.2 kDa consisting of 53 amino acids, that binds specifically and with high affinity [223] to the epidermal growth factor receptor (EGFR, Her1, ErbB1). The receptor plays a role in the control of proliferation, differentiation, and cell survival and is overexpressed on multiple solid tumors [224]. In first experiments, EGF was bound directly to the CMS surface without a PEG spacer. However, this leads to aggregation of the EGF-equipped nanoparticles. The particles were not applicable for uptake and single-particle tracking studies. Ongoing research by Christian Argyo (group of Prof. Thomas Bein) and Veronika Weiß (group of Prof. Christoph Bräuchle) focuses on EGF-receptor targeting by EGF-equipped CMS nanoparticles. The CMS particles are coated by a lipid bilayer and EGF is attached to a DSPE-PEG linker incorporated in the lipid bilayer.

6.5 Summary

In this chapter, a quenching assay was prepared and performed to assess the internalization time scale of PEG-shielded CMS nanoparticles into living HeLa cells. As a first step for the preparation of the quenching assay, we evaluated the ability of dyes to be quenched by trypan blue. The emission spectra of AF488, ATTO488, FITC and Cy3 before and after addition of trypan blue revealed that Cy3 is a well-suited dye for our purposes. As a second step, Cy3-labeled CMS nanoparticles containing PEG shells of 550 and 5000 MW have been tested for their ability to be quenched by trypan blue by fluorescence microscopy. CMS-PEG550 nanoparticles showed a reduction of the fluorescence intensity after quenching. An intensity threshold to distinguish between the unquenched and the quenched state was set. Therefore, CMS-PEG550 fulfilled the criteria for the quenching assay. To perform the quenching assay and determine the internalization time scale of CMS into living HeLa cells, Cy3-labeled CMS-PEG550 nanoparticles were used. As expected, a large spread of the internalization times was observed. After 20 min 22% (median value) of the particles were internalized into the cells. The percentage increased with time up to 67% after 60 min. The time scale is similar to other nanoparticles exhibiting non-specific uptake. To speed up the internalization, first preliminary experiments have been performed with EGF-equipped CMS nanoparticles. Future research will focus on this important subject.
In summary, the internalization time scale of PEG-shielded CMS nanoparticles resembles other unspecifically internalized nanoparticles. With this in mind, we focused on further parameters that are important for successful drug delivery, such as drug loading, pore sealing and intracellular controlled release.

7 Lipid bilayer-coated CMS nanoparticles

For the delivery of therapeutic substances to diseased cells by mesoporous silica nanoparticles, drug loading and intact sealing of the pores is essential to prevent degradation or premature drug release. A variety of strategies for pore sealing have been reported, including large molecules, clusters or molecular assemblies [129, 140, 156, 225] (see Chaper 3.3.2). An alternative design involves supported lipid bilayers (SLB) that cover the entire surface of the particles [143, 144, 226]. Lipid bilayers, as main components of cellular membranes, have been studied especially in form of liposomes as drug and gene delivery vehicles. Liposomes are advantageous systems, due to the amphiphilic nature and good biocompatibility profile [23]. However, besides their advantages, liposomes have the disadvantage of low structural stability [143]. Therefore, we applied lipid bilayers on CMS nanoparticles as solid support and stabilized the bilayer while efficiently closing the pores. In the first part of this chapter, SLB-coated CMS will be studied as drug carrier for the anti-cancer drug colchicine. The particles have been synthesized, loaded with the drug and sealed by the lipid bilayer. Bulk delivery kinetics of a dye from SLB@CMS have been measured by fluorescence spectrometry. Spinning disk confocal live-cell imaging of colchicine-loaded SLB@CMS has been performed to gain insight into the drug delivery mechanism in living cancer cells (Chapter 7.1). This chapter is taken in parts from our publication in Nano Letters [12].

In the second part of this chapter, the mode of cellular uptake of lipid bilayer-coated CMS will be studied depending on the composition of the lipid bilayer. The composition of the lipid bilayer plays an important role for interaction of the system with other membranes [227] and therefore also for cellular uptake. The predominant mode of uptake of CMS nanoparticles into cells is endocytosis. However, besides endocytosis, fusion with the plasma membrane could be of interest. Possible advantages of fusion include that endo/lysosomal entrapment is avoided and that the lipid bilayer-seal covering the nanoparticle remains in the plasma membrane while the particle enters the cytosol. Some enveloped viruses, for example, optimized their lipid bilayer composition such that fusion of the bilayer with the plasma membrane is one pathway for cellular entry. Therefore, we synthesized lipid bilayers of various compositions, incubated them with HuH7 cells and examined by live-cell imaging and co-localization analysis, whether a separation of SLB from CMS due to fusion is observed after internalization (Chapter 7.2).

7.1 Colchicine delivery by lipid bilayer-coated CMS

To coat CMS by lipid bilayers, different strategies have been pursued. In first studies by Prof. Brinker and co-workers lipid coating was achieved by fusion of positively charged liposomes with

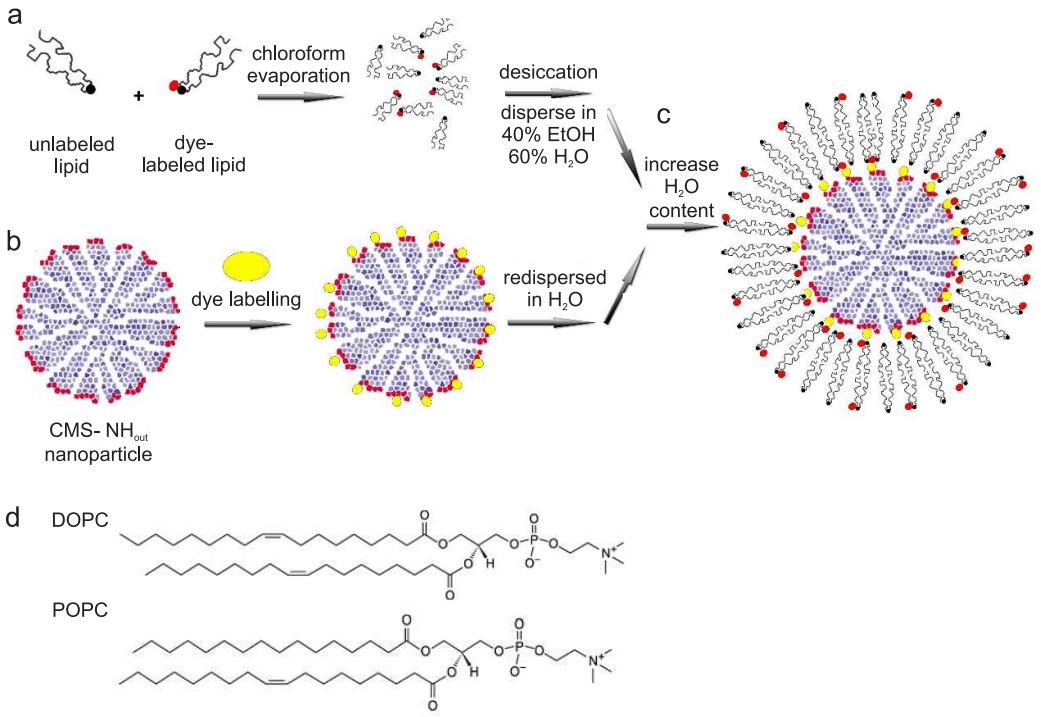

Figure 7.1: Scheme of the synthetic procedure for the formation of SLB on CMS nanoparticles. (a) The lipids in chloroform were mixed with dye-labeled lipids. After chloroform evaporation, the mixture of unlabeled and labeled lipids was desiccated and redispersed in a mixture of 40%vol EtOH/60%vol water. (b) After the synthesis of outer surface amino-functionalized CMS, the amino-propyl groups were labeled with a fluorescent dye. The labeled particles were then centrifuged. (c) The lipid solution was added to the centrifuged dye-labeled CMS nanoparticles. Upon addition of water, the SLB was formed on the surface of the CMS nanoparticles. (d) The two kinds of lipids used are DOPC and POPC.

negatively charged mesoporous silica nanoparticles [143]. The composition of the nanoparticle-supported liposomes was further modified by lipid exchange with free liposomes. The synthesis yielded 100 nm lipid-coated mesoporous nanoparticles retaining 75% of a loaded dye. In addition, doxorubicine delivery to living CHO cells was shown [144]. However, there is a lack of detailed studies on the drug delivery properties of these particles on a single-cell level.

In our study, a solvent-exchange method was used to obtain single CMS nanoparticles coated with an intact SLB. In addition, we studied in detail the drug delivery properties of this particles by live-cell imaging. The data presented in this chapter have been published in Nano Letters [12]. The supported lipid bilayer-coated CMS nanoparticles (SLB@CMS) were developed in a close collaboration with Dr. Valentina Cauda of the group of Prof. Thomas Bein and Dr. Hanna Engelke and Dr. Delphine Arcizet of the group of Prof. Joachim Rädler (both LMU Munich).

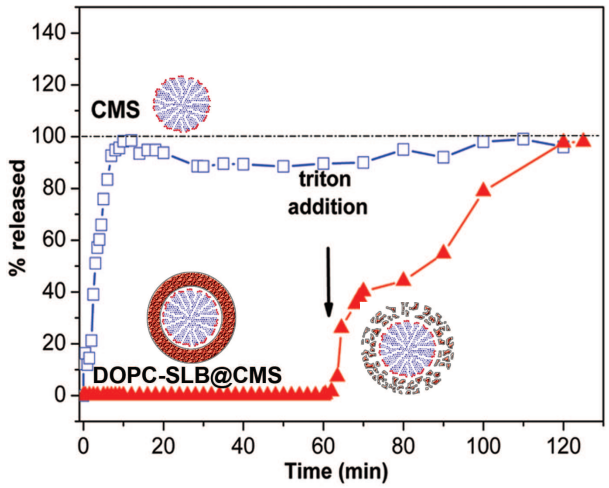

Figure 7.2: Fluorescence spectrometry of fluorescein delivery kinetics from SLB@CMS. Fluorescein-loaded CMS nanoparticles without SLB release fluorescein within 10 min into the surrounding medium (see blue curve). Fluorescein loaded SLB@CMS do not show fluorescein release into the surrounding medium within 60 min. However, after lysis of the lipid bilayer upon triton addition, prompt release of fluorescein was observed (red curve).

7.1.1 Synthesis and characterization of SLB@CMS

To study the mode of action of single colloidal mesoporous silica nanoparticles coated with an intact supported lipid bilayer (SLB@CMS), the samples were prepared in a procedure displayed in Figure 7.1. Lipids were mixed in chloroform, desiccated and finally dispersed in a mixture of 60%vol water and 40%vol ethanol (see Figure 7.1a) by the group of Prof. Joachim Rädler. The lipids were labeled with BODIPY as a fluorescent dye for subsequent stability and tracking as well as co-localization studies. In parallel, CMS nanoparticles were synthesized by Dr. Valentina Cauda following the delayed co-condensation approach to achieve nanoparticles with an unfunctionalized core and an amino-propyl functionalized outer surface [9]. The external aminopropyl surface has been selectively functionalized with the dye ATTO633 (Figure 7.1b). Characterization measurements showed that spherically shaped nanoparticles with an average size of 50-80 nm and a mesoporous structure with pore sizes of about 3.7 nm were obtained. The particles were then employed for the synthesis of SLB@CMS using a solvent-exchange method. In this method monomeric lipids (DOPC or POPC, see Figure 7.1d) dissolved in ethanolic solution self-assemble into solid surface-supported bilayers or liposomes as the water content of the solution is increased toward 100%vol [228]. By suspending the CMS nanoparticles in the lipid solution, a supporting surface is offered for lipid bilayer formation upon water addition to the solvent (up to 95%vol), thus allowing a direct and efficient coverage of the silica surface (Figure 7.1c). The resulting SLB@CMS nanoparticles have a size of about 60-100 nm. To probe the effective assembly and integrity of the supported lipid bilayer on single CMS nanoparticles *in vitro*, dye release studies were performed by Dr. Valentina Cauda. For this studies the dye fluorescein was loaded into the CMS nanoparticles and the particles were capped by a DOPC-SLB. The particles were subsequently confined in a tube sealed by a dialysis membrane which is impermeable for the particles, but permeable for fluorescein. This tube was placed on a fluorescence cuvette filled with water and the emission intensity of the solution in the cuvette was measured after excitation with 512 nm light. In case of fluorescein-loaded, but uncoated CMS (without supported lipid bilayer), a fast fluorescence increase in the cuvette was observed reaching a plateau after 10 min (see

blue line with boxes in Figure 7.2). In contrast, fluorescein-loaded SLB@CMS nanoparticles (with intact lipid bilayer) show no fluorescence increase within 1h. After disruption of the lipid bilayer by the surfactant triton X-100, however, the fluorescein fluorescence increased up to the value of the uncapped control sample within 60 min (see red line with triangles in Figure 7.2). The data suggest that SLB@CMS nanoparticles are an intact and defect-free delivery system for fluorescein showing no dye leakage from the particles in the observed time interval of 1 hour. However, the release kinetics from the capped, but lysed CMS (100% within 60 min) is much slower than from the uncapped CMS (100% released dye within 10 min). A probable explanation for this effect is the higher diffusion resistance for the dye molecules due to the presence of lysed lipid fragments on the CMS surface. Due to the positive results *in vitro*, the nanoparticle uptake and mode of action on a single-cell level were examined by live-cell imaging.

7.1.2 Mode of cellular uptake of POPC-SLB@CMS

The first barrier nanoparticles encounter in cell culture is the plasma membrane of the cell. Besides endocytosis, fusion of the particles bilayer with the cellular plasma membrane is another possible way of nanoparticles internalization into cells, as reported for some enveloped viruses [229] and artificial model cell systems [230]. To learn more about the mode of uptake of SLB@CMS nanoparticles, dual-color SLB@CMS nanoparticles were prepared with BODIPY-labeled POPC lipids in the SLB and ATTO633-labeled CMS nanoparticles. The particles have been incubated with HuH7 cells for up to 4 hours and the fluorescence of both the ATTO633-labeled nanoparticles and the BODIPY-labeled SLB were recorded in two separated channels on a spinning disk confocal fluorescence microscope. Under the measurement conditions, no crosstalk of the dyes was detected. The channels were merged after acquisition. Co-localization of both BODIPY and ATTO633 fluorescence signals indicates intact uptake via endocytosis. In case of fusion or hemi-fusion with the plasma membrane, we expect a loss of BODIPY fluorescence on the particle location.
An overlay of the two channels is shown in Figure 7.3a. The fluorescence of BODIPY-labeled POPC lipid and ATTO633-labeled nanoparticles are displayed in Figure 7.3b and c respectively. The results clearly show co-localization of both components over the entire time span of the experiment, even after the particles have been internalized by the cell which was verified by the particle's localization in the z-stack and their motion pattern with active transport along microtubules. In addition to HuH7 cells, HeLa and 3T3 cells were examined with respect to their uptake route. However, all three cell lines showed similar results. From the data, we can conclude that the particles have been mainly internalized by endocytosis resulting in particles with intact bilayer as indicated by the two colors.

7.1.3 Colchicine delivery from SLB@CMS nanoparticles

Despite the fact that the SLB-coated CMS nanoparticles are primarily taken up into the cells by endocytosis and therefore end up trapped inside endosomes or lysosomes, we wanted to examine whether the SLB@CMS nanoparticles still have the ability to deliver drugs to cells. Therefore we

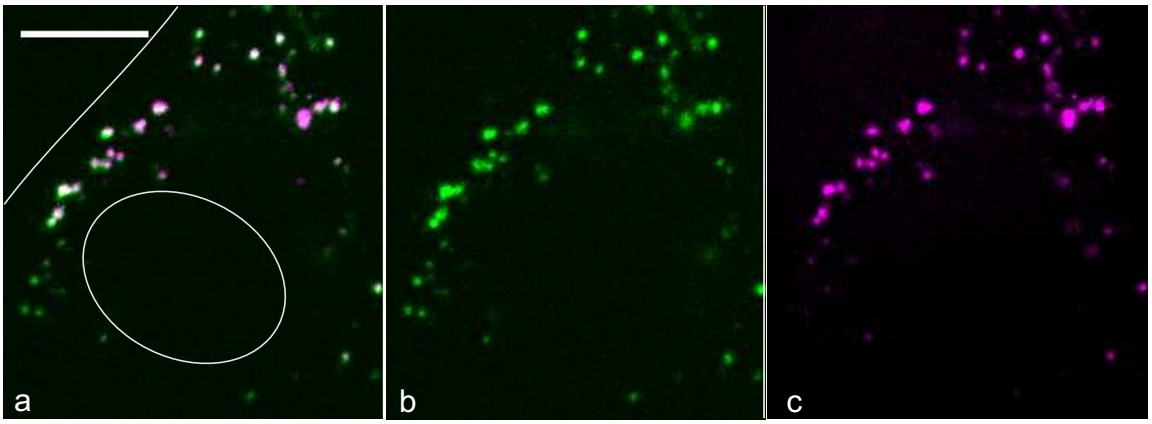

Figure 7.3: Co-localization of BODIPY-labeled lipids and ATTO633-labeled CMS of the POPC-SLB@CMS after 117 min of incubation with HuH7 cells. HuH7 cells have been exposed to POPC-SLB@CMS for 117 min. The lipids are labeled with BODIPY (green) and CMS is labeled with ATTO633 (magenta). (a) Overlay of the green BODIPY channel (shown in b) and the magenta ATTO633 channel (shown in c). White spots indicate co-localization, corresponding to intact POPC-SLB@CMS nanoparticles. The white circle and line show the nucleus and cell border respectively, as determined by a transmitted light image. All the particles are within the cell border and show co-localization of lipid and CMS fluorescence. The images are overlays of three z-planes. Scale: 10 µm.

loaded CMS nanoparticles with the anti-cancer drug colchicine. Once inside the cytosol, colchicine forms stable complexes with tubulin heterodimers [231], the building blocks for microtubules and effectively inhibits and perturbs the assembly dynamics at the microtubule ends [232]. As microtubules are essential for cell division, the ability of cells to proliferate is inhibited by colchicine [233]. After colchicine-loading into unlabeled nanoparticles a POPC lipid bilayer was formed and free colchicine was removed by centrifugation. HuH7 cells expressing GFP-labeled tubulin were incubated with the POPC-SLB@CMS nanoparticles for 6 to 7 hours. The morphology of the GFP-labeled microtubules was imaged on a spinning-disk confocal microscope (see Figure 7.4). As a result, untreated control cells (Figure 7.4a) show an intact microtubule network. Incubation of cells with colchicine-loaded nanoparticles, however, cause cell morphologies with disordered microtubuli, nuclei as well as cell edges (Figure 7.4b). These findings indicate that colchicine-loaded POPC-SLB@CMS nanoparticles are causing toxic effects on cellular microtubules. However, the mechanism of colchicine delivery was not clear at that stage of the experiments.

To understand the mechanism of colchicine delivery in more detail and to trace individual colchicine-loaded CMS nanoparticles, we incubated ATTO633-labeled nanoparticles with HuH7 cells containing GFP-labeled microtubules. This allows an interpretation of the observed effects on a single-cell level. Imaging was performed on a spinning disk confocal microscope using two detection channels for the separation of fluorescence signals above and below 592 nm respectively. The two detection channels were overlaid to obtain the images shown in Figure 7.5. A well-ordered and intact microtubule network is observed for both untreated HuH7 cells (representative cells shown in Figure 7.5a in green) and cells (in green) incubated with colchicine-loaded POPC-SLB@CMS nanoparticles (in magenta) for 25 min (Figure 7.5b). However, after 2 hours of colchicine-loaded POPC-SLB@CMS

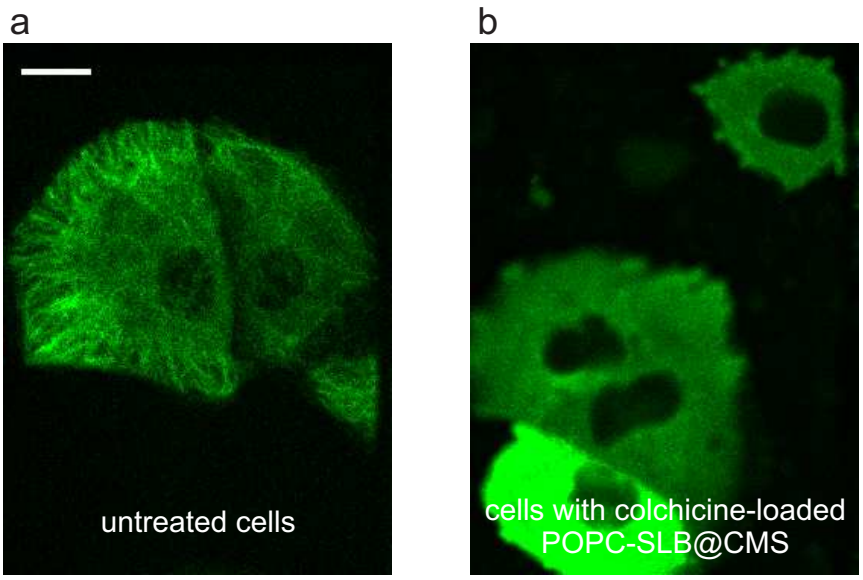

Figure 7.4: Effect of non-labeled SLB@CMS loaded with colchicine on the microtubule morphology of HuH7 cells. (a) Spinning disk confocal microscopy of untreated HuH7 cells shows intact GFP-labeled microtubules (in green). (b) Cells incubated with colchicine-loaded, unlabeled POPC-SLB@CMS for 8 hours show clear signs of colchicine toxicity. A lack of microtubule filaments together with disrupted nuclear morphology and cell edges can be observed. Scale bar: 10 µm.

incubation with the cells, the well-structured network has vanished and microtubule fragments and a diffuse green fluorescence is detected. A cross-section through the cell volume (inset in Figure 7.5c) clearly shows internalized nanoparticles appearing in white due to the overlay of the green cell interior and the magenta nanoparticles. In addition, several magenta spots can be detected on the cell surface. 24 min later, the morphology of the same cell has changed dramatically as demonstrated in Figure 7.5d. The cell shrunk and appears to be flat and dead. We attribute the observed effects to the uptake of colchicine-loaded POPC-SLB@CMS nanoparticles into cells. Previous quenching studies with nanoparticles (polyplexes, magnetic lipoplexes and PEGylated CMS nanoparticles) showed, that after 20 min only a small fraction of the applied particles (16-20 % in case of polyplexes and magnetic lipoplexes in HuH7 cells and 22 % of the PEGylated CMS in HeLa cells) have been internalized [1, 2, 234]. This is an explanation, why after 25 min no colchicine-induced effects were visible on the HuH7 cells. However, we know that the uptake of nanoparticles into cells increases with time [235], leading to a considerable degree of internalization after 2 hours. Therefore, it is not surprising that the toxic effect of colchicine was found to be pronounced at this timepoint. Therefore, our model is the following: Colchicine-loaded POPC-SLB@CMS are taken up into the cell, followed by a release of the colchicine of the nanoparticles, leading to microtubule depolymerization and cell death. However, it is still not known how exactly the colchicine is released.

To study the release mechanism in more detail, we performed control experiments. First, we wanted to verify that the internalized carrier POPC-SLB@CMS alone is not responsible for the loss of mi-

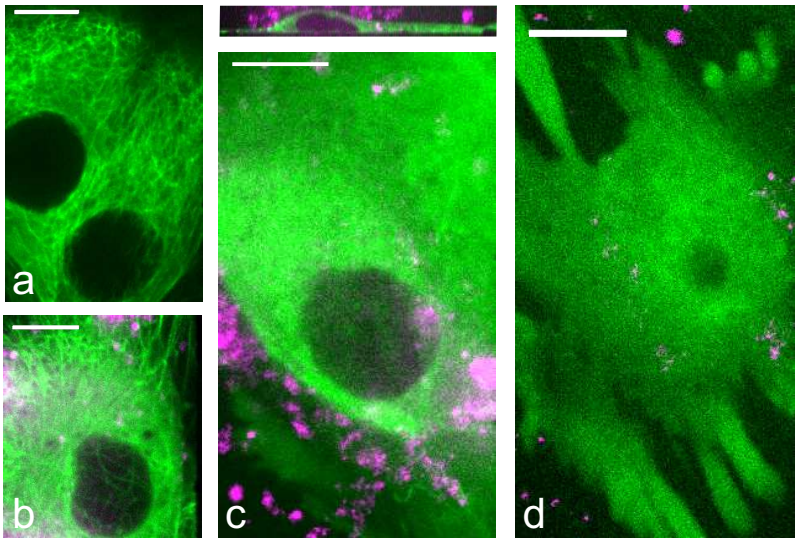

Figure 7.5: Drug delivery by colchicine loaded POPC-SLB@CMS nanoparticles to HuH7 cells. (a) Spinning disk confocal live-cell imaging of untreated HuH7 cells showing GFP-labeled microtubuli (green). (b) HuH7 cells (green) exposed to colchicine-loaded POPC-SLB@CMS (CMS in magenta) for 25 min. (c) After 120 min of incubation, the microtubule network vanished resulting in a diffuse fluorescence. Inset: Side view of the same HuH7 cell with internalized nanoparticles depicted in white (overlay of green and magenta colors) and nanoparticles on top of the cell in magenta. (d) After 144 min the cell morphology was disintegrated, indicating cell death. Scale bar: 10 µm.

crotubule structure. In this experiment, unloaded POPC-SLB@CMS nanoparticles were incubated with HuH7 cells for 2 hours. Location of the particles within the cell volume was verified by a z-stack combined with typical, intracellular motion. Figure 7.6a shows a representative HuH7 cell with intact microtubule network (green) and internalized POPC-SLB@CMS nanoparticles (shown in magenta). We conclude that the lipid-coated carrier taken up into the cell does not have an effect on the microtubule network of the cell. The observed toxicity should therefore be attributed to colchicine, the loaded drug. It is known that colchicine has a small permeability across cell membranes [236], the question is, how much colchicine is subject to premature release. In a second set of control measurements, we therefore studied how the colchicine is released from the carrier. Dr. Valentina Cauda performed *in vitro* release experiments in a fluorescence cuvette for this purpose. Colchicine was loaded into the CMS nanoparticles, a POPC lipid bilayer was built and the particles were loaded into the tube sealed by a dialysis membrane. This tube was placed on a fluorescence cuvette filled with water and the emission intensity of colchicine leaking out of the particles and through the dialysis membrane into the solution was measured for 115 min. Indeed, a slight release of colchicine was observed within the first 60-80 min reaching a plateau afterwards (see Figure 7.6b). SLB disruption by ethanol lead to a significant increase in colchicine fluorescence in the cuvette. In this control measurement, we wanted to investigate the effect of colchicine leached from the nanoparticles into the cell culture medium before cellular uptake of the nanoparticles. Therefore, instead of adding the colchicine-loaded POPC-SLB@CMS nanoparticles directly into the cell medium, we

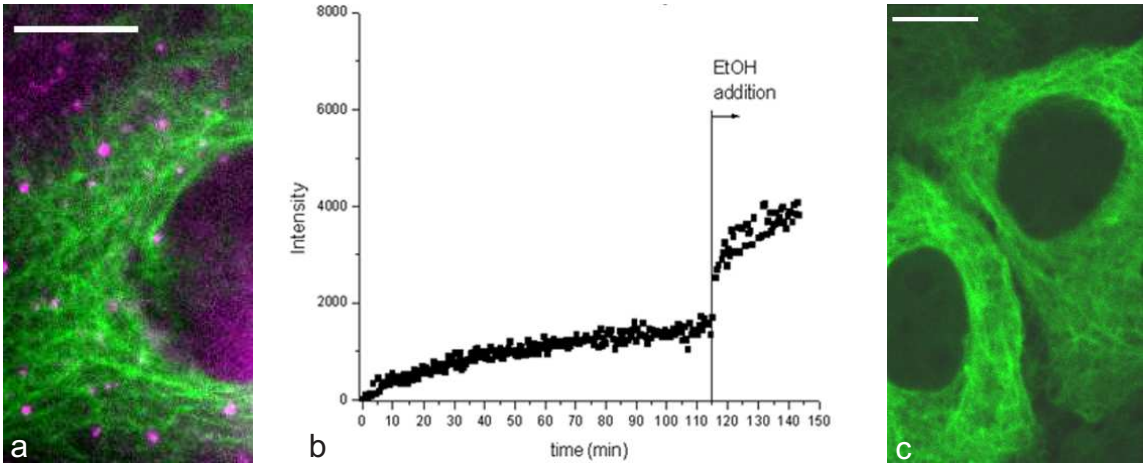

Figure 7.6: Effect of POPC-SLB@CMS and leaked colchicine on HuH7 cells. (a) HuH7 cells (green) after 2 h of incubation with POPC-SLB@CMS without colchicine (magenta). (b) *In vitro* release of colchicine from POPC-SLB@CMS, using the dialysis-capped tube fitting on the fluorescence cuvette. (c) HuH7 cells exposed to released and dissolved colchicine from POPC-SLB@CMS that have been confined into the dialysis-capped tube on the cell culture holder. After 6 h the microtubule network of the HuH7 cells was still intact. Scale bar: 10 µm.

pipetted the same amount of nanoparticles (used for the experiments shown in Figure 7.5) into the cap used for the *in vitro* release experiment. The cap was closed with the dialysis membrane and the membrane was brought in contact with the cell culture medium covering the HuH7 cells. In this arrangement only released colchicine, but not the nanoparticles can diffuse through the dialysis membrane and get in contact with the cells. Even after 6 hours of exposure to free colchicine diffusing out of the drug-loaded POPC-SLB@CMS nanoparticles, the microtubule network remained intact (see Figure 7.6c). This result suggests that the amount of colchicine leaking out of the SLB is too low to induce microtubule depolymerization and cell death. Thus, cell death is caused by colchicine delivery from POPC-SLB@CMS into the HuH7 cells.

In summary, we developed and tested a new drug delivery platform, CMS nanoparticles covered with a supported lipid bilayer *in vitro*, and in living cells. The lipid bilayer proved to be a seal against premature release of fluorescent dyes and even a good barrier against the slightly membrane-permeable drug colchicine. We showed, that colchicine delivery mediated by SLB@CMS nanoparticles is more efficient than the same dose of drug in solution. We postulate, that this is due to delivery of a small, concentrated dose inside the cell rather than a slow infiltration of colchicine from a diluted extracellular pool. This enhancement effect, if substantiated in systemic delivery, would improve cancer drug administration as lower drug doses could be applied to the patients.
Despite the fact that we successfully delivered colchicine to cancer cells, this system has the disadvantage that the mechanism of drug delivery was dependent on the ability of colchicine to permeate through lipid bilayers. One idea to overcome this problem and to make the system applicable for membrane-impermeable drugs as well, is to induce fusion of the particles on the plasma membrane

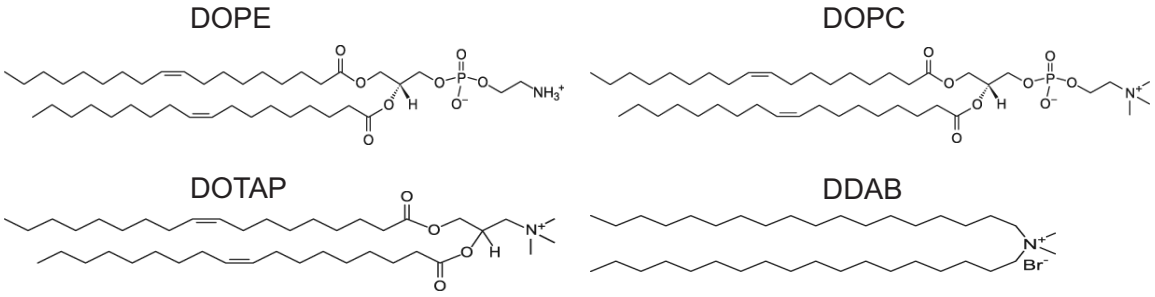

Figure 7.7: Lipids examined as supported lipid bilayers on CMS nanoparticles. DOPE and DOPC are neutral phospholipids. DOTAP and DDAB are cationic lipids.

or endosomes leading to delivery of the nanoparticle into the cytoplasm while retaining the lipid bilayer on the membrane.

7.2 Variation in SLB composition and the influence on CMS uptake

In Chapter 7.1, we studied the uptake of POPC-SLB@CMS nanoparticles and delivery of colchicine into living HuH7 cells. The nanoparticles showed internalization into cells by endocytosis. To avoid endo/lysosomal degradation, fusion of SLB@CMS nanoparticles with the plasma membrane of living cells has the potential to deliver CMS to the cytoplasm, while retaining the SLB at the plasma membrane. Experimental data on lipid vesicle fusion indicates that variation in lipid composition plays an important role for fusogenicity [227]. Therefore, we studied the influence of different lipid-compositions on the mode of cellular uptake and possibly find a composition featuring fusion.
To find SLB@CMS nanoparticles that are fusion-competent, CMS nanoparticles were equipped with supported lipid bilayers of dioleoyl-phosphatidylethanolamine (DOPE), dioleoyl-sn-glycero-3-phosphocholine (DOPC), dioleoyl-trimethylammonium propane (DOTAP), didodecyldimethylammonium bromide (DDAB) (see Figure 7.7) and mixtures thereof. In addition the positively-charged surfactant cetyltrimethylammonium bromide (CTAB) has been mixed with the lipids in different molar ratios. The dye-labeled lipid compositions have been provided by Dr. Hanna Engelke from Prof. Joachim Rädler's research group. For preparation of SLB@CMS nanoparticles, we used the solvent exchange method as described in Chapter 7.1.1.

7.2.1 Characterization of SLB@CMS nanoparticle integrity

To study the fusogenic activity of different lipids as SLB, it is essential to prepare intact SLB-sealed CMS nanoparticles. To examine the integrity, dual-color SLB@CMS nanoparticles have been prepared. The dual-color nanoparticles carry the fluorescent dye ATTO633 bound to the external aminopropyl surface of the CMS nanoparticles. The second label, BODIPY, is attached to the applied lipids. Lipids were chosen according to their favorable role in fusion. In general, liposomal

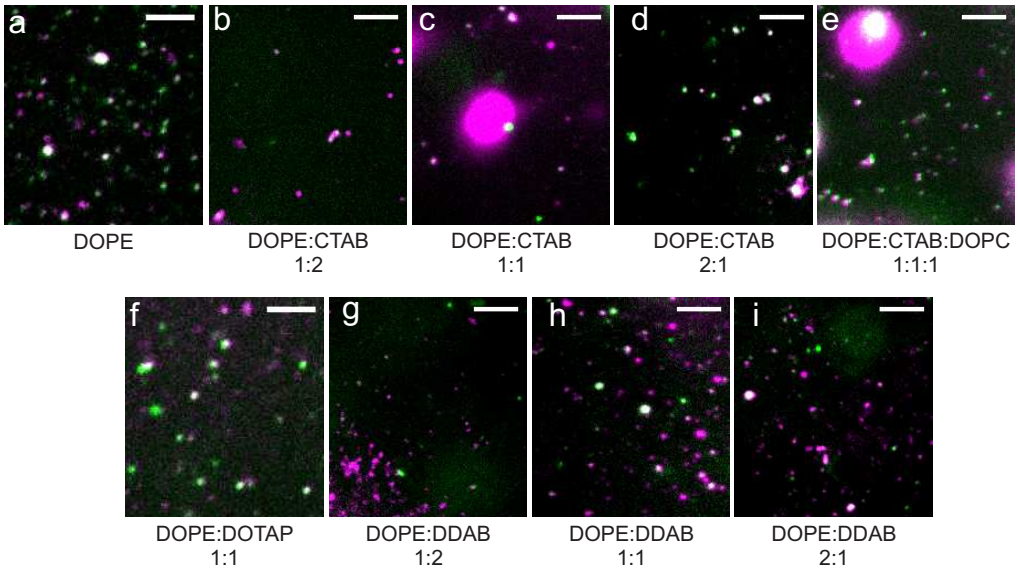

Figure 7.8: Integrity of SLB@CMS with different lipid compositions. SLB@CMS nanoparticles with varying lipid composition have been prepared and imaged on coverglass by wide-field (b-e, g-i) and spinning disk confocal microscopy (a and f). Co-localization of the nanoparticle and lipid bilayer fluorescence have been measured for SLBs composed of (a) DOPE ,(b) DOPE:CTAB 1:2, (c) DOPE:CTAB 1:1, (d) DOPE:CTAB 2:1, (e) DOPE:CTAB:DOPC 1:1:1, (f) DOPE:DOTAP 1:1, (g) DOPE:DDAB 1:2, (h) DOPE:DDAB 1:1 and (i) DOPE:DDAB 2:1 (molar ratios). Scale bar: 5 µm.

formulations oftentimes contain two lipid species, for example a cationic amphiphile combined with a neutral phospholipid, such as DOPE [237]. DOPE is known as a fusion-promoting lipid [238] with high destabilization properties. It was shown to promote fusion of lipid:DNA complexes with cellular membranes [237]. Lipid vesicle formulations containing DOPE were shown to be more fusogenic than the ones containing the neutral phospholipid DOPC [239]. However, as a widely-used helper lipid that fosters lipid bilayer formation, DOPC has been included in one of the formulations in this work. The cationic lipid DOTAP is known to be non-fusogenic [240]. However, in combination with DOPE (in ratios of DOPE/DOTAP, 1:9, 1:2.3, 1:1, 2.3:1, 9:1 molar proportion) it was shown to fuse with model membranes consisting of DOPS/DOPE/DOPC in a molar proportion of 1:1.7:4 [230]. Another cationic lipid, used in our study, is DDAB. DDAB liposomes were shown to be unstable at physiological pH and temperature, but the mixture of DDAB with DOPE (2.5:1) increased stability [241].

To assess the integrity of SLB@CMS nanoparticles and for further studies on living cells, co-localization of lipid bilayer (SLB) and nanoparticles was examined directly after sample preparation and before addition to the cells. Therefore, dual-color SLB-coated CMS have been sedimented on glass coverslips. The fluorescence of the nanoparticles was recorded in two separate channels for the detection of ATTO633-labeled CMS and BODIPY-labeled SLB, respectively. To remove out of focus fluorescence, a rolling ball background filter of 8 pix has been applied. Co-localization of BODIPY-labeled SLB and ATTO633-labeled CMS indicates intact particles. Representative co-localization

images are displayed in Figure 7.8. Successful synthesis is observed in case of DOPE-SLB@CMS nanoparticles. The nanoparticles show good co-localization of the BODIPY-labeled DOPE-SLB (depicted in green in Figure 7.8a) and ATTO633-labeled CMS (depicted in magenta in Figure 7.8a). Co-localization is indicated by white color due to overlay of green and magenta colors. In further samples, the addition of CTAB to the DOPE-bilayer in ratios of DOPE:CTAB 1:2 and 1:1 leads to large amounts of CMS without lipid bilayer (magenta only spots in Figure 7.8b and c). The samples are therefore not applicable for our cell experiments where nanoparticles without supported lipid bilayer are counted as fusogenic. This would lead to false-positive results. Reducing the amount of CTAB, such as in the sample DOPE:CTAB in the ratio of 2:1, leads to dual-color nanoparticles applicable for fusion experiments (see Figure 7.8d). Further addition of DOPC in a molar ratio of DOPE:CTAB:DOPC 1:1:1, as shown in Figure 7.8e, gives co-localizing dual-color CMS nanoparticles and will be used for the cell experiments. Reduced co-localization is found in case of DOPE:DOTAP in the molar ratio 1:1. Most of the nanoparticles were found dual-color, however, the sample preparation was inhomogeneous showing both green only and magenta only signals (see Figure 7.8f). This renders DOPE:DOTAP unsuited for cell experiments. DOPE:DDAB 1:2 preparation showed a majority of CMS nanoparticles without lipid bilayer. Further reduction of the DDAB content lead to better lipid bilayer formation, however, there were still numerous nanoparticles without lipid bilayer (see Figure 7.8g-i). Therefore, the DOPE:DDAB samples are not applicable for our co-localization studies.

To sum up, the experiment gave insight in the intactness of SLB formation on CMS depending on the lipids applied. Intact dual-color nanoparticles are a prerequisite for the experiments on a single-cell level. However, in this control experiment, we can not draw conclusions about fusogenicity of the lipid compositions. Pure DOPE-bilayers, SLB made from DOPE:CTAB in the ratio of 2:1 and SLB made from DOPE:CTAB:DOPC in the ratio of 1:1:1 turned out to be useful for experiments on nanoparticle uptake modes in living cells.

7.2.2 Mode of uptake for various SLB@CMS nanoparticles into living cells

After identification of lipid bilayer compositions that yield intact dual-color SLB@CMS nanoparticles (DOPE, DOPE:CTAB 2:1 and DOPE:CTAB:DOPC 1:1:1), the role of fusion for internalization of these compositions was determined. For this, HuH7 cells were incubated with the dual-color SLB@CMS nanoparticles for multiple hours to ensure a high degree of intracellular location. Fluorescence microscopy of the cells has been performed in two channels to detect BODIPY-labeled lipids and ATTO633-labeled CMS, respectively. To remove out of focus fluorescence from different cellular planes, a rolling ball background filter of 8 pix has been applied [217]. Internalized nanoparticles are detected by their typical motion pattern showing active transport. Co-localization analysis indicates that internalized particles, showing both BODIPY and ATTO633 fluorescence, have been taken up via endocytosis, whereas nanoparticles with intracellular CMS-ATTO633 fluorescence without co-localizing lipid-headgroup BODIPY fluorescence fused with the target cell membrane.

DOPE-SLB@CMS nanoparticles have been incubated with HuH7 cells for 3 h. Image acquisition occurred on a spinning disk confocal microscope in three successive z-planes through the cell in-

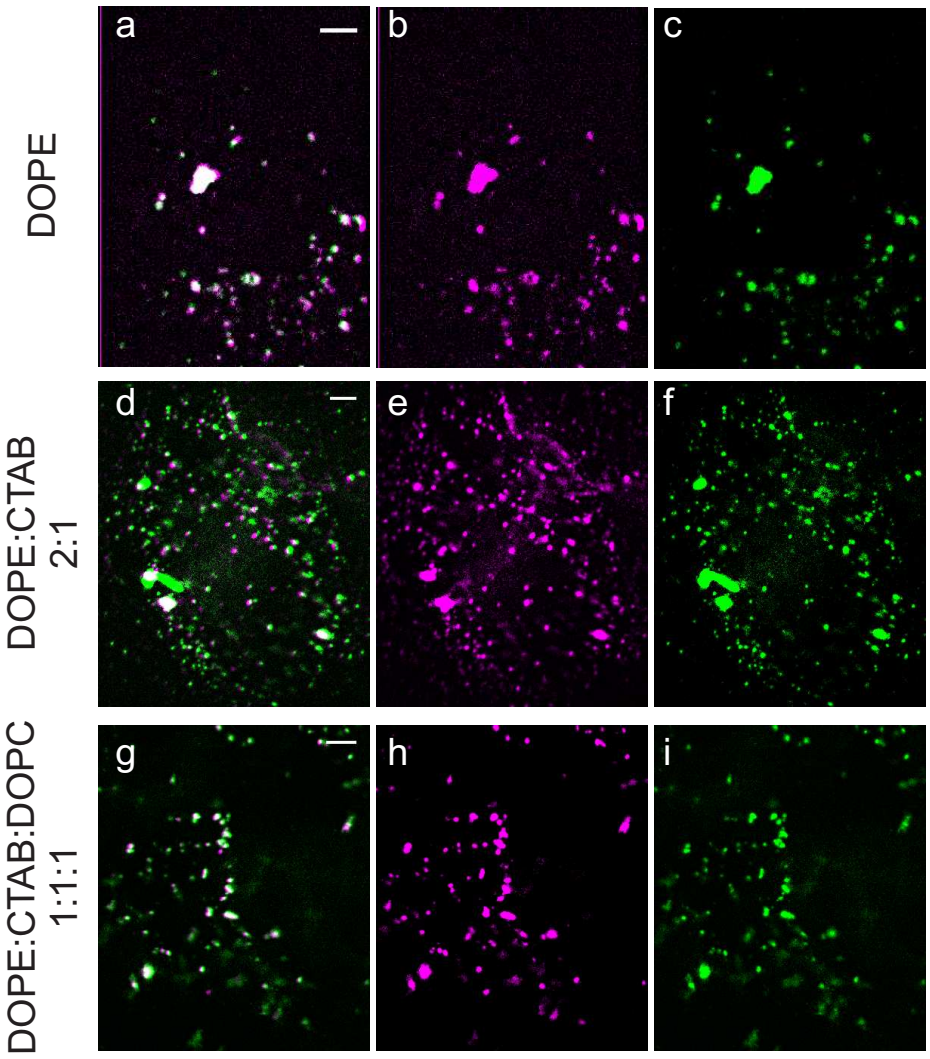

Figure 7.9: Co-localization of cell associated nanoparticles consisting of BODIPY-labeled lipids and ATTO633-labeled CMS. HuH7 cells have been exposed to SLB@CMS for multiple hours. CMS is labeled with ATTO633 (magenta) and the lipids are labeled with BODIPY (green). The lipid bilayers consisted of (a-c) DOPE, (d-f) DOPE:CTAB 2:1 and (g-i) DOPE:CTAB:DOPC 1:1:1. For the corresponding lipid compositions, overlays (shown in a, d, g) of the magenta ATTO633 channel (shown in b, e, h) and the green BODIPY channel (shown in c, f, i) have been performed. White spots in the overlay images indicate co-localization, corresponding to intact SLB@CMS nanoparticles. All the cell-associated particles show co-localization of lipid and CMS fluorescence. The images are filtered by a rolling ball background filter of 8 pix. Scale bar: 5 µm.

terior. The z-planes were overlaid as well as the two channels. Co-localization of CMS-ATTO633 nanoparticles (depicted in magenta, Figure 7.9b) with the BODIPY-labeled DOPE-SLB (depicted in green, Figure 7.9c) is displayed in Figure 7.9a. As the internalized particles still co-localize with their DOPE-SLB (white color in Figure 7.9a), there was no indication, that -under our measurement conditions- fusion on the plasma membrane of the cells is the predominant uptake route. DOPE:CTAB 2:1 as SLB on CMS nanoparticles have been incubated with the cells for 6.75 h and imaging occurred on a fluorescence wide-field microscope in two channels. Complete co-localization (see Figure 7.9d) of all CMS-ATTO633 nanoparticles (depicted in magenta in Figure 7.9e) with BODIPY-labeled SLBs consisting of DOPE:CTAB (depicted in green in Figure 7.9f) is observed. DOPE:CTAB:DOPC in a composition of 1:1:1 as SLB on CMS nanoparticles has been incubated with HuH7 cells for 8.5 h. Imaging occurred by wide-field fluorescence microscopy. The results are depicted in Figure 7.9g-i. Co-localization analysis showed that all internalized nanoparticles were dual-color. One possible explanation is that the lipid bilayer is stabilized by its CMS support leading to reduced interactions with the cellular membranes. Taken together, the data suggest that none of the tested SLB-compositions induced fusion of the SLB@CMS nanoparticles with the plasma membrane.

In summary, out of nine tested lipid compositions, only three formed intact supported lipid bilayers on the CMS nanoparticles. The compositions yielding functional dual-color nanoparticles were DOPE, DOPE:CTAB 2:1 and DOPE:CTAB:DOPC 1:1:1. After long incubation times of multiple hours, the CMS nanoparticles have been internalized together with their SLB. This means that fusion on the plasma membrane of the cells is not the predominant uptake route for the tested compositions. Ideas for improvements to finally achieve fusion on the plasma membrane can be found in biological systems where fusion is highly regulated and mediated by specialized proteins. Prominent examples of fusion proteins are glycoproteins of enveloped viruses such as the hemagglutinin fusion protein of influenza virus [242]. In addition, SNARE proteins are crucial for the intracellular membrane fusion processes in eukaryotes [243]. The application of fusion proteins in a lipid bilayer might help to facilitate fusion on the plasma membrane.

7.3 Summary

In this chapter, we presented an efficient and reproducible method, based on solvent exchange, to encapsulate individual core-shell CMS nanoparticles of 50 nm diameter with an intact lipid bilayer. The novel SLB@CMS nanoparticles feature a high capacity for the incorporation of drugs into the mesopores. *In vitro* experiments show the complete sealing of the CMS nanoparticle by the lipid bilayer and the absence of premature release of guest molecules such as dyes and prove the stability of the SLB acting as a capping system. The *in vitro* displacement of the lipid bilayer by triton leads to the opening of the mesopores. Uptake experiments showed that SLB@CMS nanoparticles were taken up intactly by endocytosis. As a proof of principle, we showed the delivery of the microtubule depolymerizing drug colchicine into HuH7 liver cancer cells. This experiment clearly exposes the

important role of the SLB, mostly preventing the release of the drug under undesired conditions and allowing delivery into the cell by uptake of the nanoparticles. The microtubule network of the cells is destroyed within 2 h of incubation with the colchicine-SLB@CMS nanoparticles, thus showing an enhanced effect compared to the same dose of colchicine in solution. We believe that the enhancement is due to the fact that colchicine delivery mediated by SLB@CMS nanoparticles results in small concentrated doses rather than slow infiltration of colchicine from a rather diluted extracellular pool. However, the proposed system has the disadvantage that it is not applicable for membrane-impermeable drugs. One idea to overcome this problem is to induce fusion of the particles on the plasma membrane leading to delivery of the nanoparticle into the cytoplasm while retaining the lipid bilayer on the cellular membrane. The cell entry mechanism would open the pores, enabling intracellular release of the cargo. Different lipids have been examined as supported lipid bilayer on CMS, however, most of them did not form intact dual-color SLB@CMS nanoparticles. Incubation of DOPE, DOPE:CTAB in a molar ratio of 2:1 and DOPE:CTAB:DOPC 1:1:1 SLB@CMS nanoparticles with HuH7 cells for multiple hours revealed that the nanoparticles show endocytosis as their major mode of uptake. Further screening of different lipid compositions might help to find a fusion-competent lipid bilayer composition, however further modification of the nanoparticles with fusion proteins or peptides is more promising.

In summary, SLB@CMS nanoparticles is a good system for pore sealing after drug loading, one major drawback of the system is, that it is not useful for “controlled drug release”. Therefore, in a next step a system with the ability for controlled release was developed.

8 Disulfide-based drug delivery induced by photochemical internalization (PCI)

In the previous chapter, we reported on SLB-coated CMS that are taken up into cells by endocytosis and release colchicine, however, not in a controlled fashion. To achieve controlled drug release into the cytosol, various stimuli can be applied (for details see Chapter 3.3). One such stimulus is light irradiation. To perform light-triggered drug release and to overcome the endosomal membrane as a barrier to cytosolic drug delivery, we used photochemical internalization (PCI). PCI is based on light activation of a photoactive compound (photosensitizer). One such photosensitizer is the amphiphilic porphyrin derivative disulfonated *meso*-tetraphenylporphine ($TPPS_{2a}$). Due to its chemical composition (see Figure 8.1), it inserts into the plasma membrane -while incubated with the cells- and specifically locates in the membrane of endocytic vesicles [81, 244, 245]. Upon exposure to light of 405 nm, $TPPS_{2a}$ is excited to its singlet state, followed by intersystem crossing to its triplet state. This excited state is then quenched by triplet oxygen producing highly reactive oxygen species (ROS) [246], such as singlet oxygen. Singlet oxygen in turn is able to oxidize amino acids, unsaturated fatty acids, cholesterol and leads to the collapse of the endosomal membrane followed by release of the endosomal content into the cytosol [80]. It is important to note, however, that the range of action of singlet oxygen remains locally confined (10-20 nm) due to its very short lifetime of 10-40 ns inside cells [247]. For this reason, singlet oxygen mainly reacts with the endosomal membrane and the damage to the endosomal cargo is expected to be low.

The CMS nanoparticles to be delivered by PCI are designed for redox-driven intracellular disulfide-cleavage, releasing the cargo upon contact with the reducing milieu of the cytoplasm. To achieve this the cargo molecules are bound via a disulfide linker to the inner volume of CMS nanoparticles. This procedure has the advantage that the cargo is protected inside the porous host material while no synthetically demanding valve is needed to prevent premature release of the cargo. The concept of disulfide-bound agents inside the pore system of mesoporous silica has been initially studied by Mortera *et al.* [124]. The authors used the membrane-impermeable amino acid cystein (Cys) as a cargo. Cystein delivery into cells promotes the synthesis of glutathion (GSH), which plays a central role in cell biology and is depleted in a number of diseases including cancer as well as neurodegenerative and cardiovascular diseases [248]. For the study of Mortera *et al.*, Cys was released from MSN based on disulfide bridge cleavage [124]. However, the authors did not report on the cellular uptake mechanism and the specific locus as well as the time point of reduction inside the cells. In the following, we elucidate the role of endosomal escape for disulfide-based drug delivery from CMS nanoparticles by real-time live-cell imaging of the photochemical release process. The results of this study are described in this chapter and have been published in Nano Letters (see

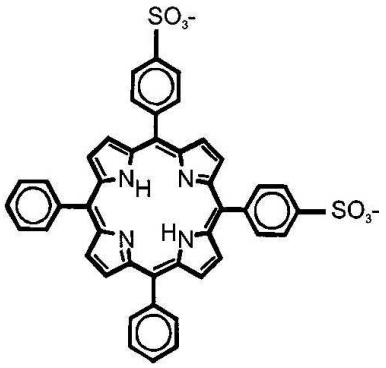

Figure 8.1: $TPPS_{2a}$. Chemical structure of disulfonated *meso*-tetraphenylporphine with the sulfonate groups on adjacent phenyl rings ($TPPS_{2a}$).

reference [13]).

First, a short description of the particle synthesis and the applied samples will be given. In a second part, the cargo release of disulfide-bridged CysATTO633 from CMS upon addition of a reducing agent will be monitored by single-particle fluorescence microscopy *in vitro*. Afterwards, live-cell imaging of HuH7 cells incubated with the nanoparticles for up to two days will be presented. In a last step, photochemically induced endosomal release of CMS is followed by live-cell imaging. Imaging of the release process in great detail enables mechanistic insights and further improvements on the drug delivery systems.

8.1 Synthesis of CMS for disulfide-based drug delivery

CMS nanoparticles for disulfide-based drug delivery have been synthesized by Dr. Axel Schlossbauer from the group of Prof. Thomas Bein (LMU Munich). The particles were prepared according to the sequential co-condensation method with a mercaptopropyl-functionalized core, surrounded by pure silica and an aminopropyl-functionalized shell. After template extraction, CMS nanoparticles have a diameter of 80 nm and a pore size of 3.8 nm. In case of the CMS nanoparticles for disulfide-based drug delivery, the aminopropyl-functionalized shell was labeled with ATTO488 and the mercaptopropyl-functionalized core was activated with 2-2'-dithiopyridine (DTP), followed by reaction with ATTO633-labeled cystein. This resulted in disulfide-bridged, ATTO633-labeled cysteine attached to the inner pore walls of the particle core (see Figure 8.2a). The sample will be referred to as CMS-CysATTO633$_{\text{core}}$-ATTO488$_{\text{shell}}$. The synthesis of this sample has been monitored by Raman spectroscopy (for details see [13, 249]). In addition, three other samples have been prepared. The sample CMS-CysATTO633$_{\text{core}}$-NH$_{2\text{shell}}$ contains an unlabeled shell (see Figure 8.2b). The samples CMS-ATTO633$_{\text{core}}$-ATTO488$_{\text{shell}}$ and CMS-ATTO633$_{\text{core}}$-NH$_{2\text{shell}}$ are control samples without disulfide-linker. Both samples contain ATTO633-labeled cores (see Figure 8.2c and d), but ATTO633 is not bound via disulfide bridges and is therefore uncleavable in reducing milieu.

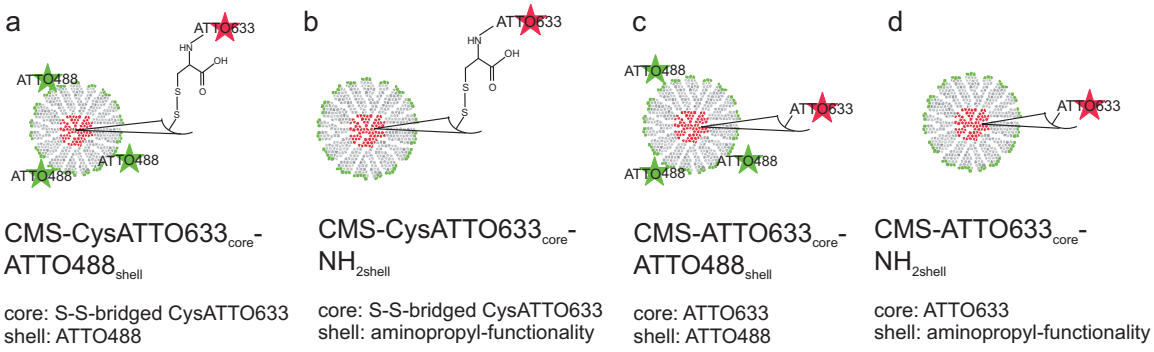

Figure 8.2: CMS samples for disulfide-based drug delivery.

8.2 Single-particle characterization *in vitro*

To examine whether the disulfide bridges inside the nanoparticle core are cleavable by reductive milieu, first experiments have been performed *in vitro* with CMS nanoparticles on glass. This first proof of principle measurements are essential to be able to interpret the more complicated cell culture experiments later on. The aim was to follow the release of dye-labeled cysteine at a single-particle level by fluorescence microscopy on-line. Therefore, CMS nanoparticles were dispersed in water, sedimented on glass coverslips and incubated with the reducing agent 10 mM GSH. Before ($t < 0$ min) and after ($t > 0$ min) addition of GSH, movies of the nanoparticles were recorded. From the movies, the mean fluorescence intensities of ATTO633-labeled particles and the background were extracted. The obtained intensities were normalized and plotted versus time (Figure 8.3). In Figure 8.3a, the relative CysATTO633 fluorescence intensities of CMS-CysATTO633$_{\text{core}}$-ATTO488$_{\text{shell}}$ nanoparticles (black) and background (gray) are displayed. After GSH addition, the CysATTO633 fluorescence of the background (gray curve) increases up to a factor of 2.3 reaching a plateau after 8 min. The increase of CysATTO633 background fluorescence intensity indicates successful release of the dye from the CMS nanoparticles and distribution of the cargo on the cover glass.

Surprisingly, the CMS-CysATTO633$_{\text{core}}$-ATTO488$_{\text{shell}}$ nanoparticles themselves (shown in Figure 8.3a, black curves) also showed an increase in CysATTO633 fluorescence intensity. This increase by a factor of 2 or more occurred within two minutes, on a faster time scale than the increase in background fluorescence, and was unexpected. Instead, we expected a decrease in the particle's CysATTO633 intensity after reductive dye release. However, the increase of nanoparticle-associated CysATTO633 intensity is easily explained by a dequenching effect of the pore-bound CysATTO633. The tight packing of the dye molecules inside the pores promotes a self-quenching of CysATTO633 similar to tightly packed octadecyl rhodamine B or calcein in liposomes [250]. The release of dye lowers the dye concentration within the pores below the limit for self-quenching and the residual dye molecules start fluorescing. The strong fluorescence of the nanoparticles also indicates that the disulfide-bound CysATTO633 is not completely released upon addition of GSH. The self-quenching effect of tightly packed ATTO633 in a constrained environment such as mesoporous silica has not been reported before. In our experiments, this self-quenching effect of CysATTO633 permits a

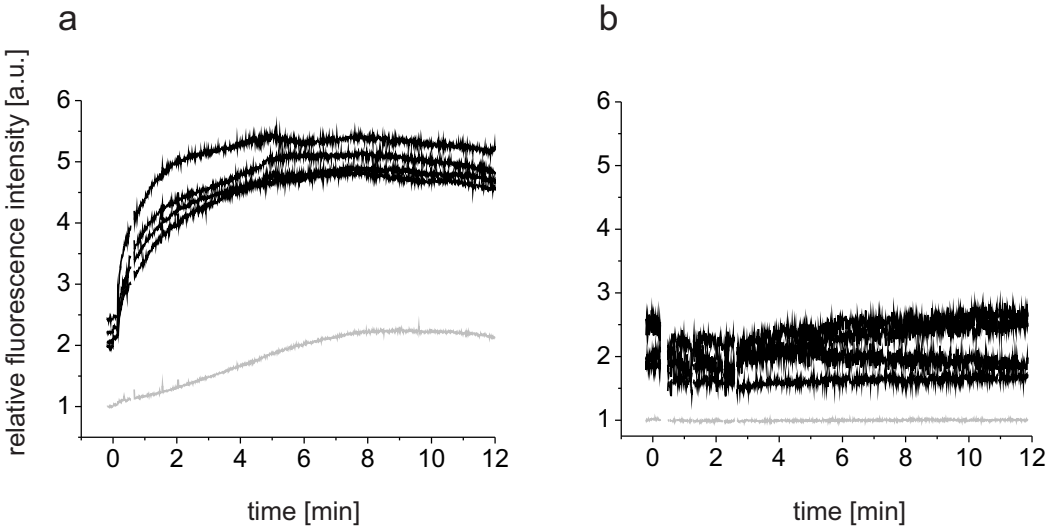

Figure 8.3: CysATTO633 release measured *in vitro* on a single-particle level. The mean fluorescence intensity of four single particles on glass (black curves) and background (gray curve) was extracted from a movie, normalized, and plotted versus time. The fluorescence intensity of ATTO633 was plotted for (a) redox-cleavable CMS-CysATTO633$_{\text{core}}$-ATTO488$_{\text{shell}}$ and (b) non-cleavable control CMS-ATTO633$_{\text{core}}$-ATTO488$_{\text{shell}}$ nanoparticles in water. At timepoint t=0 min 10 mM GSH was added to the samples. The movies were recorded at 642 nm illumination with an exposure time of 200 ms and a frame rate of 3.4 s^{-1}.

well-detectable readout for dye release with excellent signal-to-noise ratio.

As a control, CMS-ATTO633$_{\text{core}}$-ATTO488$_{\text{shell}}$ nanoparticles without cleavable disulfide linker were examined under similar conditions (Figure 8.3b). The fluorescence intensities of both the background and the particles remained constant and a dequenching effect was not observed after addition of 10 mM GSH (at t = 0 min). This result confirms that only dyes bound via a disulfide linker are released by GSH and that the release is associated with a strong increase of nanoparticle fluorescence intensity.

To summarize, we showed that release of disulfide-bound CysATTO633 from CMS nanoparticles in 10 mM GSH can successfully be observed at a single-particle level. The release was accompanied by a dequenching of the ATTO633 fluorescence and this effect permits a sensitive readout for successful dye release. The results of the experiment enabled us to further apply the CMS nanoparticles on living cells.

8.3 Long-term live-cell imaging of HuH7 cells incubated with CMS nanoparticles

To investigate whether the reductive milieu inside living cells is able to induce dye release from CMS nanoparticles, as monitored on glass, we examined living cells exposed to dual-color CMS-CysATTO633$_{\text{core}}$-ATTO488$_{\text{shell}}$ nanoparticles for up to 2 days. After this long time interval, we

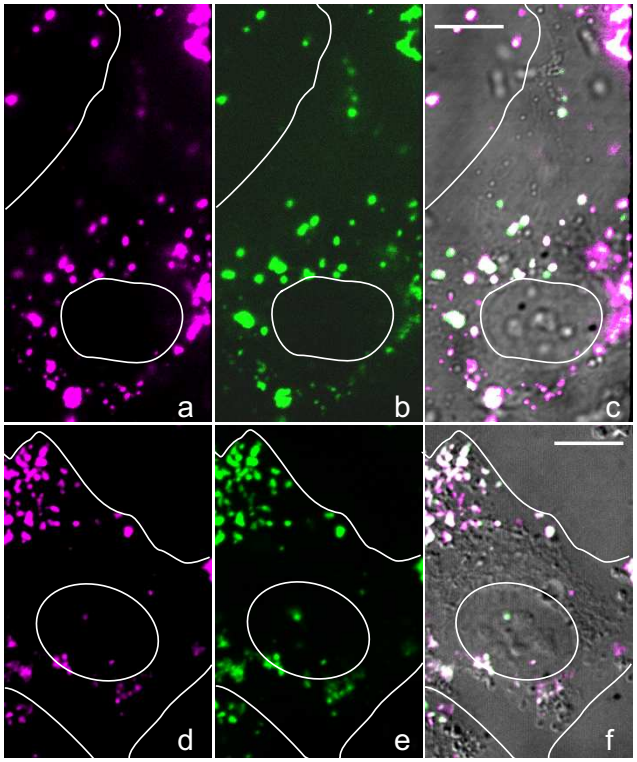

Figure 8.4: Spinning disk confocal microscopy of living HuH7 cells after long-term exposure to CMS-CysATTO633$_{\text{core}}$-ATTO488$_{\text{shell}}$ nanoparticles. z-projections are shown consisting of the overlay of three planes inside an HuH7 cell exposed to CMS-CysATTO633$_{\text{core}}$-ATTO488$_{\text{shell}}$ nanoparticles for 25 h (a-c) and 49 h (d-f). The cell nucleus is indicated by a white circle and the outer white line represents the cell border. Fluorescence of the particles' core (magenta a and d) and shell (green b and e) is highly co-localized as indicated by the white signal in the merged image (white c and f), which was superimposed on the transmitted light image of the cell. Scale bar: 10 µm.

expect the particles to be internalized to a high extent. In case of successful intracellular reductive CysATTO633 release, we expect to observe a reduction in co-localization between the two dyes.

To measure this, after 24 and 48 h of exposure, confocal z-stacks of HuH7 cells were acquired by spinning disk confocal microscopy and the co-localization of CysATTO633$_{\text{core}}$ and ATTO488$_{\text{shell}}$ was evaluated. Successful cell entry and intracellular localization of the CMS nanoparticles was detected by their characteristic intracellular motion such as transport by motor proteins [1, 2, 29] and the location within the z-stack.

Transmission light images of the cells showed no morphological signs of toxicity within our observation time. After 49 h, core-bound CysATTO633 and shell-bound ATTO488 signals of the intracellular particles were still co-localized. Additionally, fluorescence of free CysATTO633 in the cytoplasm was not detected. This indicates that within 49 h the disulfide-bound dye was not released. Two representative cells, after 25 h (Figure 8.4a-c) and 49 h (Figure 8.4d-f) of incubation, are displayed. Fluorescence of the particle's CysATTO633-core (magenta a and d) and shell (green b and e) was co-localized as indicated by the white signal in the merged image (white c and f), which was superimposed on the transmission light image of the cell.

Our results indicate that CMS-CysATTO633$_{\text{core}}$-ATTO488$_{\text{shell}}$ nanoparticles are taken up into HuH7 cells without detectable signs of toxicity. Reductive release of ATTO633-labeled cysteine from internalized particles was not detected within 49 h of incubation.

From the data obtained on uptake into living cells, including our own study presented here, it has been shown that cells internalize CMS nanoparticles into endocytic vesicles [13, 161, 251]. Entrapped

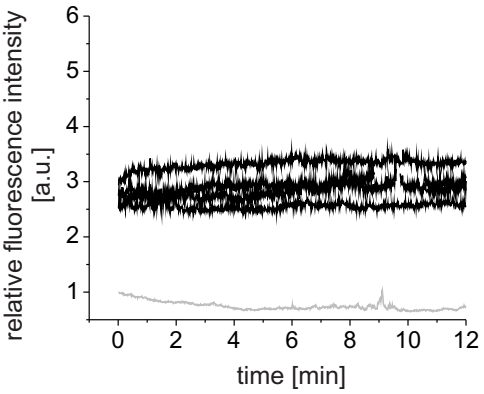

Figure 8.5: Influence of a $TPPS_{2a}$ solution on redox-cleavable CMS-$CysATTO633_{core}$-NH_{2shell}. Redox-cleavable CMS-$CysATTO633_{core}$-NH_{2shell} nanoparticles were incubated in a $TPPS_{2a}$ solution on glass coverslips on the microscope. $TPPS_{2a}$ was activated by a 405 nm laser. A movie was recorded at 642 nm illumination with an exposure time of 200 ms and a frame rate of $3.4\,s^{-1}$. The CysATTO633 intensity of single particles on glass (black curves) and background (gray curve) was extracted from the movie, normalized and plotted versus time.

in endocytic vesicles, CMS nanoparticles are not accessible to the reductive milieu of the cytosol. Surprisingly, Mortera *et al.* showed cytosolic fluorescence of reductively released cysteine [124]. However, they did not show the release process itself. In our mechanistic study, we could not detect reductive release of ATTO633-labeled cysteine.

8.4 Photochemically-induced endosomal release

To overcome the endosomal membrane barrier separating CMS nanoparticles from the cytosol and to gain mechanistic insight into the release at a single-cell level in real-time, photoinduced endosomal release is a promising strategy. In this method, the photosensitizer $TPPS_{2a}$ is incubated with the cells and incorporates into membranes via the endocytic pathway. By 405 nm laser light, $TPPS_{2a}$ is excited to its singlet state, followed by intersystem crossing to its triplet state. This excited state is then quenched by triplet oxygen producing singlet oxygen. Singlet oxygen is highly reactive and leads to a collapse of the endosomal membrane followed by release of the endosomal content into the cytosol.

To ensure that 405 nm light-activated $TPPS_{2a}$ in solution has no influence on the fluorescence intensity of CMS-$CysATTO633_{core}$-NH_{2shell} nanoparticles, control measurements have been performed *in vitro* on glass. For this, redox-cleavable CMS-$CysATTO633_{core}$-NH_{2shell} nanoparticles in $TPPS_{2a}$ solution have been sedimented on glass coverslips on the microscope. After activation of $TPPS_{2a}$ by 405 nm laser light for 1 min, a movie was recorded under 642 nm illumination. The CysATTO633 fluorescence intensities of single particles and background have been extracted, normalized and plotted versus time (see Figure 8.5). The fluorescence intensities of both the background (Figure 8.5 gray curve) and the particles (black curves) remain constant. This indicates that activated $TPPS_{2a}$ in solution has no influence on the fluorescence intensity of CMS-$CysATTO633_{core}$-NH_{2shell} particles, which is a prerequisite for further experiments in living cells.

To evaluate photochemically induced endosomal escape of CMS nanoparticles in living cells, a marker for endosomal opening was needed. For this purpose, we incubated the cells with the fluid phase marker Alexa Fluor 488 dextran (AFD). AFD is internalized by fluid-phase endocytosis

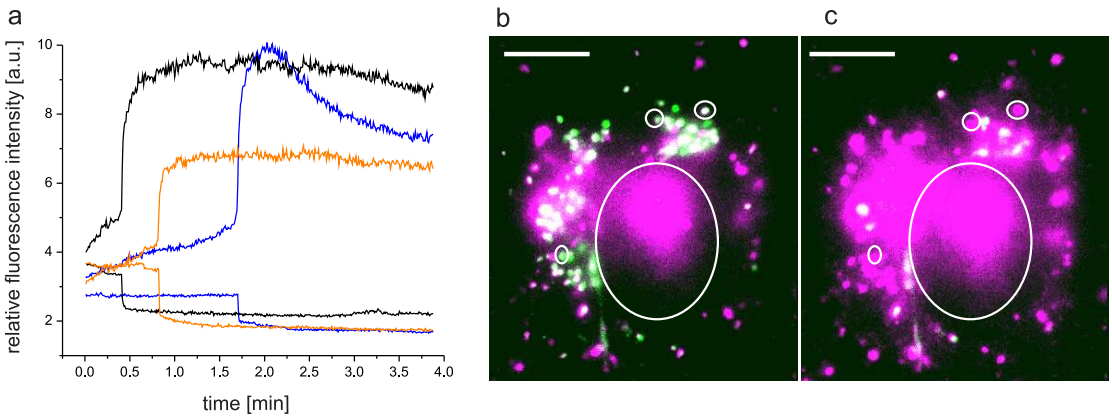

Figure 8.6: Photoinduced endosomal release of CMS-CysATTO633$_{core}$-NH$_{2shell}$ and fluid phase marker AFD inside living HuH7 cells monitored by wide-field fluorescence microscopy. The cells were exposed to the nanoparticles overnight. (a) Intensity plot of three exemplary tracked endosomes (highlighted by small circles in b and c) over time. The fluorescence intensity of CysATTO633 (upper three curves) showed a sudden increase concomitant to the decrease in AFD fluorescence intensity (corresponding lower three curves) due to endosomal rupture and AFD dye release. (b) Fluorescence microscopy image overlays of the CysATTO633 (magenta) and fluid phase marker AFD (green) signal at activation of the photosensitizer and (c) 4 min later. The cell nucleus is indicated with the large white circle. Scale bar: 10 µm.

and is used as a label for endosomes [45]. Along with AFD, we incubated the cells with CMS-CysATTO633$_{core}$-NH$_{2shell}$ nanoparticles and the photosensitizer. After 18-24 h of incubation, the cells were examined by wide-field fluorescence microscopy.

As a result, we found all CMS nanoparticles that exhibit typical intracellular motion to be co-localized with AFD. This indicates successful internalization of the CMS nanoparticles into endosomes. The AFD fluorescence intensity of the endosomes varied depending on the amount of internalized AFD. Excitation of the photosensitizer was achieved by illumination of the sample with 405 nm laser for 1 min. This resulted in deceleration of endosomal motion until arrest, as reported previously [30]. Depending on the amount of photosensitizer incorporated in the endosomal membrane, the endosomes were ruptured within 1-4 min after 405 nm illumination. Endosomal rupture lead to a spontaneous release of AFD into the cytoplasm as indicated by a sudden drop in endosomal AFD fluorescence.

Concomitant with endosomal rupture and AFD release, the fluorescence intensity of the CMS-CysATTO633$_{core}$-NH$_{2shell}$ nanoparticles increased due to the dequenching effect, as described above and presented in Figure 8.3a. Directly after photosensitizer activation the endosomes still show predominantly AFD fluorescence (see Figure 8.6b depicted in green). Strikingly, only 4 min later the same endosomes show only CysATTO633 fluorescence (Figure 8.6c depicted in magenta). Please note that the diffuse magenta fluorescence within the nucleus area (big, white circle) is due to out of focus particle fluorescence. With a size of 10 kDa, AFD can diffuse almost freely after endosomal release, and is dispersed within the cytosol [252]. In contrast, due to their large size and impaired

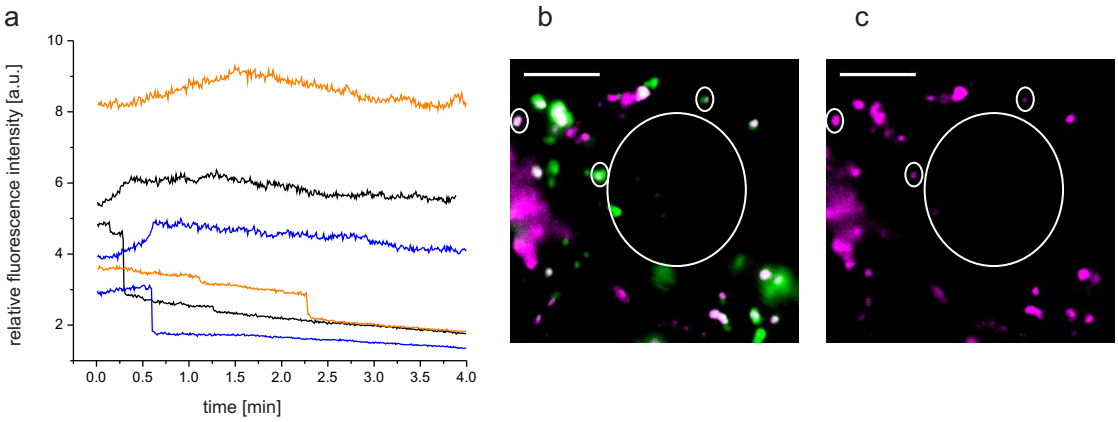

Figure 8.7: Photoinduced endosomal release of CMS-ATTO633$_{core}$-NH$_{2shell}$ and fluid phase marker AFD inside living HuH7 cells monitored by wide-field fluorescence microscopy. (a) Intensity plot of three exemplary tracked endosomes (highlighted by small circles in b and c) over time. The fluorescence intensity of ATTO633 (upper three curves) showed no or only slight increase concomitant to the decrease in AFD fluorescence intensity (corresponding lower three curves) due to endosomal rupture and AFD dye release. (b) Fluorescence microscopy image overlays of the ATTO633 (magenta) and fluid phase marker AFD (green) signal at activation of the photosensitizer and (c) 4 min later. The cell nucleus is indicated with the large white circle. Scale bar: 10 µm.

motion in the crowded cell interior, the nanoparticles remain at their location.

As a control measurement, noncleavable CMS-ATTO633$_{core}$-NH$_{2shell}$ nanoparticles without cysteine linker were incubated with AFD and the photosensitizer for 12-24 hours. The internalized nanoparticles showed co-localization with AFD until endosomal rupture. At endosomal rupture, the relative fluorescence intensity of AFD showed a sudden drop, whereas the ATTO633 fluorescence remained largely constant with a slight intensity increase by a factor of 1.25 (Figure 8.7a). This increase might be due to a small amount of unreacted dye inside the mesopores, which is released from the endosome after disruption of the endosomal membrane. The disruption of the endosomal membrane and release of AFD occurred within 4 min, and the CMS-ATTO633$_{core}$-NH$_{2shell}$ nanoparticle fluorescence remained at the former endosomal regions (Figure 8.7c).

8.5 Summary

In this chapter, we presented mechanistic insights into disulfide-based drug delivery from CMS nanoparticles. After particle synthesis, *in vitro* single-particle measurements of the nanoparticles on cover glass showed that disulfide-bound CysATTO633 is released from CMS nanoparticles in 10 mM GSH. Evaluation of the particle's fluorescence intensity revealed that the dye release is accompanied by a dequenching of the ATTO633 fluorescence. We therefore show, for the first time, that linkage of ATTO633 at high concentration in the pores of silica nanoparticles results in quenching of the ATTO633 fluorescence. This unexpected effect permits a sensitive readout for successful dye release. Although the particles were shown to be functional and to release their cargo upon addition of a

reducing agent, disulfide-based CysATTO633 release into HuH7 cells was not observed even after up to 49 h incubation of CMS-CysATTO633$_{\text{core}}$-ATTO488$_{\text{shell}}$ nanoparticles with the cells. Inefficient endosomal escape of the nanoparticles is a bottleneck for molecular delivery into the cytoplasm.
To overcome the endosomal barrier, we used the photosensitizer TPPS$_{2a}$. Upon activation of the photosensitizer, CMS-CysATTO633$_{\text{core}}$ nanoparticles successfully released disulfide-bound CysATTO633 into the cytoplasm, however the resolution of our measurement setup does not allow conclusions on the locus of reductive cleavage (endosome or cytoplasm). Our measurements confirm that endosomal escape is the main bottleneck for disulfide-based drug delivery. In case of noncleavable CMS-ATTO633$_{\text{core}}$ nanoparticles without cysteine linker, release of ATTO633 was not observed after endosomal rupture.
The proposed drug delivery system allows us to control the time of the endosomal rupture by use of the 405 nm laser. However, TPPS$_{2a}$ shows a high toxicity to the cells, as highly reactive oxygen species are produced where the photosensitizer is present. For further studies, we want to achieve spatial control on the endosomal escape by covalently particle-bound photosensitizer. Using this particle, we plan to limit singlet oxygen production and endosomal rupture only to the endosomes containing photosensitizer-equipped nanoparticles (see Chapter 9).

9 Cascaded photoinduced drug delivery from mutifunctional PpIX-mesoporous silica

In the previous chapter, we reported on an approach using reductive cleavage of disulfide-bridged compounds bound to the pore walls of mesoporous silica nanoparticles. We showed that endosomal escape represents a bottleneck for this approach. Photochemical internalization (PCI) of a photosensitizer (PS) that induces endosomal escape by creating singlet oxygen has been proven to be powerful to overcome this barrier (see Chapter 8). The PS, the porphyrin derivative $TPPS_{2a}$, is incubated with the cells. It inserts into the plasma membrane and, after endocytosis, locates in the membrane of all endocytic vesicles. Therefore, all PS containing vesicles are subject to photoactivation upon irradiation and the spatial control on endosomal escape and the induced phototoxicity is limited. To obtain spatial control on the photoactivity, association of the PS with the nanoparticles is desirable.

In current literature, different groups have applied PS associated with mesoporous silica for other purposes than PCI, such as photodynamic therapy or two-photon imaging [166, 253–255]. In addition, there are initial approaches to combine PS with mesoporous silica as drug carrier. However, in these studies, the PS is not or not completely bound to the particles [256, 257]. This can lead to uncontrolled leaching of the compounds and highly toxic effects on the cells [30]. To achieve a more precise, "surgical" function of PS-equipped nanodevices and to minimize their toxicity on cells, it is desirable to bind the PS directly to the surface of the mesoporous particles.

Therefore, we report how multifunctional core-shell colloidal mesoporous silica nanoparticles combined with covalently surface-linked protoporphyrin IX (PpIX) as an on-board photosensitizer show localized photoactivity along with controlled drug release. PpIX is a photosensitizer naturally occurring in many cell types. The iron(II) complex of PpIX, called heme, is needed for binding to different proteins to form hemoproteins such as hemoglobin [258]. For photochemical internalization, PpIX in solution is not useful due to its low water solubility (around 1 µg/mL) [259]. The low solubility can be overcome by delivery of PpIX into cells by a nanoparticle drug carrier. Once inside the cell, PpIX can be effectively excited in its Soret band at around 410 nm. This excitation initiates a cascade in which energy is transferred to molecular oxygen that oxidizes amino acids, unsaturated fatty acids, cholesterol and various cellular compartments enabling endosomal escape [80].

In this chapter, the synthesis of the CMS with covalently surface-linked PpIX and the applied particle designs will be presented briefly. Afterwards live-cell imaging studies of CMS-PpIX for disulfide-based drug delivery similar to the studies presented in Chapter 8 will be shown. To improve the readout signal for successful drug delivery, we exchanged disulfide-based drug loading

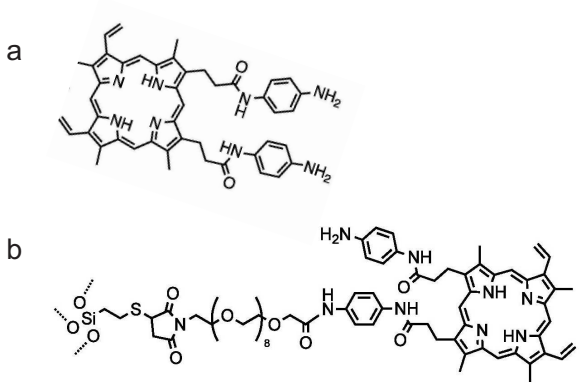

Figure 9.1: PpIX attachment to CMS nanoparticles. Attachment of amino-terminated PpIX (PpIX-NH_2) (a) to the PEGylated surface of CMS, leading to the sample CMS-$PpIX_{shell}$ (b).

towards adsorption of "model drugs". To seal the pores after drug loading, the particles were further equipped with a SLB. The activity of these SLB-coated CMS-PpIX nanodevices for photochemical release was examined with regard to the release efficiency by wide-field microscopy on a single cell level. In addition, successful drug release of "model drugs" of varying size was shown by spinning disk confocal microscopy. The results give insight into the characteristics of this newly developed drug delivery system. The project was performed in collaboration with Dr. Axel Schlossbauer, Dr. Valentina Cauda and Alexandra Schmidt from the group of Prof. Thomas Bein; Dr. Hanna Engelke from the group of Prof. Joachim Rädler and with Dr. Kourosh Zolghadr and Dr. Ulrich Rothbauer from the group of Prof. Heinrich Leonhardt (all LMU Munich). Main parts of this chapter are derived from a manuscript submitted for publication [14].

9.1 Synthesis of CMS-NH_{2core}-$PpIX_{shell}$

CMS nanoparticles with covalently surface-linked PpIX have been developed by Dr. Axel Schlossbauer and have been synthesized for our experiments by him, Dr. Valentina Cauda and Alexandra Schmidt from the group of Prof. Thomas Bein (LMU Munich).
In brief, the recently developed sequential co-condensation process [9, 260] was used to generate core-shell bifunctionalized colloidal mesoporous silica, exhibiting aminopropyl-groups on the inner pore walls and 3-mercaptopropyl on the particles' outer surface (sample CMS-NH_{2core}-SH_{shell}). For the synthesis, a mixture of tetraethylorthosilicate (TEOS), 3-aminopropyl triethoxysilane (APTES), phenyltriethoxysilane (PhTES), cetyltrimethylammonium chloride (CTAC) and triethanolamine (TEA) was stirred for hydrolysis of the silanes. PhTES was used as an additive to improve the structured co-condensation with APTES in the synthesis. 30 minutes after seed generation, a thin shell of silica was generated on the surface by adding four equal portions of TEOS to the synthesis (each with 2.5% of the total Si content of the synthesis). The outer shell of thiols was grown after an additional aging time of 30 minutes. To this end, a mixture of TEOS and 3-mercaptopropyltriethoxysilane

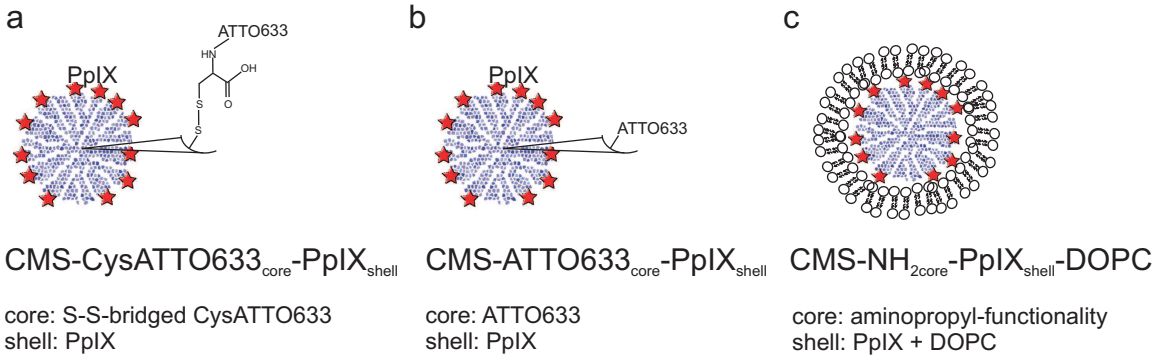

Figure 9.2: CMS samples for PpIX based drug delivery (a) CMS-CysATTO633$_{\text{core}}$-PpIX$_{\text{shell}}$ disulfide-bridged cysteinATTO633 in the particle's core and covalently surface linked PpIX (represented by red stars). (b) CMS-ATTO633$_{\text{core}}$-PpIX$_{\text{shell}}$ with non-cleavable ATTO633 in the particle's core and surface linked PpIX (red stars) (c) CMS-NH$_{2\text{core}}$-PpIX$_{\text{shell}}$-DOPC is equipped with a DOPC lipid bilayer.

(MPTES) was added (each silane amount was 1% of the total Si content of the synthesis). The resulting particles have sizes of around 80 nm and a pore diameter of around 4 nm. The outer surface of the particles was further functionalized with a short bifunctional PEG(8) linker. In order to provide an amino-terminated porphyrin derivative for subsequent attachment to the particle's PEGylated surface, protoporphyrin-IX-bis(phenyleneaminoamide) (PpIX-NH$_2$) was synthesized (see Figure 9.1a), following a modified procedure from the literature [261]. The obtained PpIX-NH$_2$ can then be attached to the particle via amidation, leading to CMS-NH$_{2\text{core}}$-PpIX$_{\text{shell}}$ nanoparticles (see Figure 9.1b). Synthesis success was monitored by dynamic light scattering, nitrogen sorption measurements, ESI mass spectroscopy as well as IR and fluorescence spectroscopy.
Different particle designs can be achieved (see Figure 9.2). For disulfide-based drug delivery, the aforementioned synthesis has been slightly modified. After CMS PEGylation, the inner amino-functional groups were reacted with mercaptopropionic acid to obtain thiol-functional groups. The core was activated with 2-2'-dithiopyridine (DTP), followed by reaction with ATTO633-labeled cystein. This resulted in disulfide-bridged, ATTO633-labeled cysteine attached to the inner pore walls of the particle core. In the last step, PpIX was covalently surface linked to obtain CMS-CysATTO633$_{\text{core}}$-PpIX$_{\text{shell}}$ (see Figure 9.2a). In addition, a control sample without cleavable disulfide-linker CMS-ATTO633$_{\text{core}}$-PpIX$_{\text{shell}}$ (see Figure 9.2b) has been synthesized.
In addition to the samples for disulfide-based drug delivery, CMS nanoparticles have been synthesized for adsorptive cargo loading and release. To achieve this, CMS-NH$_{2\text{core}}$-PpIX$_{\text{shell}}$ nanoparticles were loaded with drugs and sealed by a SLB to prevent premature cargo release. The sample CMS-NH$_{2\text{core}}$-PpIX$_{\text{shell}}$-DOPC was prepared for this purpose (see Figure 9.2c).

9.2 PpIX-induced disulfide-based drug delivery from CMS

To demonstrate the effectivity of the CMS nanoparticles with covalently surface-linked PpIX for PCI, disulfide-based drug delivery from CMS is a well-suited strategy. The strategy is based on the

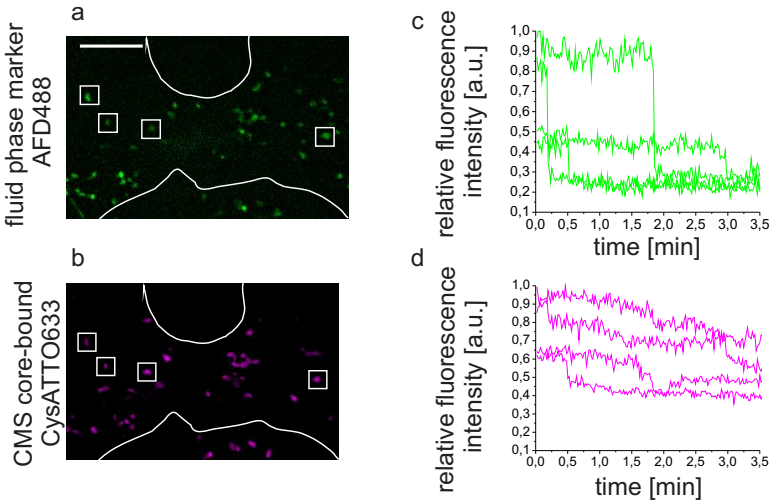

Figure 9.3: Photoinduced endosomal release of CMS-CysATTO633$_{\mathbf{core}}$-PpIX$_{\mathbf{shell}}$ and fluid phase marker AFD inside living HuH7 cells monitored by wide-field fluorescence microscopy. (a and b) Fluorescence microscopy images of the fluid phase marker AFD (green) and ATTO633 (magenta) signal directly after activation of the photosensitizer. (c and d) Intensity plot of four exemplarily tracked endosomes (highlighted by white boxes in a and b) over time. As expected, the fluorescence intensity of AFD (c) showed a sudden decrease due to endosomal rupture. The fluorescence of core-bound CysATTO633 drops concomitantly (d). The cell nucleus is indicated by a white circle and the outer white line represents the cell border. Scale bar: 10 µm.

reductive cleavage of disulfide bridges in the reductive milieu of the cytoplasm. In our previously described study (see Chapter 8), we used CMS for disulfide-based drug delivery in combination with the fluid-phase photosensitizer TPPS$_{2a}$ for endosomal escape. In the following experiment, we used CMS-CysATTO633$_{\text{core}}$-PpIX$_{\text{shell}}$ with covalently surface bound PpIX. For the experiment, living HuH7 cells were incubated with the nanoparticles and the fluid phase marker Alexa Fluor 488 Dextran (AFD), a marker for endocytosis [45] for 12-24 hours. The incubation time of 12-24 hours was chosen to ensure sufficient uptake of the particles into the cells and minimize effects of cell surface-associated nanoparticles. After incubation, the cells were exposed to 405 nm laser light with a power of 0.15 mW for up to 15 s on a wide-field microscope. Subsequently, movies of the photoactivated cells were taken in alternating illumination with 488 and 633 nm laser light and a frame rate of 1.7 s^{-1} exciting AFD and disulfide-bound CysATTO633, respectively. The fluorescence images were recorded on two separate cameras. The first fluorescence images of the representative movies recorded by the two cameras are shown in Figure 9.3. The images of AFD-stained endosomes (Figure 9.3a, depicted in green) and core disulfide-bound CysATTO633 (Figure 9.3b, depicted in magenta) co-localize to a high extend confirming intracellular localization of the particles. To determine the kinetics of endosomal release, particle-containing endosomes were tracked in every frame of the movie sequence in both colors. A rolling ball background filter of 5 pixels was used to remove inhomogeneous background fluorescence in both channels. The fluorescence intensities were extracted, normalized and plotted versus time. The AFD and CysATTO633 intensity plots

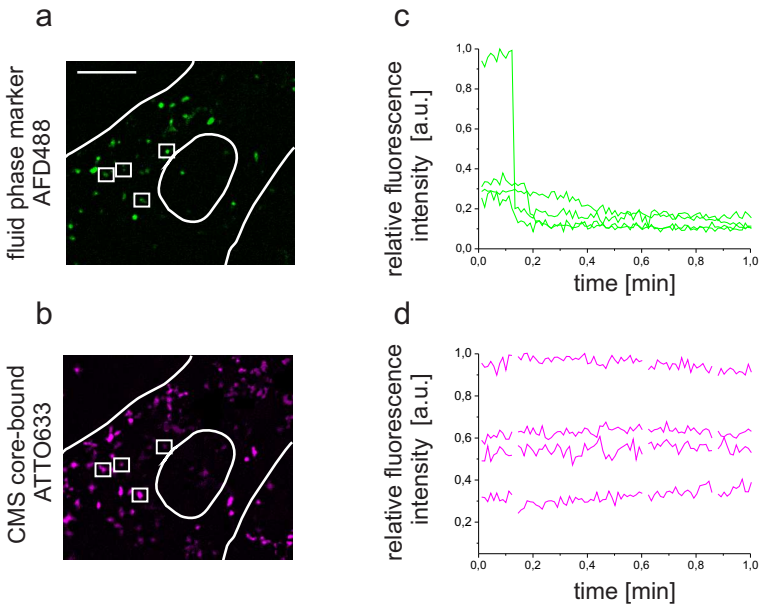

Figure 9.4: Photoinduced endosomal release of CMS-ATTO633$_{\text{core}}$-PpIX$_{\text{shell}}$ and fluid phase marker AFD inside living HuH7 cells monitored by wide-field fluorescence microscopy. (a and b) Fluorescence microscopy images of the fluid phase marker AFD (green) and ATTO633 (magenta) signal directly after photosensitizer activation. (c and d) Intensity plot of four exemplarily tracked endosomes (highlighted by white boxes in a and b) over time. The fluorescence intensity of AFD (c) showed a sudden decrease due to endosomal rupture while the fluorescence of covalently core-bound dye ATTO633 remains constant (d). The cell nucleus is indicated by a white circle and the outer white line represents the cell border. Scale bar: 10 µm.

of four exemplary tracked endosomes are shown in Figure 9.3c and d. In case of endosomal AFD fluorescence, destruction of the endosomal membrane is indicated by a sudden drop in fluorescence (see Figure 9.3c, green curves) within 3 min post photoactivation. A similar effect is observed for the CysATTO633 fluorescence of the nanoparticles in the endosomes. Concomitantly to the sudden drop in AFD fluorescence, the same endosome shows a drop in CysATTO633 fluorescence (see Figure 9.3). This result shows, that CysATTO633 is probably released from the endosome. Furthermore, the drop in fluorescence intensity shows that in this experiment there is no self-quenching of ATTO633 and therefore a smaller amount of ATTO633 in bound to the CMS pores. However, photochemical effects of the produced reactive oxygen species on the fluorescence of CysATTO633 have to be excluded.

To evaluate this, CMS nanoparticles with non-cleavable pore-bound ATTO633 (CMS-ATTO633$_{\text{core}}$-PpIX$_{\text{shell}}$) have been incubated with the cells together with AFD. After incubation, the cells were activated by 405 nm illumination for 15 s. The movie was taken in alternating illumination with a frame rate of 4.6 s^{-1}. The first images of the movie sequence together with the fluorescence intensity plots over time for both AFD and ATTO633 are shown in Figure 9.4. Endosomes for evaluation in the intensity plots have been marked by boxes in Figure 9.4a and b. Endosomal rupture is shown

by stepwise decrease in AFD fluorescence (Figure 9.4c, green curves). However, the fluorescence intensity of pore-bound ATTO633 remains constant (Figure 9.4d, magenta curves). This indicates that photochemically generated reactive oxygen species seem to have no effect on the fluorescence of ATTO633 bound to the CMS core. Hence, the drop in fluorescence of the cleavable and pore-bound CysATTO633 can be fully attributed to its release into the cytoplasm.
To summarize, we showed that CMS nanoparticles with covalently surface-linked PpIX are effective in photochemical endosomal escape. However, we want to study the release mechanism in more detail and extend PpIX-induced drug delivery to model drugs that can not be delivered in a disulfide-based manner. Therefore, we loaded the nanoparticles by adsorption of model drugs and sealed the nanoparticles by a SLB to prevent premature drug release.

9.3 PpIX-induced release mechanism of chromobodies from CMS

To show the functionality of the nanodevice for photoinduced endosomal release mechanistically, we loaded CMS-NH_{2core}-$PpIX_{shell}$ nanoparticles with chromobodies as model drugs and investigated them with wide-field fluorescence microscopy in living cells. Chromobodies are epitope-recognizing fragments of heavy-chain antibodies of Camelidae sp. fused to fluorescent proteins or dyes [262–264]. ATTO594-labeled chromobodies were provided by Dr. Ulrich Rothbauer and Dr. Kourosh Zolghadr from the group of Prof. Heinrich Leonhardt (LMU). The loaded and SLB-sealed particles were incubated with living HuH7 cells together with the fluid phase marker AFD. Both CMS with supported lipid bilayer [12] and AFD [45] are known to be internalized into the cell by endocytosis. After 12-24 hours of incubation, the cells were exposed to 405 nm laser light for 1 min. After photoactivation of the sample, a movie of the cell was taken in alternating illumination with 488 and 633 nm laser light and a frame rate of $3.4\,s^{-1}$ exciting AFD and chromobodies labeled with ATTO594, respectively. The first image of a representative movie sequence is displayed in Figure 9.5. Co-localization of AFD-stained endosomes (Figure 9.5a) and chromobody-loaded CMS-NH_{2core}-$PpIX_{shell}$DOPC nanoparticles (Figure 9.5b) confirmed successful intracellular localization of the particles. To obtain kinetic information on the burst of the endosomes and the release mechanism on the level of a single endosome, the fluorescence intensities of endosomes (marked with white boxes and a circle in Figures 9.5a and b) were recorded and plotted versus time. Upon destruction of the endosomal membrane, a spontaneous release and dilution of AFD into the cytoplasm was indicated by a sudden drop in endosomal AFD fluorescence (Figure 9.5c, green curves). Depending on the amount of internalized photosensitizer (PpIX), the endosomes ruptured at different timepoints within 1 min after photoactivation. No change in fluorescence intensity was recorded for the endosome that did not contain chromobody-loaded CMS-NH_{2core}-$PpIX_{shell}$DOPC nanoparticles (Figure 9.5a, white circle and 9.5c, black curve). Concomitantly to the sudden drop in endosomal AFD fluorescence caused by endosomal rupture, the chromobody fluorescence in the indicated regions dropped as well (Figure 9.5d, magenta curves). Summarizing, in the first step of the cascaded delivery mechanism directly after photoactivation, the supported lipid bilayer is disintegrated by singlet oxygen. This leads to the escape of chromobodies from CMS nanoparticles. However, they cannot escape

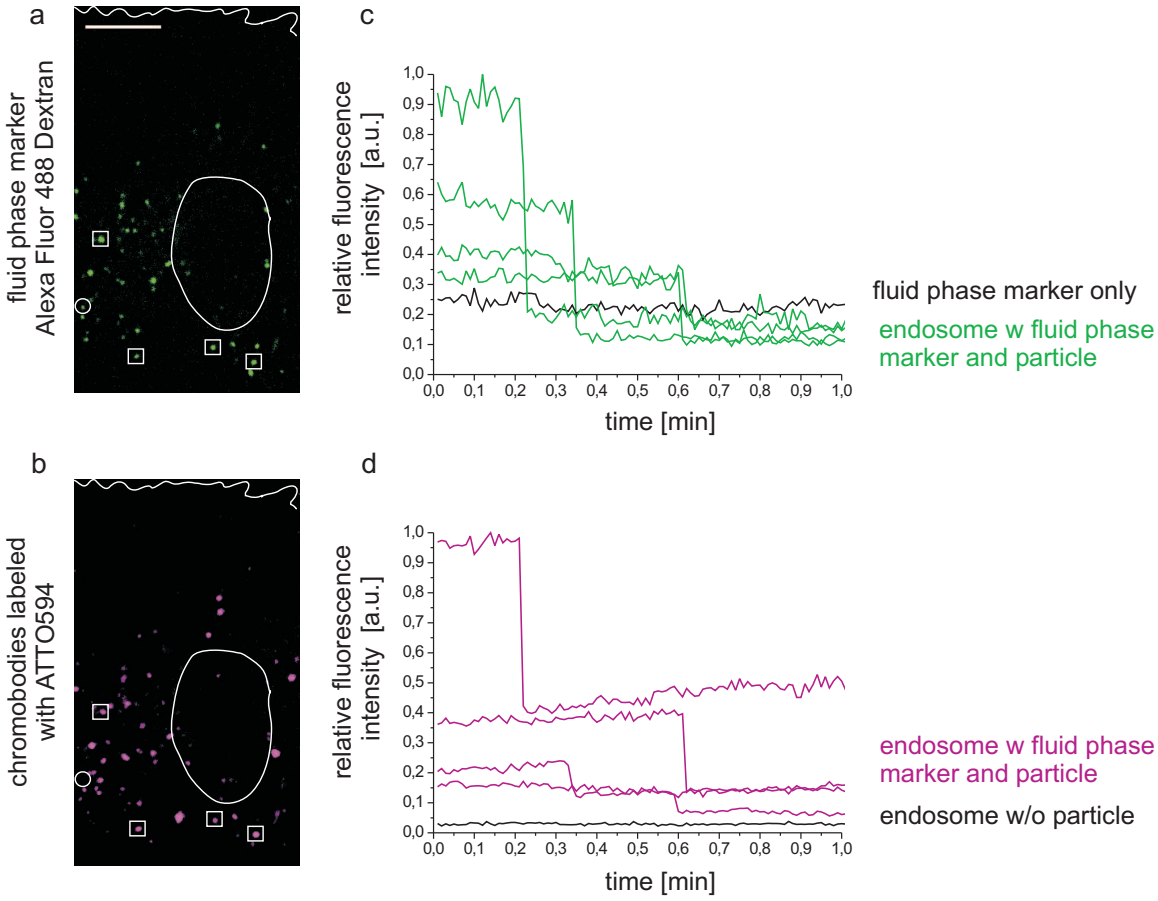

Figure 9.5: Photoinduced endosomal release of chromobody-loaded CMS-NH_{2core}-$PpIX_{shell}$-DOPC and fluid phase marker AFD. The cells were exposed overnight to CMS-NH_{2core}-$PpIX_{shell}$-DOPC loaded with ATTO549-labeled chromobodies. (a,b) Fluorescence wide-field microscopy images of the chromobody (magenta) and fluid phase marker AFD signal (green) directly after activation of the photosensitizer. (c,d) Intensity plot of four exemplarily tracked endosomes (highlighted by white boxes and a white small circle in a and b) over time. A rolling ball background filter of 5 pixels was used to remove inhomogeneous background fluorescence due to released AFD and chromobodies in both channels [217]. In case of particle-filled endosomes (white boxes in a), the fluorescence intensity of AFD (green curves in c) showed a sudden decrease concomitant to the decrease in chromobody fluorescence intensity (magenta curves in d) in the same region of interest due to endosomal membrane rupture and distribution of AFD and chromobodies into the cytosol. No decrease in AFD fluorescence (black curve in c) was detected for the endosome filled only with fluid phase marker (white circle in a). The cell nucleus is indicated by a big white circle and the outer white line represents the cell border. Scale bar: 10 µm.

from the endosome and no change of the endosomes' chromobody fluorescence can be recorded. In a second step, the endosomal membrane ruptures, indicated by fluid phase marker and concomitant chromobody release. In addition, we observed that as a result of the 405 nm illumination of the cell, intracellular motion of particle-filled endosomes (highlighted in white boxes in Figure 3a,b) slowed down, as previously described [13, 30]. Strikingly, endosomes without photosensitizer (e.g. the endosome highlighted with a white circle in Figure 9.5a,b) did not show such an effect. This indicates that only endosomes containing the particle-bound photosensitizer are affected by the toxicity of singlet oxygen on the microtubule motor proteins. In contrast to standard fluid-phase photosensitizers such as $AlPcS_{2a}$ [265] and $TPPS_{2a}$ [266], the phototoxic effect can be locally restricted to endosomes that are loaded with nanoparticles and therefore contain the covalently-bound photosensitizer. This important finding shows that the covalently-bound photosensitizer enables "surgical" endosomal release without the global cell toxicity exerted by the common photosensitizers.

9.4 Cellular effects of PpIX-induced drug release

To generalize the above approach and to verify the release and biological effects of loaded substances on the cells, we charged two other membrane-impermeable model drugs into the pores of the CMS-NH_{2core}-$PpIX_{shell}$. The first model drug was propidium iodide (PI), a well-known DNA and RNA intercalator with a molecular weight of 660 Da. In addition, Alexa Fluor 647-labeled phalloidin was applied. Phalloidin is a bicyclic peptide with a molecular weight of 1950 Da that binds to filamentous actin. The cellular protein actin forms filaments that - among other functions - contributes to the mechanical support of the cells [267]. As a third model drug, we used chromobodies with a molecular weight of 13.738 Da. The chromobodies were labeled with Chromeo642 and were designed to bind to GFP. In all cases, the particles were loaded with the corresponding model drug, sealed with a lipid bilayer and incubated with the cells for 12-24 hours. Afterwards, the cells were exposed to mild photoactivation conditions on a 405 nm LED plate for 5-20 min and imaged on a spinning disk confocal microscope. As a control, we used cells that were incubated under the same conditions, but were not photoactivated prior to imaging. The results obtained with the three model drugs are shown in Figure 9.6. Superposition of a transmitted light image with the PI fluorescence image (Figure 9.6a, left panel) as well as the PI fluorescence channel alone (Figure 9.6a, right panel) are displayed. Release of PI can be visualized by diffuse magenta fluorescence in the nuclei (marked with white circles in Figure 9.6a). Especially the nucleoli, highly contrasted structures in transmitted light images, were stained by released PI. This can be attributed to the fact that the nucleoli, as functional entities for the synthesis of ribosomal RNA, offer multiple intercalation sites for PI [268]. In case of phalloidin, an overlay of the peptide's fluorescent signal (shown in magenta) with stably actin-GFP expressing HuH7 cells (shown in green) reveals co-localization of both colors (see boxes in Figure 9.6b). This indicates successful release and binding of phalloidin to actin fibers. As a third proof of principle, we observed successful chromobody release and GFP binding to the tubulin filaments of stably expressing tubulin-GFP HuH7 cells (examples of fibers are marked with boxes in Figure 9.6c). In all three cases, non-activated control cells show only fluorescence from endosomally

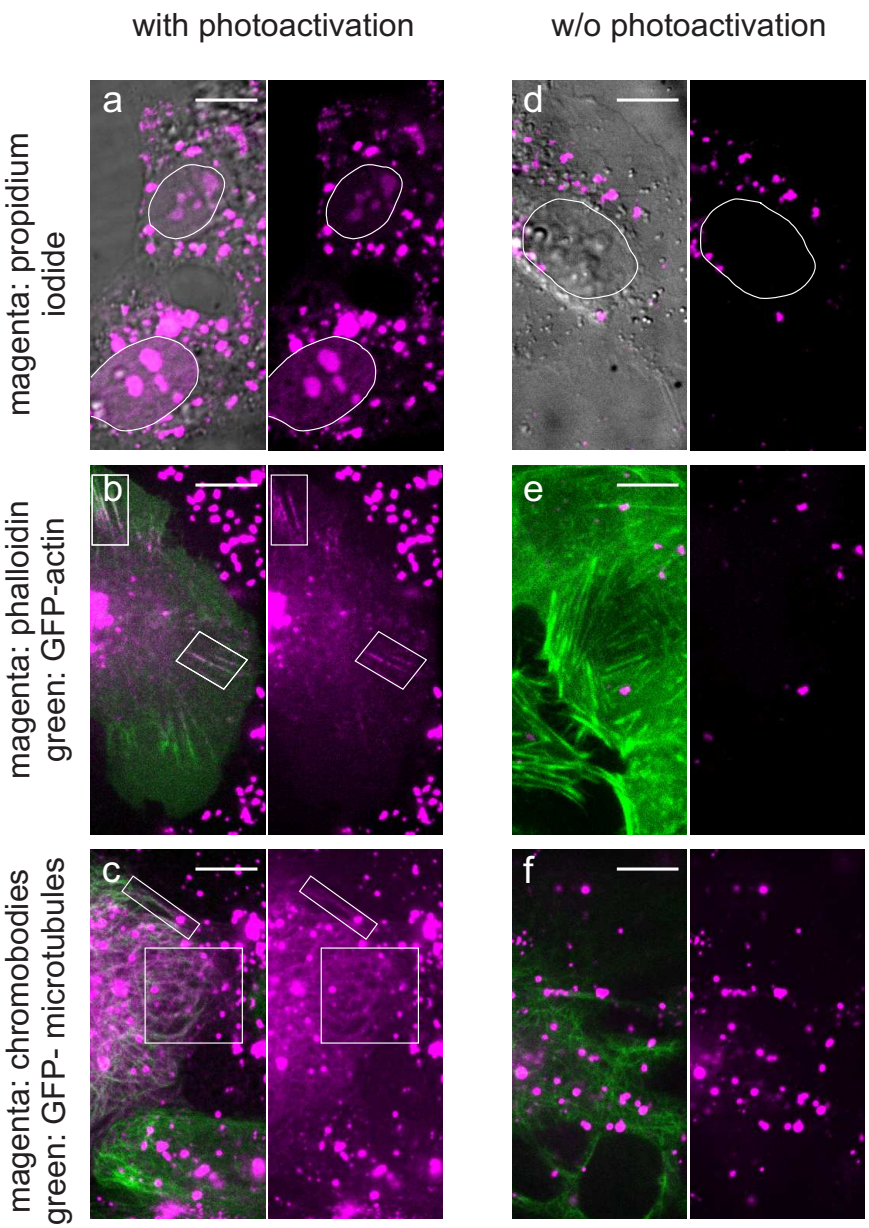

Figure 9.6: Confocal microscopy of living HuH7 cells exposed to CMS-NH_{2core}-$PpIX_{shell}$-DOPC nanoparticles loaded with model drugs. HuH7 cells were exposed to CMS-NH_{2core}-$PpIX_{shell}$-DOPC nanoparticles loaded with PI (a,d), phalloidin (b,e) and chromobodies (c,f). (a) Superposition of the transmitted light image of HuH7 cells with the PI fluorescence (left panel) and the PI fluorescence alone (right panel). Propidium iodide stains the nucleus of the cell. (b) Alexa Fluor 647-labeled phalloidin fluorescence (shown in magenta) and stably actin-GFP expressing HuH7 cell (shown in green on the left panel) and the phalloidin fluorescence alone (shown in magenta in the right panel). (c) Chromeo642-labeled chromobodies (magenta) released from the particles stain the microtubules of stably microtubule-GFP expressing HuH7 cells (green, in the left panel). The chromobody channel is displayed in the right panel. (d-f) In case of the non-photoactivated samples, no labeled cell structure was observed. Scale bar: 10 µm.

entrapped nanoparticles (Figure 9.6d-f). We have thus shown that the model drugs were released from the nanoparticles in their intact form upon photoactivation, and that they were able to bind to their respective cellular target structures.

9.5 Summary

In this chapter, we presented the use of CMS nanoparticles with covalently surface-linked PpIX as novel photoinduced drug delivery platform. The nanoparticles were successfully applied for PCI in living cells. In a first set of experiments, we showed disulfide-based CysATTO633 delivery from CMS. In order to gain more mechanistic insight into the drug delivery with PS-equipped nanoparticles, chromobodies were adsorbed into the pores and a SLB was used as a seal. The chromobodies were released in a two-step cascaded manner. In the first step, the supported lipid bilayer is disintegrated by singlet oxygen and in a second step, the endosomal membrane ruptures, the chromobodies can escape and bind to their target structure. In addition, other model drugs, such as propidium iodide and phalloidin were released from the nanoparticles in their intact form and were able to bind to their respective cellular target structures.
To summarize, we have presented a novel photoinduced drug delivery platform consisting of multifunctional core-shell colloidal mesoporous silica nanoparticles with surface-bound photosensitizer PpIX. This nanodevice for drug delivery is capable of stimuli-responsive and controlled, localized endosomal escape and drug release in a two-step cascaded manner, without the global cell toxicity exerted by common photosensitizers. We expect this method to be a powerful and general approach for endosomal release, as the encapsulated drugs remain functional after photoactivation and release from the nanoparticle. In addition, our delivery platform may prove very powerful for the delivery of other membrane impermeable substances.

List of abbreviations

abbreviation	explanation
AF488	alexa fluor 488
AFD	alexa fluor dextran
α-CD	α-cyclodextrin
AOTF	acousto-optical tunable filter
APTES	(3-aminopropyl)-triethoxysilane
ASGP-R	asialoglycoprotein receptor
ATP	adenosine triphosphate
BfR	german federal institute for risk assessment
Γ	radiative decay rate
cAMP	cyclic adenosine monophosphate
CB[6]	cucurbit[6]uril
CdS	cadmium sulfide
CHO	chinese hamster ovary cells
CMS	colloidal mesoporous silica
COS-7	african green monkey kidney cells
CTAB	cetyltrimethylammonium bromide
CTAC	cetyltrimethylammonium chloride
Cys	cystein
DDAB	didodecyldimethylammonium bromide
DMEM	dulbecco's modified eagle's medium
DNA	desoxyribonucleic acid
DOPC	dioleoyl-sn-glycero-3-phosphocholine
DOPE	dioleoyl-phosphatidylethanolamine
DOTAP	dioleoyl-trimethylammonium propane
DTP	2-2'-dithiopyridine
DTT	dithiothreitol
EGF(R)	epidermal growth factor (receptor)
EPR	enhanced permeability and retention effect

abbreviation	explanation
ESF	european science foundation
FCS	fetal calve serum
FDA	food and drug administration
FITC	fluorescein isothiocyanate
GFP	green fluorescent protein
GSH	glutathion
HeLa	cervix adenocarcinoma cell line
HepaG2	human liver hepatocellular carcinoma cell line
HFF	human foreskin fibroblast
HRBC	human red blood cells
HSA	human serum protein
HuH7	human hepato cellular carcinoma cell line
IUPAC	International Union of Pure and Applied Chemistry
k_{nr}	non-radiative decay rates
LA	lactobionic acid
MDA-MB-468	human breast cancer cells
MDDC	human monocyte-derived dendritic cells
ME	2-mercaptoethanol
MS	mesoporous silica
MPTES	(3-mercaptopropyl)-triethoxysilane
MSN	mesoporous silica nanoparticles
MW	molecular weight
NIH	national institutes of health
PANC-1	human pancreatic carcinoma cell line
PCI	photochemical internalization
PEG	polyethylene glycol
PEI	polyethyleneimine
PhTES	phenyltriethoxysilane
PI	propidium iodide
PL(G)A	polylactic (co-glycolic) acid
PMV	polymethacrylic acid-co-vinyl triethoxysilane
POPC	1-palmitoyl-2-oleoyl-sn-glycero-3-phosphocholine

abbreviation	explanation
PpIX	protoporphyrin IX
PS	photosensitizer
Q	quantum yield
RES	reticuloendothelial system
RGD	arginine-glycine-aspartic acid
(si)RNA	(small interfering) ribonucleic acid
ROI	region of interest
ROS	reactive oxygen species
RT	room temperature
SBF	simulated body fluid
SLB	supported lipid bilayer
SNARE	soluble N-ethylmaleimide-sensitive factor attachment protein receptor
τ_0	lifetime of a fluorophore
TEA	triethanolamine
TEOS	tetraethyl orthosilicate
TFR	transferrin receptor
$TPPS_{2a}$	disulfonated *meso*-tetraphenylporphine
WHO	world health organization
3T3	swiss albino mouse embryo fibroblast cell line

Bibliography

[1] K. de Bruin, N. Ruthardt, K. von Gersdorff, R. Bausinger, E. Wagner, M. Ogris, and C. Bräuchle. Cellular dynamics of EGF receptor-targeted synthetic viruses. *Mol Ther*, 15(7):1297–305, 2007.

[2] A. M. Sauer, K. G. de Bruin, N. Ruthardt, O. Mykhaylyk, C. Plank, and C. Bräuchle. Dynamics of magnetic lipoplexes studied by single particle tracking in living cells. *J Control Release*, 137(2):136–45, 2009.

[3] Federal Institute for Risk Assessment (BfR). Public perceptions about nanotechnology- representative survey and basic morphological-psychological study. 2008.

[4] J. D. Kingsley, H. Dou, J. Morehead, B. Rabinow, H. E. Gendelman, and C. J. Destache. Nanotechnology: a focus on nanoparticles as a drug delivery system. *J Neuroimmune Pharmacol*, 1(3):340–50, 2006.

[5] World health organization (WHO). The world health organization's fight against cancer- strategies that prevent, cure and care. *http://www.who.int/cancer/publicat/WHOCancerBrochure2007.FINALweb.pdf*, 2007.

[6] M. Liong, S. Angelos, E. Choi, K. Patel, J. F. Stoddart, and J. I. Zink. Mesostructured multifunctional nanoparticles for imaging and drug delivery. *J Mater Chem*, 19:6251–6257, 2009.

[7] M. Liong, J. Lu, M. Kovochich, T. Xia, S. G. Ruehm, A. E. Nel, F. Tamanoi, and J. I. Zink. Multifunctional inorganic nanoparticles for imaging, targeting, and drug delivery. *ACS Nano*, 2(5):889–96, 2008.

[8] J. Lu, M. Liong, J. I. Zink, and F. Tamanoi. Mesoporous silica nanoparticles as a delivery system for hydrophobic anticancer drugs. *Small*, 3(8):1341–6, 2007.

[9] V. Cauda, A. Schlossbauer, J. Kecht, A. Zürner, and T. Bein. Multiple core-shell functionalized colloidal mesoporous silica nanoparticles. *J Am Chem Soc*, 131(32):11361–70, 2009.

[10] K. Möller, J. Kobler, and T. Bein. Colloidal suspensions of nanometer-sized mesoporous silica. *Adv Funct Mater*, 17(4):605–612, 2007.

[11] M. L. Immordino, F. Dosio, and L. Cattel. Stealth liposomes: review of the basic science, rationale, and clinical applications, existing and potential. *Int J Nanomedicine*, 1(3):297–315, 2006.

[12] V. Cauda, H. Engelke, A. Sauer, D. Arcizet, C. Bräuchle, J. Rädler, and T. Bein. Colchicine-loaded lipid bilayer-coated 50 nm mesoporous nanoparticles efficiently induce microtubule depolymerization upon cell uptake. *Nano Lett*, 10(7):2484–92, 2010.

[13] A. M. Sauer, A. Schlossbauer, N. Ruthardt, V. Cauda, T. Bein, and C. Bräuchle. Role of endosomal escape for disulfide-based drug delivery from colloidal mesoporous silica evaluated by live-cell imaging. *Nano Lett*, 10(9):3684–91, 2010.

[14] A. Schlossbauer, A.M. Sauer, V. Cauda, A. Schmidt, H. Engelke, U. Rothbauer, K. Zolghadr, H. Leonhardt, C. Bräuchle, and T. Bein. Cascaded photoinduced drug delivery to cells from multifunctional core-shell mesoporous silica. *submitted*, 2011.

[15] B. Y. Kim, J. T. Rutka, and W. C. Chan. Nanomedicine. *N Engl J Med*, 363(25):2434–43, 2010.

[16] R. Duncan. Polymer conjugates as anticancer nanomedicines. *Nat Rev Cancer*, 6(9):688–701, 2006.

[17] National Institutes of Health (NIH). NIH common funds: nanomedicine. *https://commonfund.nih.gov/nanomedicine/overview.aspx*, 2011.

[18] European Science Foundation (ESF). ESF forward look on nanomedicine. *http://www.nanopharmaceuticals.org/files/nanomedicine.pdf*, 2005.

[19] W. Y. Sheng and L. Huang. Cancer immunotherapy and nanomedicine. *Pharm Res*, 28(2):200–14, 2011.

[20] A. Shapira, Y. D. Livney, H. J. Broxterman, and Y. G. Assaraf. Nanomedicine for targeted cancer therapy: Towards the overcoming of drug resistance. *Drug Resist Updat*, 14(3):150–63, 2011.

[21] M. Ferrari. Cancer nanotechnology: opportunities and challenges. *Nat Rev Cancer*, 5(3):161–71, 2005.

[22] C. K. Kim and S. J. Lim. Recent progress in drug delivery systems for anticancer agents. *Arch Pharm Res*, 25(3):229–39, 2002.

[23] A. H. Faraji and P. Wipf. Nanoparticles in cellular drug delivery. *Bioorg Med Chem*, 17(8):2950–62, 2009.

[24] K. Cho, X. Wang, S. Nie, Z. G. Chen, and D. M. Shin. Therapeutic nanoparticles for drug delivery in cancer. *Clin Cancer Res*, 14(5):1310–6, 2008.

[25] V. Russ and E. Wagner. Cell and tissue targeting of nucleic acids for cancer gene therapy. *Pharm Res*, 24(6):1047–57, 2007.

[26] W. Li and Jr. Szoka, F. C. Lipid-based nanoparticles for nucleic acid delivery. *Pharm Res*, 24(3):438–49, 2007.

[27] R. A. Petros and J. M. Desimone. Strategies in the design of nanoparticles for therapeutic applications. *Nat Rev Drug Discov*, 9(8):615–27, 2010.

[28] T. M. Allen and P. R. Cullis. Drug delivery systems: entering the mainstream. *Science*, 303(5665):1818–22, 2004.

[29] R. Bausinger, K. von Gersdorff, K. Braeckmans, M. Ogris, E. Wagner, C. Bräuchle, and A. Zumbusch. The transport of nanosized gene carriers unraveled by live-cell imaging. *Angew Chem Int Ed*, 45(10):1568–72, 2006.

[30] K. G. de Bruin, C. Fella, M. Ogris, E. Wagner, N. Ruthardt, and C. Bräuchle. Dynamics of photoinduced endosomal release of polyplexes. *J Control Release*, 2008.

[31] D. Peer, J. M. Karp, S. Hong, O. C. Farokhzad, R. Margalit, and R. Langer. Nanocarriers as an emerging platform for cancer therapy. *Nat Nanotechnol*, 2(12):751–60, 2007.

[32] F. Danhier, O. Feron, and V. Preat. To exploit the tumor microenvironment: Passive and active tumor targeting of nanocarriers for anti-cancer drug delivery. *J Control Release*, 148(2):135–46, 2010.

[33] D. Shenoy, S. Little, R. Langer, and M. Amiji. Poly(ethylene oxide)-modified poly(beta-amino ester) nanoparticles as a pH-sensitive system for tumor-targeted delivery of hydrophobic drugs: part 2. in vivo distribution and tumor localization studies. *Pharm Res*, 22(12):2107–14, 2005.

[34] Y. Matsumura and H. Maeda. A new concept for macromolecular therapeutics in cancer chemotherapy: mechanism of tumoritropic accumulation of proteins and the antitumor agent smancs. *Cancer Res*, 46(12):6387–92, 1986.

[35] F. Yuan, M. Dellian, D. Fukumura, M. Leunig, D. A. Berk, V. P. Torchilin, and R. K. Jain. Vascular permeability in a human tumor xenograft: molecular size dependence and cutoff size. *Cancer Res*, 55(17):3752–6, 1995.

[36] H. Maeda. The enhanced permeability and retention (EPR) effect in tumor vasculature: the key role of tumor-selective macromolecular drug targeting. *Adv Enzyme Regul*, 41:189–207, 2001.

[37] P. Carmeliet and R. K. Jain. Angiogenesis in cancer and other diseases. *Nature*, 407(6801):249–57, 2000.

[38] C. Plank. Nanomedicine: Silence the target. *Nat Nanotechnol*, 4(9):544–545, 2009.

[39] A. Philipp, M. Meyer, and E. Wagner. Extracellular targeting of synthetic therapeutic nucleic acid formulations. *Curr Gene Ther*, 8(5):324–34, 2008.

[40] E. Wagner, M. Ogris, and W. Zauner. Polylysine-based transfection systems utilizing receptor-mediated delivery. *Adv Drug Deliv Rev*, 30(1-3):97–113, 1998.

[41] I. A. Khalil, K. Kogure, H. Akita, and H. Harashima. Uptake pathways and subsequent intracellular trafficking in nonviral gene delivery. *Pharmacol Rev*, 58(1):32–45, 2006.

[42] G. Sahay, D. Y. Alakhova, and A. V. Kabanov. Endocytosis of nanomedicines. *J Control Release*, 145(3):182–195, 2010.

[43] S. D. Conner and S. L. Schmid. Regulated portals of entry into the cell. *Nature*, 422(6927):37–44, 2003.

[44] M. Amyere, M. Mettlen, P. Van Der Smissen, A. Platek, B. Payrastre, A. Veithen, and P. J. Courtoy. Origin, originality, functions, subversions and molecular signalling of macropinocytosis. *Int J Med Microbiol*, 291(6-7):487–94, 2002.

[45] R. D. Berlin and J. M. Oliver. Surface functions during mitosis. II. Quantitation of pinocytosis and kinetic characterization of the mitotic cycle with a new fluorescence technique. *J Cell Biol*, 85(3):660–71, 1980.

[46] K. A. Mislick and J. D. Baldeschwieler. Evidence for the role of proteoglycans in cation-mediated gene transfer. *Proc Natl Acad Sci U S A*, 93(22):12349–54, 1996.

[47] M. P. Murphy. Selective targeting of bioactive compounds to mitochondria. *Trends Biotechnol*, 15(8):326–30, 1997.

[48] R. A. Smith, C. M. Porteous, A. M. Gane, and M. P. Murphy. Delivery of bioactive molecules to mitochondria in vivo. *Proc Nat Acad Sci U S A*, 100(9):5407–12, 2003.

[49] H. Hillaireau and P. Couvreur. Nanocarriers' entry into the cell: relevance to drug delivery. *Cell Mol Life Sci*, 66(17):2873–96, 2009.

[50] E. Ryschich, G. Huszty, H. P. Knaebel, M. Hartel, M. W. Buchler, and J. Schmidt. Transferrin receptor is a marker of malignant phenotype in human pancreatic cancer and in neuroendocrine carcinoma of the pancreas. *Eur J Cancer*, 40(9):1418–22, 2004.

[51] S. D. Weitman, R. H. Lark, L. R. Coney, D. W. Fort, V. Frasca, Jr. Zurawski, V. R., and B. A. Kamen. Distribution of the folate receptor GP38 in normal and malignant cell lines and tissues. *Cancer Res*, 52(12):3396–401, 1992.

[52] V. Rusch, J. Mendelsohn, and E. Dmitrovsky. The epidermal growth factor receptor and its ligands as therapeutic targets in human tumors. *Cytokine Growth Factor Rev*, 7(2):133–41, 1996.

[53] L. K. Medina-Kauwe. "Alternative" endocytic mechanisms exploited by pathogens: new avenues for therapeutic delivery? *Adv Drug Deliv Rev*, 59(8):798–809, 2007.

[54] A. Pol, A. Lu, M. Pons, S. Peiró, and C. Enrich. Epidermal growth factor-mediated caveolin recruitment to early endosomes and mapk activation. role of cholesterol and actin cytoskeleton. *J Biol Chem*, 275(39):30566–72, 2000.

[55] Y. Nie, D. Schaffert, W. Rödl, M. Ogris, E. Wagner, and M. Günther. Dual-targeted polyplexes: One step towards a synthetic virus for cancer gene therapy. *J Control Release*, 152(1):127–34, 2011.

[56] R. Jahn, T. Lang, and T. C. Südhof. Membrane fusion. *Cell*, 112(4):519–33, 2003.

[57] P. L. Felgner, T. R. Gadek, M. Holm, R. Roman, H. W. Chan, M. Wenz, J. P. Northrop, G. M. Ringold, and M. Danielsen. Lipofection: a highly efficient, lipid-mediated DNA-transfection procedure. *Proc Natl Acad Sci U S A*, 84(21):7413–7, 1987.

[58] P. L. Felgner, Y. J. Tsai, L. Sukhu, C. J. Wheeler, M. Manthorpe, J. Marshall, and S. H. Cheng. Improved cationic lipid formulations for in vivo gene therapy. *Ann N Y Acad Sci*, 772:126–39, 1995.

[59] I. S. Zuhorn and D. Hoekstra. On the mechanism of cationic amphiphile-mediated transfection. to fuse or not to fuse: is that the question? *J Membr Biol*, 189(3):167–79, 2002.

[60] A. Verma, O. Uzun, Y. Hu, H. S. Han, N. Watson, S. Chen, D. J. Irvine, and F. Stellacci. Surface-structure-regulated cell-membrane penetration by monolayer-protected nanoparticles. *Nat Mater*, 7(7):588–95, 2008.

[61] M. Oren-Suissa and B. Podbilewicz. Evolution of programmed cell fusion: common mechanisms and distinct functions. *Dev Dyn*, 239(5):1515–28, 2010.

[62] K. Miyauchi, Y. Kim, O. Latinovic, V. Morozov, and G. B. Melikyan. HIV enters cells via endocytosis and dynamin-dependent fusion with endosomes. *Cell*, 137(3):433–44, 2009.

[63] G. L. Lukacs, P. Haggie, O. Seksek, D. Lechardeur, N. Freedman, and A. S. Verkman. Size-dependent DNA mobility in cytoplasm and nucleus. *J Biol Chem*, 275(3):1625–9, 2000.

[64] A. S. Silva, J. A. Yunes, R. J. Gillies, and R. A. Gatenby. The potential role of systemic buffers in reducing intratumoral extracellular pH and acid-mediated invasion. *Cancer Res*, 69(6):2677–84, 2009.

[65] G. Helmlinger, F. Yuan, M. Dellian, and R. K. Jain. Interstitial pH and pO2 gradients in solid tumors in vivo: high-resolution measurements reveal a lack of correlation. *Nat Med*, 3(2):177–82, 1997.

[66] F. A. Gallagher, M. I. Kettunen, S. E. Day, D. E. Hu, J. H. Ardenkjaer-Larsen, R. Zandt, P. R. Jensen, M. Karlsson, K. Golman, M. H. Lerche, and K. M. Brindle. Magnetic resonance imaging of pH in vivo using hyperpolarized 13C-labelled bicarbonate. *Nature*, 453(7197):940–3, 2008.

[67] F. R. Maxfield and T. E. McGraw. Endocytic recycling. *Nat Rev Mol Cell Biol*, 5(2):121–32, 2004.

[68] J. P. Luzio, P. R. Pryor, and N. A. Bright. Lysosomes: fusion and function. *Nat Rev Mol Cell Biol*, 8(8):622–32, 2007.

[69] A. K. Varkouhi, M. Scholte, G. Storm, and H. J. Haisma. Endosomal escape pathways for delivery of biologicals. *J Control Release*, 151(3):220–8, 2011.

[70] J. Haensler and Jr. Szoka, F. C. Polyamidoamine cascade polymers mediate efficient transfection of cells in culture. *Bioconjug Chem*, 4(5):372–9, 1993.

[71] O. Boussif, F. Lezoualc'h, M. A. Zanta, M. D. Mergny, D. Scherman, B. Demeneix, and J. P. Behr. A versatile vector for gene and oligonucleotide transfer into cells in culture and in vivo: polyethylenimine. *Proc Natl Acad Sci U S A*, 92(16):7297–301, 1995.

[72] N. D. Sonawane, Jr. Szoka, F. C., and A. S. Verkman. Chloride accumulation and swelling in endosomes enhances DNA transfer by polyamine-DNA polyplexes. *J Biol Chem*, 278(45):44826–31, 2003.

[73] A. Akinc, M. Thomas, A. M. Klibanov, and R. Langer. Exploring polyethylenimine-mediated DNA transfection and the proton sponge hypothesis. *J Gene Med*, 7(5):657–63, 2005.

[74] J. P. Behr. The proton sponge: a trick to enter cells the viruses did not exploit. *Chimia*, 51:34–36, 1997.

[75] Y. Yue, F. Jin, R. Deng, J. Cai, Z. Dai, M. C. Lin, H. F. Kung, M. A. Mattebjerg, T. L. Andresen, and C. Wu. Revisit complexation between DNA and polyethylenimine–effect of length of free polycationic chains on gene transfection. *J Control Release*, 152(1):143–51, 2011.

[76] P. R. Cullis, M. J. Hope, and C. P. Tilcock. Lipid polymorphism and the roles of lipids in membranes. *Chem Phys Lipids*, 40(2-4):127–44, 1986.

[77] I. Koltover, T. Salditt, J. O. Rädler, and C. R. Safinya. An inverted hexagonal phase of cationic liposome-DNA complexes related to DNA release and delivery. *Science*, 281(5373):78–81, 1998.

[78] E. Wagner, C. Plank, K. Zatloukal, M. Cotten, and M. L. Birnstiel. Influenza virus hemagglutinin HA-2 N-terminal fusogenic peptides augment gene transfer by transferrin-polylysine-DNA complexes: toward a synthetic virus-like gene-transfer vehicle. *Proc Natl Acad Sci U S A*, 89(17):7934–8, 1992.

[79] K. Berg and J. Moan. Lysosomes and microtubules as targets for photochemotherapy of cancer. *Photochem Photobiol*, 65(3):403–9, 1997.

[80] K. Berg, P. K. Selbo, A. Weyergang, A. Dietze, L. Prasmickaite, A. Bonsted, B. Ø. Engesæter, E. Angell-Petersen, T. Warloe, N. Frandsen, and A. Høgset. Porphyrin-related photosensitizers for cancer imaging and therapeutic applications. *J Microsc*, 218(Pt 2):133–47, 2005.

[81] K. Berg, P. K. Selbo, L. Prasmickaite, T. E. Tjelle, K. Sandvig, J. Moan, G. Gaudernack, Ø. Fodstad, S. Kjølsrud, H. Anholt, G. H. Rodal, S. K. Rodal, and A. Høgset. Photochemical internalization: a novel technology for delivery of macromolecules into cytosol. *Cancer Res*, 59(6):1180–3, 1999.

[82] A. Bonsted, E. Wagner, L. Prasmickaite, A. Høgset, and K. Berg. Photochemical enhancement of DNA delivery by EGF receptor targeted polyplexes. *Methods in molecular biology*, 434:171–81, 2008.

[83] H. Cabral, M. Nakanishi, M. Kumagai, W. D. Jang, N. Nishiyama, and K. Kataoka. A photo-activated targeting chemotherapy using glutathione sensitive camptothecin-loaded polymeric micelles. *Pharm Res*, 26(1):82–92, 2009.

[84] A. Vogel and V. Venugopalan. Mechanisms of pulsed laser ablation of biological tissues. *Chem Rev*, 103(2):577–644, 2003.

[85] E. Wagner. Strategies to improve DNA polyplexes for in vivo gene transfer: will "artificial viruses" be the answer? *Pharm Res*, 21(1):8–14, 2004.

[86] D. Schaffert and E. Wagner. Gene therapy progress and prospects: synthetic polymer-based systems. *Gene Ther*, 15(16):1131–8, 2008.

[87] R. Duncan. The dawning era of polymer therapeutics. *Nat Rev Drug Discov*, 2(5):347–60, 2003.

[88] M. Rawat, D. Singh, and S. Saraf. Nanocarriers: promising vehicle for bioactive drugs. *Biol Pharm Bull*, 29(9):1790–8, 2006.

[89] R. H. Müller, K. Mäder, and S. Gohla. Solid lipid nanoparticles (SLN) for controlled drug delivery - a review of the state of the art. *Eur J Pharm Biopharm*, 50(1):161–77, 2000.

[90] J. Buse and A. El-Aneed. Properties, engineering and applications of lipid-based nanoparticle drug-delivery systems: current research and advances. *Nanomedicine*, 5(8):1237–60, 2010.

[91] P. L. Felgner, Y. Barenholz, J. P. Behr, S. H. Cheng, P. Cullis, L. Huang, J. A. Jessee, L. Seymour, F. Szoka, A. R. Thierry, E. Wagner, and G. Wu. Nomenclature for synthetic gene delivery systems. *Human gene therapy*, 8(5):511–2, 1997.

[92] J. O. Rädler, I. Koltover, T. Salditt, and C. R. Safinya. Structure of DNA-cationic liposome complexes: DNA intercalation in multilamellar membranes in distinct interhelical packing regimes. *Science*, 275(5301):810–4, 1997.

[93] V. P. Torchilin. Recent advances with liposomes as pharmaceutical carriers. *Nat Rev Drug Discov*, 4(2):145–60, 2005.

[94] J. Huwyler, D. Wu, and W. M. Pardridge. Brain drug delivery of small molecules using immunoliposomes. *Proc Natl Acad Sci U S A*, 93(24):14164–9, 1996.

[95] N. F. Steinmetz. Viral nanoparticles as platforms for next-generation therapeutics and imaging devices. *Nanomedicine*, 6(5):634–41, 2010.

[96] Z. G. Chen. Small-molecule delivery by nanoparticles for anticancer therapy. *Trends Mol Med*, 16(12):594–602, 2010.

[97] R. Singh and K. Kostarelos. Designer adenoviruses for nanomedicine and nanodiagnostics. *Trends Biotechnol*, 27(4):220–9, 2009.

[98] M. Manchester and P. Singh. Virus-based nanoparticles (VNPs): platform technologies for diagnostic imaging. *Adv Drug Deliv Rev*, 58(14):1505–22, 2006.

[99] B. Fadeel and A. E. Garcia-Bennett. Better safe than sorry: Understanding the toxicological properties of inorganic nanoparticles manufactured for biomedical applications. *Adv Drug Deliv Rev*, 62(3):362–74, 2010.

[100] A. J. Gormley, K. Greish, A. Ray, R. Robinson, J. A. Gustafson, and H. Ghandehari. Gold nanorod mediated plasmonic photothermal therapy: A tool to enhance macromolecular delivery. *Int J Pharm*, 2011.

[101] D.H. Everett and L.K. Koopal. *Manual of Symbols and Terminology for Physicochemical Quantities and Units - Appendix II: Definitions, Terminology and Symbols in Colloid and Surface Chemistry*. International Union of Pure and Applied Chemistry (IUPAC) Division of Physical Chemistry, 1971.

[102] C. T. Kresge, M. E. Leonowicz, W. J. Roth, J. C. Vartuli, and J. S. Beck. Ordered mesoporous molecular sieves synthesized by a liquid-crystal template mechanism. *Nature*, 359:710–712, 1992.

[103] M. Vallet-Regi, F. Balas, and D. Arcos. Mesoporous materials for drug delivery. *Angew Chem Int Ed*, 46(40):7548–58, 2007.

[104] B. G. Trewyn, II Slowing, S. Giri, H. T. Chen, and V. S. Lin. Synthesis and functionalization of a mesoporous silica nanoparticle based on the sol-gel process and applications in controlled release. *Acc Chem Res*, 40(9):846–53, 2007.

[105] A. Corma. From microporous to mesoporous molecular sieve materials and their use in catalysis. *Chem Rev*, 97(6):2373–2420, 1997.

[106] A. Stein, B. J. Melde, and R. C. Schroden. Hybrid inorganic-organic mesoporous silicates - nanoscopic reactors coming of age. *Adv Mater*, 12(19):1403–1419, 2000.

[107] X. Feng, G. E. Fryxell, L.-Q. Wang, A. Y. Kim, J. Liu, and K. M. Kemner. Functionalized monolayers on ordered mesoporous supports. *Science*, 276(5314):923–926, 1997.

[108] M. Vallet-Regi, L. Ruiz-Gonzalez, Isabel Izquierdo-Barba, and J. M. Gonzalez-Calbet. Revisiting silica based ordered mesoporous materials: medical applications. *J Mater Chem*, 16(1):26–31, 2006.

[109] M. Vallet-Regi, A. Ramila, R.P. del Real, and J. Perez-Pariente. A new property of MCM-41: Drug delivery system. *Chem Mater*, 13:308–311, 2001.

[110] T. Lebold, C. Jung, J. Michaelis, and C. Bräuchle. Nanostructured silica materials as drug-delivery systems for doxorubicin: single molecule and cellular studies. *Nano Lett*, 9(8):2877–83, 2009.

[111] S. Pevzner, O. Regev, and R. Yerushalmi-Rozen. Thin films of mesoporous silica: preparation and characterization. *Curr Opin Colloid Interface Sci*, 4(6):420–427, 2000.

[112] T. Yamada, H. Zhou, K. Asai, and I. Honma. Pore size controlled mesoporous silicate powder prepared by triblock copolymer templates. *Mater Lett*, 56:93–96, 2002.

[113] C. Y. Mou and H.-Y. Lin. Control of morphology in synthesizing mesoporous silica. *Pure Appl Chem*, 72:137–146, 2000.

[114] J. L. Vivero-Escoto, II Slowing, B. G. Trewyn, and V. S. Lin. Mesoporous silica nanoparticles for intracellular controlled drug delivery. *Small*, 6(18):1952–67, 2010.

[115] L. S. Wang, L. C. Wu, S. Y. Lu, L. L. Chang, I. T. Teng, C. M. Yang, and J. A. Ho. Biofunctionalized phospholipid-capped mesoporous silica nanoshuttles for targeted drug delivery: improved water suspensibility and decreased nonspecific protein binding. *ACS Nano*, 4(8):4371–9, 2010.

[116] P. Kortesuo, M. Ahola, S. Karlsson, I. Kangasniemi, A. Yli-Urpo, and J. Kiesvaara. Silica xerogel as an implantable carrier for controlled drug delivery–evaluation of drug distribution and tissue effects after implantation. *Biomaterials*, 21(2):193–8, 2000.

[117] S. Radin, G. El-Bassyouni, E. J. Vresilovic, E. Schepers, and P. Ducheyne. In vivo tissue response to resorbable silica xerogels as controlled-release materials. *Biomaterials*, 26(9):1043–52, 2005.

[118] K. R. Martin. The chemistry of silica and its potential health benefits. *J Nutr Health Aging*, 11(2):94–7, 2007.

[119] II Slowing, B. G. Trewyn, and V. S. Lin. Mesoporous silica nanoparticles for intracellular delivery of membrane-impermeable proteins. *J Am Chem Soc*, 129(28):8845–9, 2007.

[120] C. Tourne-Peteilh, D. A. Lerner, C. Charnay, L. Nicole, S. Begu, and J. M. Devoisselle. The potential of ordered mesoporous silica for the storage of drugs: the example of a pentapeptide encapsulated in a MSU-tween 80. *ChemPhysChem*, 4(3):281–6, 2003.

[121] Q. Huo, D.I. Margolese, and G.D. Stucky. Surfactant control of phases in the synthesis of mesoporous silica-based materials. *Chem Mater*, 8(5):1147, 1996.

[122] N. Lang and A. Tuel. A fast and efficient ion-exchange procedure to remove surfactant molecules from MCM-41 materials. *Chem Mater*, 16(10):1961–1966, 2004.

[123] A. Schlossbauer, D. Schaffert, J. Kecht, E. Wagner, and T. Bein. Click chemistry for high-density biofunctionalization of mesoporous silica. *J Am Chem Soc*, 130(38):12558–9, 2008.

[124] R. Mortera, J. Vivero-Escoto, II Slowing, E. Garrone, B. Onida, and V. S. Lin. Cell-induced intracellular controlled release of membrane impermeable cysteine from a mesoporous silica nanoparticle-based drug delivery system. *Chem Commun*, (22):3219–21, 2009.

[125] V. Cauda, C. Argyo, A. Schlossbauer, and T. Bein. Controlling the delivery kinetics from colloidal mesoporous silica nanoparticles with pH-sensitive gates. *J Mater Chem*, 20:4305–4311, 2010.

[126] M. Vallet-Regi. Ordered mesoporous materials in the context of drug delivery systems and bone tissue engineering. *Chemistry*, 12(23):5934–43, 2006.

[127] A. Nieto, M. Colilla, F. Balas, and M. Vallet-Regi. Surface electrochemistry of mesoporous silicas as a key factor in the design of tailored delivery devices. *Langmuir*, 26(7):5038–49, 2010.

[128] C. E. Ashley, E. C. Carnes, G. K. Phillips, D. Padilla, P. N. Durfee, P. A. Brown, T. N. Hanna, J. Liu, B. Phillips, M. B. Carter, N. J. Carroll, X. Jiang, D. R. Dunphy, C. L. Willman, D. N. Petsev, D. G. Evans, A. N. Parikh, B. Chackerian, W. Wharton, D. S. Peabody, and C. J. Brinker. The targeted delivery of multicomponent cargos to cancer cells by nanoporous particle-supported lipid bilayers. *Nat Mater*, 10(5):389–97, 2011.

[129] C. Y. Lai, B. G. Trewyn, D. M. Jeftinija, K. Jeftinija, S. Xu, S. Jeftinija, and V. S. Lin. A mesoporous silica nanosphere-based carrier system with chemically removable CdS nanoparticle caps for stimuli-responsive controlled release of neurotransmitters and drug molecules. *J Am Chem Soc*, 125(15):4451–9, 2003.

[130] Y. Zhang, Z. Zhi, T. Jiang, J. Zhang, Z. Wang, and S. Wang. Spherical mesoporous silica nanoparticles for loading and release of the poorly water-soluble drug telmisartan. *J Control Release*, 145(3):257–263, 2010.

[131] J. Lu, E. Choi, F. Tamanoi, and J. I. Zink. Light-activated nanoimpeller-controlled drug release in cancer cells. *Small*, 4(4):421–426, 2008.

[132] A. M. Chen, M. Zhang, D. Wei, D. Stueber, O. Taratula, T. Minko, and H. He. Co-delivery of doxorubicin and Bcl-2 siRNA by mesoporous silica nanoparticles enhances the efficacy of chemotherapy in multidrug-resistant cancer cells. *Small*, 5(23):2673–2677, 2009.

[133] C. H. Lee, S. H. Cheng, I. P. Huang, J. S. Souris, C. S. Yang, C. Y. Mou, and L. W. Lo. Intracellular pH-responsive mesoporous silica nanoparticles for the controlled release of anticancer chemotherapeutics. *Angew Chem Int Ed*, 2010.

[134] Y. Zhao, B. G. Trewyn, II Slowing, and V. S. Lin. Mesoporous silica nanoparticle-based double drug delivery system for glucose-responsive controlled release of insulin and cyclic AMP. *J Am Chem Soc*, 131(24):8398–400, 2009.

[135] S. Angelos, N. M. Khashab, Y. W. Yang, A. Trabolsi, H. A. Khatib, J. F. Stoddart, and J. I. Zink. pH clock-operated mechanized nanoparticles. *J Am Chem Soc*, 131(36):12912–4, 2009.

[136] J. M. Rosenholm, E. Peuhu, J. E. Eriksson, C. Sahlgren, and M. Linden. Targeted intracellular delivery of hydrophobic agents using mesoporous hybrid silica nanoparticles as carrier systems. *Nano Lett*, 9(9):3308–11, 2009.

[137] T. D. Nguyen, K. C. F. Leung, M. Liong, Y. Liu, J. F. Stoddart, and J. I. Zink. Versatile supramolecular nanovalves reconfigured for light activation. *Adv Funct Mater*, 17(13):2101–2110, 2007.

[138] E. Aznar, M. D. Marcos, R. Martinez-Manez, F. Sancenon, J. Soto, P. Amoros, and C. Guillem. pH- and photo-switched release of guest molecules from mesoporous silica supports. *J Am Chem Soc*, 131(19):6833–43, 2009.

[139] C. L. Zhu, C. H. Lu, X. Y. Song, H. H. Yang, and X. R. Wang. Bioresponsive controlled release using mesoporous silica nanoparticles capped with aptamer-based molecular gate. *J Am Chem Soc*, 133(5):1278–81, 2011.

[140] A. Schlossbauer, J. Kecht, and T. Bein. Biotin-avidin as a protease-responsive cap system for controlled guest release from colloidal mesoporous silica. *Angew Chem Int Ed*, 48(17):3092–5, 2009.

[141] J. L. Vivero-Escoto, II Slowing, C. W. Wu, and V. S. Lin. Photoinduced intracellular controlled release drug delivery in human cells by gold-capped mesoporous silica nanosphere. *J Am Chem Soc*, 131(10):3462–3, 2009.

[142] T. W. Kim, II Slowing, P. W. Chung, and V. S. Lin. Ordered mesoporous polymer-silica hybrid nanoparticles as vehicles for the intracellular controlled release of macromolecules. *ACS Nano*, 5(1):360–6, 2011.

[143] J. Liu, A. Stace-Naughton, X. Jiang, and C. J. Brinker. Porous nanoparticle supported lipid bilayers (protocells) as delivery vehicles. *J Am Chem Soc*, 131(4):1354–5, 2009.

[144] J. Liu, X. Jiang, C. Ashley, and C. J. Brinker. Electrostatically mediated liposome fusion and lipid exchange with a nanoparticle-supported bilayer for control of surface charge, drug containment, and delivery. *J Am Chem Soc*, 131(22):7567–9, 2009.

[145] E. Climent, A. Bernardos, R. Martinez-Manez, A. Maquieira, M. D. Marcos, N. Pastor-Navarro, R. Puchades, F. Sancenon, J. Soto, and P. Amoros. Controlled delivery systems using antibody-capped mesoporous nanocontainers. *J Am Chem Soc*, 2009.

[146] Z. Luo, K. Cai, Y. Hu, L. Zhao, P. Liu, L. Duan, and W. Yang. Mesoporous silica nanoparticles end-capped with collagen: Redox-responsive nanoreservoirs for targeted drug delivery. *Angew Chem Int Ed*, 50(3):640–3, 2010.

[147] C. Coll, L. Mondragon, R. Martinez-Manez, F. Sancenon, M. D. Marcos, J. Soto, P. Amoros, and E. Perez-Paya. Enzyme-mediated controlled release systems by anchoring peptide sequences on mesoporous silica supports. *Angew Chem Int Ed*, 50(9):2138–40, 2011.

[148] Q. Gao, Y. Xu, D. Wu, Y. Sun, and X. Li. pH-responsive drug release from polymer-coated mesoporous silica spheres. *J Phys Chem*, 113(29):12753–12758, 2009.

[149] A. Bernardos, E. Aznar, M. D. Marcos, R. Martinez-Manez, F. Sancenon, J. Soto, J. M. Barat, and P. Amoros. Enzyme-responsive controlled release using mesoporous silica supports capped with lactose. *Angew Chem Int Ed*, 48(32):5884–7, 2009.

[150] C. Chen, J. Geng, F. Pu, X. Yang, J. Ren, and X. Qu. Polyvalent nucleic acid/mesoporous silica nanoparticle conjugates: dual stimuli-responsive vehicles for intracellular drug delivery. *Angew Chem Int Ed*, 50(4):882–6, 2011.

[151] T. D. Nguyen, H. R. Tseng, P. C. Celestre, A. H. Flood, Y. Liu, J. F. Stoddart, and J. I. Zink. A reversible molecular valve. *Proc Natl Acad Sci U S A*, 102(29):10029–34, 2005.

[152] T. D. Nguyen, K. C. F. Leung, M. Liong, C. D. Pentecost, J. F. Stoddart, and J. I. Zink. Construction of a pH-driven supramolecular nanovalve. *Org Lett*, 8(15):3363–3366, 2006.

[153] T. D. Nguyen, Y. Liu, S. Saha, K. C. Leung, J. F. Stoddart, and J. I. Zink. Design and optimization of molecular nanovalves based on redox-switchable bistable rotaxanes. *J Am Chem Soc*, 129(3):626–34, 2007.

[154] S. Angelos, E. Choi, F. Vogtle, L. De Cola, and J. I. Zink. Photo-driven expulsion of molecules from mesostructured silica nanoparticles. *J Phys Chem C*, 111(18):6589–6592, 2007.

[155] S. Angelos, Y. W. Yang, K. Patel, J. F. Stoddart, and J. I. Zink. pH-responsive supramolecular nanovalves based on cucurbit[6]uril pseudorotaxanes. *Angew Chem Int Ed*, 47(12):2222–6, 2008.

[156] K. Patel, S. Angelos, W. R. Dichtel, A. Coskun, Y. W. Yang, J. I. Zink, and J. F. Stoddart. Enzyme-responsive snap-top covered silica nanocontainers. *J Am Chem Soc*, 130(8):2382–3, 2008.

[157] D. P. Ferris, Y. L. Zhao, N. M. Khashab, H. A. Khatib, J. F. Stoddart, and J. I. Zink. Light-operated mechanized nanoparticles. *J Am Chem Soc*, 131(5):1686–8, 2009.

[158] S. Angelos, Y. W. Yang, N. M. Khashab, J. F. Stoddart, and J. I. Zink. Dual-controlled nanoparticles exhibiting AND logic. *J Am Chem Soc*, 2009.

[159] M. W. Ambrogio, T. A. Pecorelli, K. Patel, N. M. Khashab, A. Trabolsi, H. A. Khatib, Y. Y. Botros, J. I. Zink, and J. F. Stoddart. Snap-top nanocarriers. *Org Lett*, 12(15):3304–3307, 2010.

[160] J. M. Rosenholm, A. Meinander, E. Peuhu, R. Niemi, J. E. Eriksson, C. Sahlgren, and M. Linden. Targeting of porous hybrid silica nanoparticles to cancer cells. *ACS Nano*, 3(1):197–206, 2009.

[161] I. Slowing, B. G. Trewyn, and V. S. Lin. Effect of surface functionalization of MCM-41-type mesoporous silica nanoparticles on the endocytosis by human cancer cells. *J Am Chem Soc*, 128(46):14792–3, 2006.

[162] V. Lebret, L. Raehm, J.-O. Durand, M. Smaihi, M. Werts, M. Blanchard-Desce, D. Methy-Gonnod, and C. Dubernet. Surface functionalization of two-photon dye-doped mesoporous silica nanoparticles with folic acid: cytotoxicity studies with HeLa and MCF-7 cancer cells. *J Sol-Gel Sci Technol*, 48(1-2):32–39, 2008.

[163] D. P. Ferris, J. Lu, C. Gothard, R. Yanes, C. R. Thomas, J. C. Olsen, J. F. Stoddart, F. Tamanoi, and J. I. Zink. Synthesis of biomolecule-modified mesoporous silica nanoparticles for targeted hydrophobic drug delivery to cancer cells. *Small*, 2011.

[164] C. P. Tsai, C. Y. Chen, Y. Hung, F. H. Chang, and C. Y. Mou. Monoclonal antibody-functionalized mesoporous silica nanoparticles (MSN) for selective targeting breast cancer cells. *J Mater Chem*, 19(32):5737–5743, 2009.

[165] C. L. Zhu, X. Y. Song, W. H. Zhou, H. H. Yang, Y. H. Wen, and X. R. Wang. An efficient cell-targeting and intracellular controlled-release drug delivery system based on mesoporous silica nanoparticle-polyelectrolyte multilayer-aptamer conjugates. *J Mater Chem*, 19(41):7765–7770, 2009.

[166] D. Brevet, M. Gary-Bobo, L. Raehm, S. Richeter, O. Hocine, K. Amro, B. Loock, P. Couleaud, C. Frochot, A. Morere, P. Maillard, M. Garcia, and J. O. Durand. Mannose-targeted mesoporous silica nanoparticles for photodynamic therapy. *Chem Commun*, (12):1475–7, 2009.

[167] I. Y. Park, I. Y. Kim, M. K. Yoo, Y. J. Choi, M. H. Cho, and C. S. Cho. Mannosylated polyethylenimine coupled mesoporous silica nanoparticles for receptor-mediated gene delivery. *Int J Pharm*, 359(1-2):280–7, 2008.

[168] J. M. Rosenholm, E. Peuhu, L. T. Bate-Eya, J. E. Eriksson, C. Sahlgren, and M. Linden. Cancer-cell-specific induction of apoptosis using mesoporous silica nanoparticles as drug-delivery vectors. *Small*, 6(11):1234–41, 2010.

[169] C. R. Thomas, D. P. Ferris, J. H. Lee, E. Choi, M. H. Cho, E. S. Kim, J. F. Stoddart, J. S. Shin, J. Cheon, and J. I. Zink. Noninvasive remote-controlled release of drug molecules in vitro using magnetic actuation of mechanized nanoparticles. *J Am Chem Soc*, 132(31):10623–5, 2010.

[170] A. Schlossbauer, S. Warncke, P.M.E. Gramlich, J. Kecht, A. Manetto, T. Carell, and T. Bein. A programmable DNA-based molecular valve for colloidal mesoporous silica. *Angew Chem Int Ed*, 49(28):4734–4737, 2010.

[171] F. Muhammad, M. Guo, W. Qi, F. Sun, A. Wang, Y. Guo, and G. Zhu. pH-triggered controlled drug release from mesoporous silica nanoparticles via intracelluar dissolution of ZnO nanolids. *J Am Chem Soc*, 2011.

[172] R. Liu, X. Zhao, T. Wu, and P. Feng. Tunable redox-responsive hybrid nanogated ensembles. *J Am Chem Soc*, 130(44):14418–9, 2008.

[173] I. Slowing, J. L. Vivero-Escoto, C. W. Wu, and V. S. Lin. Mesoporous silica nanoparticles as controlled release drug delivery and gene transfection carriers. *Adv Drug Deliv Rev*, 60(11):1278–88, 2008.

[174] S. H. Wu, Y. S. Lin, Y. Hung, Y. H. Chou, Y. H. Hsu, C. Chang, and C. Y. Mou. Multifunctional mesoporous silica nanoparticles for intracellular labeling and animal magnetic resonance imaging studies. *Chembiochem*, 9(1):53–7, 2008.

[175] J. Lu, M. Liong, Z. Li, J. I. Zink, and F. Tamanoi. Biocompatibility, biodistribution, and drug-delivery efficiency of mesoporous silica nanoparticles for cancer therapy in animals. *Small*, 6(16):1794–1805, 2010.

[176] Q. He, Z. Zhang, F. Gao, Y. Li, and J. Shi. In vivo biodistribution and urinary excretion of mesoporous silica nanoparticles: effects of particle size and PEGylation. *Small*, 7(2):271–80, 2011.

[177] S. Metz, G. Bonaterra, M. Rudelius, M. Settles, E. J. Rummeny, and H. E. Daldrup-Link. Capacity of human monocytes to phagocytose approved iron oxide MR contrast agents in vitro. *Eur Radiol*, 14(10):1851–8, 2004.

[178] M. Longmire, P. L. Choyke, and H. Kobayashi. Clearance properties of nano-sized particles and molecules as imaging agents: considerations and caveats. *Nanomedicine*, 3(5):703–17, 2008.

[179] H. Vallhov, S. Gabrielsson, M. Stromme, A. Scheynius, and A. E. Garcia-Bennett. Mesoporous silica particles induce size dependent effects on human dendritic cells. *Nano Lett*, 7(12):3576–82, 2007.

[180] Q. He, Z. Zhang, Y. Gao, J. Shi, and Y. Li. Intracellular localization and cytotoxicity of spherical mesoporous silica nano- and microparticles. *Small*, 5(23):2722–2729, 2009.

[181] J. M. Rosenholm, C. Sahlgren, and M. Linden. Towards multifunctional, targeted drug delivery systems using mesoporous silica nanoparticles–opportunities and challenges. *Nanoscale*, 2(10):1870–83, 2010.

[182] Q. He, J. Zhang, J. Shi, Z. Zhu, L. Zhang, W. Bu, L. Guo, and Y. Chen. The effect of PEGylation of mesoporous silica nanoparticles on nonspecific binding of serum proteins and cellular responses. *Biomaterials*, 31(6):1085–92, 2010.

[183] Y. S. Lin, N. Abadeer, and C. L. Haynes. Stability of small mesoporous silica nanoparticles in biological media. *Chem Commun*, 47(1):532–4, 2011.

[184] Y. S. Lin and C. L. Haynes. Impacts of mesoporous silica nanoparticle size, pore ordering, and pore integrity on hemolytic activity. *J Am Chem Soc*, 132(13):4834–42, 2010.

[185] T. H. Chung, S. H. Wu, M. Yao, C. W. Lu, Y. S. Lin, Y. Hung, C. Y. Mou, Y. C. Chen, and D. M. Huang. The effect of surface charge on the uptake and biological function of mesoporous silica nanoparticles in 3T3-L1 cells and human mesenchymal stem cells. *Biomaterials*, 28(19):2959–66, 2007.

[186] II Slowing, C. W. Wu, J. L. Vivero-Escoto, and V. S. Lin. Mesoporous silica nanoparticles for reducing hemolytic activity towards mammalian red blood cells. *Small*, 5(1):57–62, 2009.

[187] D. R. Radu, C. Y. Lai, K. Jeftinija, E. W. Rowe, S. Jeftinija, and V. S. Lin. A polyamidoamine dendrimer-capped mesoporous silica nanosphere-based gene transfection reagent. *J Am Chem Soc*, 126(41):13216–7, 2004.

[188] K. M. Taylor, J. S. Kim, W. J. Rieter, H. An, and W. Lin. Mesoporous silica nanospheres as highly efficient MRI contrast agents. *J Am Chem Soc*, 130(7):2154–5, 2008.

[189] S. P. Hudson, R. F. Padera, R. Langer, and D. S. Kohane. The biocompatibility of mesoporous silicates. *Biomaterials*, 29(30):4045–55, 2008.

[190] Q. He, J. Shi, M. Zhu, Y. Chen, and F. Chen. The three-stage in vitro degradation behavior of mesoporous silica in simulated body fluid. *Microporous Mesoporous Mater*, 131(1-3):314–320, 2010.

[191] V. Cauda, A. Schlossbauer, and T. Bein. Bio-degradation study of colloidal mesoporous silica nanoparticles: Effect of surface functionalization with organo-silanes and poly(ethylene glycol). *Microporous Mesoporous Mater*, 132(1-2):60–71, 2010.

[192] A. Zürner, J. Kirstein, M. Döblinger, C. Bräuchle, and T. Bein. Visualizing single-molecule diffusion in mesoporous materials. *Nature*, 450(7170):705–8, 2007.

[193] J. Kirstein, B. Platschek, C. Jung, R. Brown, T. Bein, and C. Bräuchle. Exploration of nanostructured channel systems with single-molecule probes. *Nat Mater*, 6(4):303–10, 2007.

[194] T. Lebold, L. A. Mühlstein, J. Blechinger, M. Riederer, H. Amenitsch, R. Kohn, K. Peneva, K. Müllen, J. Michaelis, C. Bräuchle, and T. Bein. Tuning single-molecule dynamics in functionalized mesoporous silica. *Chemistry*, 15(7):1661–72, 2009.

[195] C. Jung, P. Schwaderer, M. Dethlefsen, R. Kohn, J. Michaelis, and C. Bräuchle. Visualization of the self-assembly of silica nanochannels reveals growth mechanism. *Nat Nanotechnol*, 6(2):87–92, 2011.

[196] T. Lebold, J. Michaelis, and C. Bräuchle. The complexity of mesoporous silica nanomaterials unravelled by single molecule microscopy. *Phys Chem Chem Phys*, 13(11):5017–33, 2011.

[197] G. Seisenberger, M. U. Ried, T. Endress, H. Büning, M. Hallek, and C. Bräuchle. Real-time single-molecule imaging of the infection pathway of an adeno-associated virus. *Science*, 294(5548):1929–32, 2001.

[198] S. Ivanchenko, W. J. Godinez, M. Lampe, H. G. Kräusslich, R. Eils, K. Rohr, C. Bräuchle, B. Müller, and D. C. Lamb. Dynamics of HIV-1 assembly and release. *PLoS Pathog*, 5(11):e1000652, 2009.

[199] V. Baumgärtel, S. Ivanchenko, A. Dupont, M. Sergeev, P. W. Wiseman, H. G. Kräusslich, C. Bräuchle, B. Müller, and D. C. Lamb. Live-cell visualization of dynamics of HIV budding site interactions with an ESCRT component. *Nat Cell Biol*, 13(4):469–74, 2011.

[200] D.C. Lamb and C. Bräuchle. Dem Molekül auf der Spur. *Physik Journal*, 6(12):39–45, 2007.

[201] N. Ruthardt, D. C. Lamb, and C. Bräuchle. Single-particle tracking as a quantitative microscopy-based approach to unravel cell entry mechanisms of viruses and pharmaceutical nanoparticles. *Mol Ther*, 19(7):1199–211, 2011.

[202] J. W. Lichtman and J. A. Conchello. Fluorescence microscopy. *Nat Methods*, 2(12):910–9, 2005.

[203] J. R. Lakowicz. *Principles of fluorescence spectroscopy.* 2nd edition, 1999.

[204] N. Turro, V. Ramamurthy, and J.C. Scaiano. *Principles of Molecular photochemistry. An introduction.* University Science Books Sausalito, California, 2009.

[205] B. N. Giepmans, S. R. Adams, M. H. Ellisman, and R. Y. Tsien. The fluorescent toolbox for assessing protein location and function. *Science*, 312(5771):217–24, 2006.

[206] S. A. Claridge, J. J. Schwartz, and P. S. Weiss. Electrons, photons, and force: quantitative single-molecule measurements from physics to biology. *ACS Nano*, 5(2):693–729, 2011.

[207] J. R. Lakowicz. Radiative decay engineering: biophysical and biomedical applications. *Anal Biochem*, 298(1):1–24, 2001.

[208] M. R. Eftink and C. A. Ghiron. Fluorescence quenching studies with proteins. *Analytical biochemistry*, 114(2):199–227, 1981.

[209] D. Gerion. *Fluorescence imaging in biology using nanoprobes.* Nanosystem characterization tools in the life sciences. Wiley-VHC Verlag GmbH & Co. KGaA, Weinheim, 2006.

[210] D. B. Schmolze, C. Standley, K. E. Fogarty, and A. H. Fischer. Advances in microscopy techniques. *Arch Pathol Lab Med*, 135(2):255–63, 2011.

[211] L. Kastrup, D. Wildanger, B. Rankin, and S.W. Hell. *STED microscopy with compact light sources*. Nanoscopy and mutidimensional optical fluorescence microscopy. Taylor and Francis Group, Boca Raton, FL, 2010.

[212] H. Kobayashi, M. Ogawa, R. Alford, P. L. Choyke, and Y. Urano. New strategies for fluorescent probe design in medical diagnostic imaging. *Chem Rev*, 110(5):2620–40, 2010.

[213] R. Y. Tsien. Constructing and exploiting the fluorescent protein paintbox (nobel lecture). *Angew Chem Int Ed*, 48(31):5612–26, 2009.

[214] J. T. Wessels, K. Yamauchi, R. M. Hoffman, and F. S. Wouters. Advances in cellular, subcellular, and nanoscale imaging in vitro and in vivo. *Cytometry A*, 77(7):667–76, 2010.

[215] R. M. Hoffman. The multiple uses of fluorescent proteins to visualize cancer in vivo. *Nat Rev Cancer*, 5(10):796–806, 2005.

[216] Y. Sako. Imaging single molecules in living cells for systems biology. *Mol Syst Biol*, 2:56, 2006.

[217] S.R. Sternberg. Biomedical image processing. *Computer*, 16(1):22–34, 1983.

[218] M. Wang and M. Thanou. Targeting nanoparticles to cancer. *Pharmacol Res*, 62(2):90–9, 2010.

[219] N. Modi, N. Gulati, K. Solomon, T. Monaghan, A. Robins, H. F. Sewell, and Y. R. Mahida. Differential binding and internalization of clostridium difficile toxin a by human peripheral blood monocytes, neutrophils and lymphocytes. *Scand J Immunol*, 74(3):264–71, 2011.

[220] J. Nuutila and E. M. Lilius. Flow cytometric quantitative determination of ingestion by phagocytes needs the distinguishing of overlapping populations of binding and ingesting cells. *Cytometry A*, 65(2):93–102, 2005.

[221] H. Xu, F. Yan, E. E. Monson, and R. Kopelman. Room-temperature preparation and characterization of poly (ethylene glycol)-coated silica nanoparticles for biomedical applications. *J Biomed Mater Res A*, 66(4):870–9, 2003.

[222] C. Argyo. Inorganic-organic core-shell nanoparticles - PEGylated colloidal mesoporous silica. *Diploma Thesis, LMU Munich*, 2009.

[223] T. T. Kwok and R. M. Sutherland. Differences in EGF related radiosensitisation of human squamous carcinoma cells with high and low numbers of EGF receptors. *Br J Cancer*, 64(2):251–4, 1991.

[224] R. S. Herbst. Review of epidermal growth factor receptor biology. *International journal of radiation oncology, biology, physics*, 59(2 Suppl):21–6, 2004.

[225] N. K. Mal, M. Fujiwara, and Y. Tanaka. Photocontrolled reversible release of guest molecules from coumarin-modified mesoporous silica. *Nature*, 421(6921):350–3, 2003.

[226] G. Nordlund, J. B. Sing Ng, L. Bergström, and P. Brzezinski. A membrane-reconstituted multisubunit functional proton pump on mesoporous silica particles. *ACS Nano*, 3(9):2639–46, 2009.

[227] P. M. Kasson and V. S. Pande. Control of membrane fusion mechanism by lipid composition: predictions from ensemble molecular dynamics. *PLoS Comput Biol*, 3(11):e220, 2007.

[228] A. O. Hohner, M. P. David, and J. O. Rädler. Controlled solvent-exchange deposition of phospholipid membranes onto solid surfaces. *Biointerphases*, 5(1):1–8, 2010.

[229] D. Mudhakir and H. Harashima. Learning from the viral journey: how to enter cells and how to overcome intracellular barriers to reach the nucleus. *The AAPS journal*, 11(1):65–77, 2009.

[230] S. Berezhna, S. Schaefer, R. Heintzmann, M. Jahnz, G. Boese, A. Deniz, and P. Schwille. New effects in polynucleotide release from cationic lipid carriers revealed by confocal imaging, fluorescence cross-correlation spectroscopy and single particle tracking. *Biochim Biophys Acta*, 1669(2):193–207, 2005.

[231] R. B. Ravelli, B. Gigant, P. A. Curmi, I. Jourdain, S. Lachkar, A. Sobel, and M. Knossow. Insight into tubulin regulation from a complex with colchicine and a stathmin-like domain. *Nature*, 428(6979):198–202, 2004.

[232] B. Bhattacharyya, D. Panda, S. Gupta, and M. Banerjee. Anti-mitotic activity of colchicine and the structural basis for its interaction with tubulin. *Med Res Rev*, 28(1):155–83, 2008.

[233] A. L. Risinger, F. J. Giles, and S. L. Mooberry. Microtubule dynamics as a target in oncology. *Cancer Treat Rev*, 35(3):255–61, 2009.

[234] J Janik. Quenching Experimente an medizinisch relevanten mesoporoesen Nanopartikeln und Optimierung eines Mikrofluidiksystems zur Simulation von Blutgefaessen. *B.Sc. Thesis, LMU Munich*, 2009.

[235] A.A. Torrano, J. Blechinger, C. Argyo, A. Reller, T. Bein, and C. Bräuchle. A fast analysis method to quantify nanoparticle uptake on a single cell level. *under review*, 2011.

[236] S. A. Carlsen, J. E. Till, and V. Ling. Modulation of membrane drug permeability in chinese hamster ovary cells. *Biochim Biophys Acta*, 455(3):900–12, 1976.

[237] J. H. Felgner, R. Kumar, C. N. Sridhar, C. J. Wheeler, Y. J. Tsai, R. Border, P. Ramsey, M. Martin, and P. L. Felgner. Enhanced gene delivery and mechanism studies with a novel series of cationic lipid formulations. *J Biol Chem*, 269(4):2550–61, 1994.

[238] I. M. Hafez and P. R. Cullis. Roles of lipid polymorphism in intracellular delivery. *Adv Drug Deliv Rev*, 47(2-3):139–48, 2001.

[239] N. Düzgünes, J. A. Goldstein, D. S. Friend, and P. L. Felgner. Fusion of liposomes containing a novel cationic lipid, N-[2,3-(dioleyloxy)propyl]-N,N,N-trimethylammonium: induction by multivalent anions and asymmetric fusion with acidic phospholipid vesicles. *Biochemistry*, 28(23):9179–84, 1989.

[240] K. Lappalainen, I. Jaaskelainen, K. Syrjanen, A. Urtti, and S. Syrjanen. Comparison of cell proliferation and toxicity assays using two cationic liposomes. *Pharm Res*, 11(8):1127–31, 1994.

[241] G. D. Scarioti, A. Lubambo, J. P. Feitosa, M. R. Sierakowski, T. M. Bresolin, and R. A. de Freitas. Nanocapsule of cationic liposomes obtained using "in situ" acrylic acid polymerization: Stability, surface charge and biocompatibility. *Colloids Surf B Biointerfaces*, 87(2):267–72, 2011.

[242] I. Martin and J. M. Ruysschaert. Common properties of fusion peptides from diverse systems. *Biosci Rep*, 20(6):483–500, 2000.

[243] W. Antonin, D. Fasshauer, S. Becker, R. Jahn, and T. R. Schneider. Crystal structure of the endosomal SNARE complex reveals common structural principles of all SNAREs. *Nat Struct Biol*, 9(2):107–11, 2002.

[244] A. Høgset, L. Prasmickaite, M. Hellum, B. Ø. Engesæter, V. M. Olsen, T. E. Tjelle, C. J. Wheeler, and K. Berg. Photochemical transfection: a technology for efficient light-directed gene delivery. *Somat Cell Mol Genet*, 27(1-6):97–113, 2002.

[245] A. Høgset, L. Prasmickaite, P. K. Selbo, M. Hellum, B. Ø. Engesæter, A. Bonsted, and K. Berg. Photochemical internalisation in drug and gene delivery. *Adv Drug Deliv Rev*, 56(1):95–115, 2004.

[246] R. Schmidt. Photosensitized generation of singlet oxygen. *Photochem Photobiol*, 82(5):1161–77, 2006.

[247] J. Moan and K. Berg. The photodegradation of porphyrins in cells can be used to estimate the lifetime of singlet oxygen. *Photochem Photobiol*, 53(4):549–53, 1991.

[248] A. Pastore, G. Federici, E. Bertini, and F. Piemonte. Analysis of glutathione: implication in redox and detoxification. *Clin Chim Acta*, 333(1):19–39, 2003.

[249] A. Schlossbauer. Biofunctionalized mesoporous silica for controlled release applications. *Ph.D. Thesis, LMU Munich*, 2010.

[250] S. Pollock, R. Antrobus, L. Newton, B. Kampa, J. Rossa, S. Latham, N. B. Nichita, R. A. Dwek, and N. Zitzmann. Uptake and trafficking of liposomes to the endoplasmic reticulum. *Faseb J*, 24(6):1866–78, 2010.

[251] D. M. Huang, Y. Hung, B. S. Ko, S. C. Hsu, W. H. Chen, C. L. Chien, C. P. Tsai, C. T. Kuo, J. C. Kang, C. S. Yang, C. Y. Mou, and Y. C. Chen. Highly efficient cellular labeling of mesoporous nanoparticles in human mesenchymal stem cells: implication for stem cell tracking. *Faseb J*, 19(14):2014–6, 2005.

[252] E. Dauty and A. S. Verkman. Actin cytoskeleton as the principal determinant of size-dependent DNA mobility in cytoplasm: a new barrier for non-viral gene delivery. *J Biol Chem*, 280(9):7823–8, 2005.

[253] H. Guo, H. Qian, N. M. Idris, and Y. Zhang. Singlet oxygen-induced apoptosis of cancer cells using upconversion fluorescent nanoparticles as a carrier of photosensitizer. *Nanomedicine*, 6(3):486–95, 2010.

[254] R. Zhang, C. Wu, L. Tong, B. Tang, and Q. H. Xu. Multifunctional core-shell nanoparticles as highly efficient imaging and photosensitizing agents. *Langmuir*, 25(17):10153–8, 2009.

[255] T. Zhao, H. Wu, S. Q. Yao, Q. H. Xu, and G. Q. Xu. Nanocomposites containing gold nanorods and porphyrin-doped mesoporous silica with dual capability of two-photon imaging and photosensitization. *Langmuir*, 26(18):14937–42, 2010.

[256] Y. Yang, W. Song, A. Wang, P. Zhu, J. Fei, and J. Li. Lipid coated mesoporous silica nanoparticles as photosensitive drug carriers. *Phys Chem Chem Phys*, 12(17):4418–22, 2010.

[257] S. Febvay, D. M. Marini, A. M. Belcher, and D. E. Clapham. Targeted cytosolic delivery of cell-impermeable compounds by nanoparticle-mediated, light-triggered endosome disruption. *Nano Lett*, 10(6):2211–9, 2010.

[258] Q. Peng, K. Berg, J. Moan, M. Kongshaug, and J. M. Nesland. 5-Aminolevulinic acid-based photodynamic therapy: principles and experimental research. *Photochem Photobiol*, 65(2):235–51, 1997.

[259] H. Ding, B. D. Sumer, C. W. Kessinger, Y. Dong, G. Huang, D. A. Boothman, and J. Gao. Nanoscopic micelle delivery improves the photophysical properties and efficacy of photodynamic therapy of protoporphyrin IX. *J Control Release*, 151(3):271–7, 2011.

[260] J. Kecht, A. Schlossbauer, and T. Bein. Selective functionalization of the outer and inner surfaces in mesoporous silica nanoparticles. *Chem Mater*, 20(23):7207–7214, 2008.

[261] S. K. Sahoo, T. Sawa, J. Fang, S. Tanaka, Y. Miyamoto, T. Akaike, and H. Maeda. PEGylated zinc protoporphyrin: a water-soluble heme oxygenase inhibitor with tumor-targeting capacity. *Bioconjug Chem*, 13(5):1031–8, 2002.

[262] U. Rothbauer, K. Zolghadr, S. Tillib, D. Nowak, L. Schermelleh, A. Gahl, N. Backmann, K. Conrath, S. Muyldermans, M. C. Cardoso, and H. Leonhardt. Targeting and tracing antigens in live cells with fluorescent nanobodies. *Nat Methods*, 3(11):887–9, 2006.

[263] A. Kirchhofer, J. Helma, K. Schmidthals, C. Frauer, S. Cui, A. Karcher, M. Pellis, S. Muyldermans, C. S. Casas-Delucchi, M. C. Cardoso, H. Leonhardt, K. P. Hopfner, and U. Rothbauer. Modulation of protein properties in living cells using nanobodies. *Nat Struct Mol Biol*, 17(1):133–8, 2010.

[264] U. Rothbauer, K. Zolghadr, S. Muyldermans, A. Schepers, M. C. Cardoso, and H. Leonhardt. A versatile nanotrap for biochemical and functional studies with fluorescent fusion proteins. *Mol Cell Proteomics*, 7(2):282–9, 2008.

[265] K. Berg, A. Dietze, O. Kaalhus, and A. Høgset. Site-specific drug delivery by photochemical internalization enhances the antitumor effect of bleomycin. *Clin Cancer Res*, 11(23):8476–85, 2005.

[266] P. J. Lou, P. S. Lai, M. J. Shieh, A. J. Macrobert, K. Berg, and S. G. Bown. Reversal of doxorubicin resistance in breast cancer cells by photochemical internalization. *Int J Cancer*, 119(11):2692–8, 2006.

[267] T. D. Pollard and J. A. Cooper. Actin, a central player in cell shape and movement. *Science*, 326(5957):1208–12, 2009.

[268] V. Sirri, S. Urcuqui-Inchima, P. Roussel, and D. Hernandez-Verdun. Nucleolus: the fascinating nuclear body. *Histochem Cell Biol*, 129(1):13–31, 2008.

Acknowledgments

For the success of a PhD, it takes a lot of people who I would like to acknowledge in the following.

First of all, I wish to thank Prof. Christoph Bräuchle for his continuous encouragement, support and loyalty. Much appreciation is extended to Prof. Jens Michaelis and Prof. Don Lamb for scientific discussions and the great atmosphere on the second floor of Haus E.

It was a privilege to collaborate with Prof. Thomas Bein and Prof. Joachim Rädler. Thank you for fruitful discussions and support. Many thanks go to the reviewers of my thesis and other collaborating group leaders: Prof. Christina Scheu, Prof. Ernst Wagner and Prof. Heinrich Leonhardt.

I was privileged to closely collaborate with Valentina, Hanna and Axel. Thanks for all the exciting ideas, the fun we had in and outside the lab and for not giving up on the experiments that rarely wanted to work at once. It has been great working with you!
I also want to acknowledge Delphine and Nadia, Kourosh and Ulrich for discussing data, scientific input and sample preparations. Thanks to Monika for taking loving care of the cells. In addition, I would like to acknowledge Alexandra, Christian and Basti from the Bein lab for sample preparation, discussions and the fabulous 3D schemes for our publications!

The first person I met in the Bräuchle lab was Karla de Bruin. Thanks for teaching me so many things and supporting me. Thanks for being a great colleague and friend.
It was a pleasure to share daily PhD life with Julia, Frauke and Doro. I have so many things to thank you for, they will simply not fit on this page! I enjoyed each and every single day working with you. Thank you, ladies!

Thanks to my students Julia and Sophia. A special thanks goes to my ex-student and now-colleague Vroni. I know that you will take good care of the project and foster the good collaborations.

I had the fortune to meet a lot of wonderful people in AK Bräuchle/Lamb/Michaelis. Thank you for the great time with you. In particular I thank: Adriano, Stephan, Adam, Iko, Martin, Ellen, Gregor, Timo, Jens, Meli, Flo, Wolfi, Niko, Bärbel, Julia, Viola, Sushi and Moritz.

Thanks to my mom, Ulrike, and my dad, Helmut, as well as to Mirjam, Carolin, Emma and Johannes. You are the best support one can possibly think of!

My final thanks goes to Marcel. Thanks for your never-ending optimism, patience, inquisitiveness and support. Thanks for being by my side!

List of publications

Publications related to the thesis

peer reviewed journals

- Sauer A.M.*, Schlossbauer A.*, Cauda V., Schmidt A., Engelke H., Rothbauer U., Zolghadr K., Leonhardt H., Bräuchle C., Bein T.
  Cascaded Photoinduced Drug Delivery to Cells from Multifunctional Core-Shell Mesoporous Silica.
  submitted

- Sauer A.M.*, Schossbauer A.*, Ruthardt N., Cauda V., Bein T., Bräuchle C.
  Role of endosomal escape from disulfide-based drug delivery from colloidal mesoporous silica evaluated by live-cell imaging.
  Nano Lett, 10(9):3684-91, September 2010.

- Sauer A.M.*, Cauda V.*, Engelke H.*, Arcizet D.*, Bräuchle C., Rädler J., Bein T.
  Colchicine-loaded lipid bilayer-coated 50 nm mesoporous nanoparticles efficiently induce microtubule depolymerization upon cell uptake.
  Nano Lett, 10(7):2484-92, July 2010.

* contributed equally.

posters

- Sauer A.M., de Bruin K.G., Plank C., Bräuchle C.
  Dynamics and localization of magnetic transfection complexes.,
  European Symposium on Controlled Drug Delivery 2008, Noordwijk aan Zee, Netherlands.

- Sauer A.M., de Bruin K.G., Plank C., Bräuchle C.
  Dynamics and localization of magnetic transfection complexes.,
  Summerschool “Nanoobjects in living cell” 2008, Lille, France.

- Sauer A.M., de Bruin K.G., Plank C., Bräuchle C.
  Internalization dynamics and localization of magnetic transfection complexes.,
  Annual Meeting of the European Society of Gene and Cell Therapy 2008, Bruges, Belgium.

- Sauer A.M., de Bruin K.G., Ruthardt N., Plank C., Wagner E., Bräuchle C.
  Live-cell imaging of nanoparticles for gene and drug delivery.,
  Winterschool of the Nanosystems Initiative Munich (NIM) 2009, St. Christoph, Austria.

- Sauer A.M., Ruthardt N., de Bruin K.G., König F.M., Bausinger R., Plank C., Wagner E., Bräuchle C.
  Live-cell imaging: nanoparticle internalization and gene delivery,
  3th Annual Symposium on Nanobiotechnology at the University of California Los Angeles 2009, CA, USA.

- Sauer A.M., Cauda V., Janik J., Weiß V., Argyo C., Ruthardt N., Bein T. and Bräuchle C.
  Characterization of custom-designed mesoporous silica nanoparticles for their application in live-cell imaging,
  22nd Deutsche Zeolith Tagung 2010, Munich.

- Sauer A.M., Schlossbauer A., Cauda V., Engelke H., Ruthardt N., Arcizet D., Rädler J.O., Bein T., Bräuchle C.
  Live-Cell Imaging of Colloidal Mesoporous Silica Nanoparticles for Drug Delivery: Drug Loading, Pore Sealing and Controlled Release,
  4th Annual Symposium on Nanobiotechnology 2010, Munich.

- Sauer A.M., Schlossbauer A., Cauda V., Engelke H., Argyo C., Arcizet D., Ruthardt N., Rädler J.O., Bein T., Bräuchle C.
  Live-Cell Imaging of Colloidal Mesoporous Silica Nanoparticles for Drug Delivery: Drug Loading, Pore Sealing and Controlled Release,
  Biophysical Society 55th Annual Meeting in Baltimore 2011, MD, USA.

Publications not related to the thesis

- Sauer A.M., de Bruin K.G., Ruthardt N., Mykhaylyk O., Plank C., Bräuchle C., J
  Dynamics of magnetic lipoplexes studied by single particle tracking in living cells.
  J Control Release, 137(2):1-36-45, July 2009.

- Capone R., Garcia Quiroz F., Prangkio P., Saluja I., Sauer A.M., Bautista M.R., Turner R.S., Yang J., and Mayer M.
  Amyloid-beta-Induced Ion Flux in Artificial Lipid Bilayers and Neuronal Cells: Resolving a Controversy.
  Neurotox Res, 16(1):1-13, July 2009.

Curriculum Vitae

Anna Magdalena Sauer

Date of birth	25th of June 1983
Place of birth	Assis / Brasil

Education

2008 - 2011	Graduate studies in the group of Prof. Christoph Bräuchle, LMU München
2005 - 2008	Master studies in Molecular Biotechnology, TU München
2002 - 2005	Bachelor studies if Molecular Biotechnology, TU München
1994 - 2002	Theodolinden-Gymnasium München (secondary school)

Awards and scholarships

2011	Römer prize of the faculty of chemistry for the doctoral thesis, LMU München
2009	Römer prize of the faculty of chemistry for the master thesis, LMU München
2008 - 2011	Member of the International Doctorate Program NanoBioTechnology (IDK-NBT)